Max Planck Institut für Kolloid- und Grenzflächenforschung
Abteilung Theorie

Titel der Dissertation

Model membranes grafted with long polymers

**Dissertation
zur Erlangung des akademischen Grades
"doctor rerum naturalium"
(Dr. rer. nat.)
in der Wissenschaftsdisziplin Experimentelle Physik**

**eingereicht an der
Mathematisch-Naturwissenschaftlichen Fakultät
der Universität Potsdam**

von

Vesselin Kirilov Nikolov

Potsdam, im März 2004

Аз съм българче, живея
В дни велики, в славно време.
Син съм на земя прекрасна
Син съм на юнашко племе

Иван Вазов, 1912

Благодарности

Тук бих искал да изкажа моята най-сърдечна благодарност към хората, без чиято помощ и безрезервна подкрепа тази дисертациа не би била възможна. На първо място ще поставя проф. Липовски и Макс Планк Институт, благодаря за финансовата подкрепа. Разбира се, не мога да не поставя на второ място ръководителят ми Руми Димова, благодаря ти за предоставената възможност, за доверието, за съдействието, за дискусиите, за личните услуги, за свободата да работя и да развивам собствените си идеи. На трето място (но може би първо по важност) искам да благодаря на приятелката си Маргарита. Маги, благодара ти за търпението, за разбирането, за отправените критики. Твоята подкрепа и доверие бяха през последните 3 години бяха една от основните сили, които ме тласкаха към целта. Подобни думи трябва да отправя и към семейството си, майка ми, баща ми и брат ми. Не мога да не спомена членовете (бивши и настоящи) от групата на Руми (т. нар. Rumiana Dimova AG) – Джеръми Пенсър, Крис Халуска, Карин Риске, Корнелия Синн (Кони), Ева Кодина, Антье Райнеке и Томас Франке. Те винаги бяха до мен в трудни моменти. Съвместната ни работа за мен беше чест и удовоствие. Работната атмосферата, която вие създадохте, беше неповторима и уникална. Срещите ни на масата за кикърс бяха не по малко стимулираши и ползотворни от научните ни дискусии. Специални благодарности за Крис за усилията му да усъвършенства моят "американски" английски. Задължително трябва да спомена Радостина Георгиева, която посвети много време и усилия за моите ескперименти с конфокалния микроскоп. Благодаря ти, без твоето съдействие тази част от дисертацията ми нямаше да е същата. Не мога да не изкажа благодарност на хората от групата на проф. Липовски, особено на Мартин Бринкман, Джулиан Шилкок и Ханс-Гюнтер Дьоберайнер. Контактите ми с вас откриха нови хоризонти и ми дадоха безценна насока за бъдещо развитие. Тук е мястото за спомена имената на три бивши членове на тази група - Тицияно Зито, Лоренцо Джиада и Велиа Миникоци - имената не само изглеждат италянски, наистина са такива. Благодаря ви за всичко. Сега идва ред на още едно италянско име - Анджело Валериани - координатор на IMPRS (International Max Planck Research School). Благодаря за всичко, което направи за мен през последните три години. Искам да изкажа специални благодарности на всички гореспоменати италиянци за прекрасното кафе и невероятната компания. Накрая бих искал да спомена имената на хора, които не се вписват в гореспоменатите категории, но контактите ми с тях бяха незабравимо преживяване: Ривелино Монтенегро, Инг Чао, Герхард Гомпер, Лиинг Уанг, Милена Михайлова, Пол Лазар, Богдан Сербаною, Лутер Райх и Феликс Мейзер. На последно място (но не и по важност) бих искал да благодаря на хората от групата "колоидна химия" в нашия институт за невероятните купони и биренатa подкрепа.

Acknowledgments

Here I would like to express my sincere acknowledgments to the people, whose full backing made this thesis possible. First of all I would like to thank to Prof Lipowsky and Max Planck Society for the financial support. Of course the second person in the list is my advisor Dr. Rumiana Dimova, thank you for giving me opportunity, for the confidence, for the assistance, for all discussions, for the personal favors, for the freedom to work on my own and to develop my own ideas. I would like to thank to my girlfriend Margarita. Magi, thank you for the patience, for the understanding and for the criticism. During the last 3 years your support and faith were one of the most important driving forces for me. Similar words I should address to the members of my family – my mother, father and brother. I feel obliged to mention the names of the other members (present and former) of Rumiana's research group (also known as Rumiana Dimova AG) - Jeremy Pencer, Chris Haluska, Karin Riske, Cornelia Sinn, Eva Codina, Antje Reinecke and Thomas Franke. They were always with me at the most difficult moments. You guys, created a unique atmosphere in the group. Our collaboration for me was my pleasure and honor. Special acknowledgments to Chris for his efforts to improve my "American" accent. I have to mention the name of Dr. Radostina Georgieva. She invested incredible amounts of time to perform experiments with the confocal microscope. Thank you, without your assistance this part of my thesis would not be the same. I cannot ignore the other members of Prof. Lipowsky's (besides Rumiana's group) group, especially Martin Brinkmann, Julian Shillcock and Hans-Günther Döbereiner. My contacts with you expanded my view and gave me a precious direction for further development. Here is the best moment to mention the names of the former members of this group – Tiziano Zito, Lorenzo Giada and Velia Minicozzi – the names not only sound like Italian ones, the are Italian. Thank you for everything. What follows is another Italian name -Angelo Valleriani - the coordinator of IMPRS (International Max Planck Research School on Biomimetic systems). Thank you for everything you did for me during the last three years. I would like to express special acknowledgments to all mentioned Italians for the wonderful coffee and the great company. At the end I would like to mention the names of some people which do not belong to any the already mentioned groups, but my contacts with them were unforgettable experience: Rivelino Montenegro, Ying Qiao, Gerhard Gompper, Liying Wang, Milena Mihayilova, Paul Lazar, Bogdan Serbanoiu, Luther Reich and Felix Meiser. At last but not least I would like to thank to all people from the department of colloid chemistry for the great parties and beer support.

Resume

Model membranes grafted with long polymers

1. The subject of this study is a systematic investigation of the changes in the elastic properties of lipid membranes, induced by anchored long polymers. The polymers are anchored asymmetrically, only on the membrane outer surface, thus inducing spontaneous curvature. Theoretical calculations[1] predict two limiting regimes for the membrane spontaneous curvature as a function of the surface polymer concentration: *i)* at low coverage (mushroom regime) the spontaneous curvature scales linearly with the surface density of anchored polymers; *ii)* at high surface concentration (brush regime) the dependence is quadratic
2. We attempt to test experimentally the theoretical predictions for the mushroom regime by monitoring the morphological changes induced on model membranes.
3. As model membranes we use swollen Giant Unilamellar Vesicles (GUVs) made of DOPC (18:1)(1, 2-Dioleoyl-*sn*-Glycero-3-Phosphocholine) and biotinyl-CAP-PE (18:1) (1, 2-Dioleoyl-*sn*-Glycero-3-Phosphoethanolamine-N-Cap Biotinyl). The second of these lipids has a biotin "hook" attached to the hydrophilic head-group. The purpose of this biotin-end design of the molecule is to make use of the strong non-covalent biotin-avidin binding as a further connection.
4. The ratio of bound to the vesicle membrane vs. free bulk avidin is proportional to the equilibrium constant of the avidin-biotin reaction (avidin can be bound to only to biotinyl-CAP-PE). It is assessed with Isothermal Titrational Calorimetry (ITC) measurements.
5. The performed measurements can be classified in three groups depending on the concentration of biotin relative to the concentration of avidin in the calorimeter the working cell: *(i) Excess of avidin*; *(ii) Molar ratios close to 1:1 avidin to biotin; (iii) Large excess of biotin*.
6. We found that the equilibrium constant of the avidin-biotin reaction in the case with biotin, which is attached to the membrane lipids is lower than the reported in the literature[2] value corresponding, obtained for the binding reaction between free avidin and free biotin. Presumably such difference originates from *(i) Geometrical constraints*. When attached to the membrane lipids the biotin group is about 1.5 nm above the membrane and therefore is less accessible than in bulk; additional complication arises from membrane fluctuations – they may hinder avidin-biotin binding. Thus, presumably the biotinylated membranes bind much fewer avidins than the same amount of free bulk biotin would bind; *(ii) Loss of entropy*. When inserted in the two dimensional membrane, the biotin looses degrees of freedom and therefore entropy. Such loss is expected to result in a decrease in the Gibbs free energy and correspondingly in smaller equilibrium constant.
7. As long polymers we use λ-phage DNA molecules with a biotinylated 3' ("sticky") end. The purpose of this biotin modification is to enable the molecule to make use of the strong non-covalent bond with avidin, which resides on the vesicle surface.
8. We set the number of DNA anchoring sites (avidin-biotin complexes) by varying the membrane lipid composition (the molar ratio DOPC/Biotinyl-CAP-PE). The surface concentrations of anchors, used in this study were calculated in terms of overlapping concentration Γ^{ov} (this surface concentration separates mushroom and brush regime) and they were $0.03\Gamma^{ov}$, $0.06\Gamma^{ov}$, $0.12\Gamma^{ov}$, $0.3\Gamma^{ov}$ and $0.6\Gamma^{ov}$.

9. The changes in the membrane spontaneous curvature and the bending modulus, induced by the anchored DNA, are measured simultaneously by combination of optical microscopy and analysis of the membrane fluctuations.
10. Depending on the surface concentration of anchors, two different effects were observed: *(i)* at low surface concentration an increase in the membrane spontaneous curvature with the increase of the surface concentration was measured by performing analyses of the membrane fluctuations; *(ii)* At high surface concentration the anchored polymers induced vesicle budding and the analyses of membrane fluctuations were not possible. The change in the spontaneous curvature was estimated from the size of the buds.
11. We attempted to estimate the amount of anchored fluorescently labeled DNA by using three different fluorescence measurement techniques – fluorometry, fluorescence microscopy and confocal microscopy. The confocal microscopy experiments demonstrated that the DNA molecules were anchored to membranes with different surface concentration of avidin anchors, but no quantitative information about their number was obtained.
12. The combined data from the fluctuation spectroscopy and bud analysis show that up to $0.3\Gamma^{\varphi v}$, the DNA induced curvature increases with the increase of the surface concentration of anchors.
13. The induced spontaneous curvatures in the experiments with $0.3\Gamma^{\varphi v}$ and $0.6\Gamma^{\varphi v}$ are identical. Presumably this effect is due to the relatively low bulk concentration of DNA used in this study. Regardless of the higher surface concentration of anchors, the number of anchored DNA molecules does not change.
14. The spontaneous curvatures obtained from both methods (fluctuation spectroscopy and bud analysis) cannot be directly compared. The bud analysis yields the absolute spontaneous curvature, while the fluctuation spectroscopy gives a quantity, proportional to the absolute one.
15. The absolute value of the spontaneous curvature and the membrane bending stiffness are to be obtained. The latter can be achieved when the experimentally measured fluctuation spectra are matched with Monte Carlo generated spectra[3].
16. The experimental data are to be compared with the theoretical predictions when the fluctuation spectroscopy data are quantified with Monte Carlo simulations. The unknown surface concentration of anchored DNA (see 11) is to be used as a fitting parameter.

Contents

Introduction

Materials and experimental techniques

Binding of avidin to biotinylated membranes (ITC study)

Chapter 1

Introduction

1.1. Membranes

1.1.1. Membrane composition. Lipids

Biological membranes are composed of proteins embedded in a lipid bilayer matrix (fig. 1.1). The bilayer is a two-dimensional fluid, supported by the cytoskeleton underneath. The lipid composition is complex and generally depends on cell function, e.g. animal and plant cell membranes have different lipid composition. Membrane proteins carry out the dynamic processes associated with the membranes and therefore specific proteins are present only in particular membranes. They can be classified according to the way in which they are associated with membranes as: *(i)* integral (transmembrane) proteins which are tightly bound to the membranes by hydrophobic forces; *(ii)* peripheral (extrinsic) proteins which do not enter the lipid bilayer and are attached to the outside of the membrane. Membrane lipids are a class of amphiphilic molecules with huge diversity. Apart from forming the bilayer matrix, they play multiple roles within the membrane, such as regulatory functions, signal transduction, optimization of enzyme activity etc. We will concentrate on a particular class of lipids - glycerophospholipids – the most commonly occurring lipids in the animal and bacterial cell membranes. They have a glycerol backbone, which is non polar and water insoluble. One of the glycerol carbons is linked to a polar phosphate group and the other two are linked to hydrophobic fatty acid chains. The alkyl chains typically have an even number of carbons ranging from 14 to 24; the most commonly found chains in the cell membranes contain 16, 18 and 20 carbons [101]. The degree of unsaturation varies widely, but the most common unsaturated chains are 18:1, 18:2, 18:3 and 20:4 (where the first number indicates the chainlength and second – the number of double bonds) [101]. Glyceride nomenclature is usually presented in terms of stereoscopic numbers (*sn*). In most phospholipids the phosphate group is at *sn*-3 position and is usually linked to one or several groups (choline, ethanolamine,

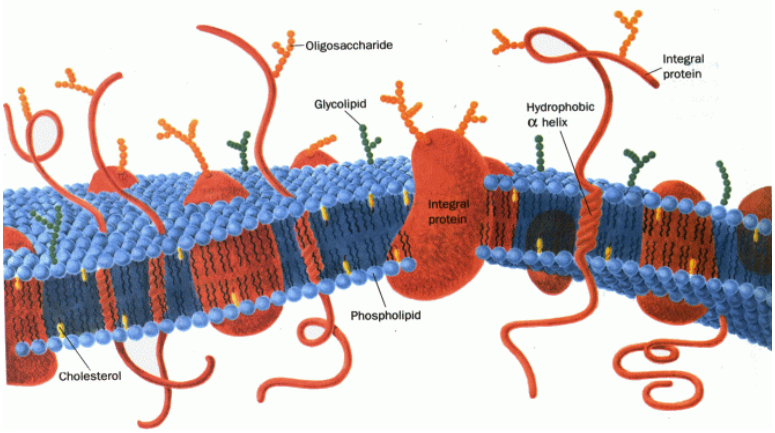

Fig 1.1: schematic diagram of a cell membrane. Integral proteins are embedded in a bilayer composed of lipids and cholesterol. The carbohydrate components of glycoproteins and glycolipids occur only on the outer surface of the membrane. The cytoskeleton is not shown (Taken from [1])

hydroxyl etc) as shown in fig 1.2. Many naturally occurring phospholipids have a saturated and an unsaturated chain. In the unsaturated ones, the double bond can exist in two configurations. In *cis bonds*, the two pieces of the fatty acid chain on either side of the double bond are either both "up" or both "down," such that both are on the same side of the bond. In *trans bonds*, the two pieces of the molecule are on opposite sides of the double bond, that is, one "up" and one "down" across from each other. This places a "kink" in the molecule which is generally disruptive for the lipid packing in the bilayer. Most of the naturally occurring double bonds are *cis* rather than *trans* [6].

Apart from phospholipids there are other major classes of membrane components like glycolipids, sphingolipids and cholesterol. Glycolipids are membrane lipids with heads covalently bound to monosaccharides or polysaccharides (fig 1.1). They play an important role in signal transduction and targeting [2]. Sphingolipids are composed of a backbone of sphingosine which is derived itself from glycerol. They predominate in the myelin sheath of nerve fibers [2]. Cholesterol, a kind of steroid, is an amphipathic molecule that serves as a temperature-stability buffer. At higher temperatures cholesterol impedes phospholipid fluidity. At lower temperatures it interferes with solidification of membranes (e.g. in the latter case cholesterol affects the lipid-bilayer fluidity similar was as the unsaturated fatty acids do)

1.2. Model membranes

So far only the membranes of living cells were considered. Cell diversity and complexity, however, hinder the collection of detailed quantitative information about the physical and chemical properties of their membranes. Simple model systems, which can replace the

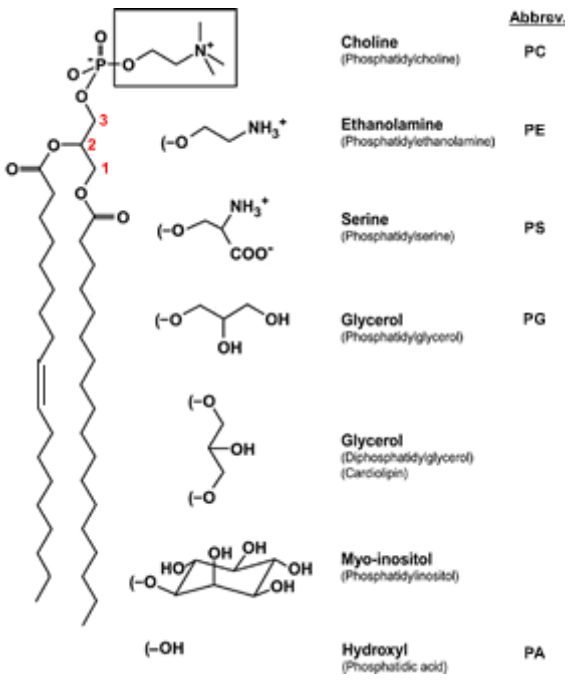

Fig 1.2: Chemical structure of some biologically important phospholipids. The naturally occurring phospholipids have saturated, unsaturated (or both) fatty acid chains. The charged headgroup is highly polar, while the rest of the molecule is apolar. Both, PC and PE, are zwitterionic molecules, whereas the other phospholipids carry one negative charge at physiological conditions. Stereoscopic numbers are shown in red.

biological membranes in the lab, are provided by lipid membranes with a small number of components (fig 1.3). They are usually made of one type of lipid [3, 13, 16, 32], but can contain a mixture of two [3, 33] or two lipids and cholesterol [34]. Of course, this is an oversimplification of the cell membrane and the properties of artificial membranes cannot be directly related to that of living cells. Nevertheless the results obtained from those model systems, combined with theoretical modeling and calculations, provide useful information about all membranes. One model system which is frequently used is vesicles (or liposomes). They are closed membrane bags encompassing a certain volume of aqueous solution. As far as the vesicle size and the number of lamellae composing the membrane is constant one can distinguish different classes of vesicles: *(i)* small (S), large (L) and giant (G), typical sizes 20-50 nm (S), 50-500 nm (L) up to 0.5-100 μm (G) and *(ii)* uni-, oligo- or multilamellar (U, O, M respectively). If the term "vesicle" is abbreviated as V, one may assemble several widely used abbreviations such as SUV, LUV, GUV and MLV. In this study we will focus on two classes of vesicles – GUVs and LUVs. GUVs have the size of cells, can be visualized with an optical microscope and allow working with individual vesicles. In contrast, LUVs provide information in an indirect way. GUVs are a subject of theoretical interest and there are a lot of calculations and computer simulations aimed at understanding their behavior, material properties and shape transformation [3, 12, 13]. Systematic experimental studies of vesicles originate from the mid 1960's. Two recent reviews [3, 5] summarize the current knowledge about the physico-chemical and mechanical properties of GUVs, including some applications.

Vesicles are self-assembled objects which form spontaneously when lipid is in contact with water. Lipid geometry favors assembly of bilayers rather than micelles. When formed,

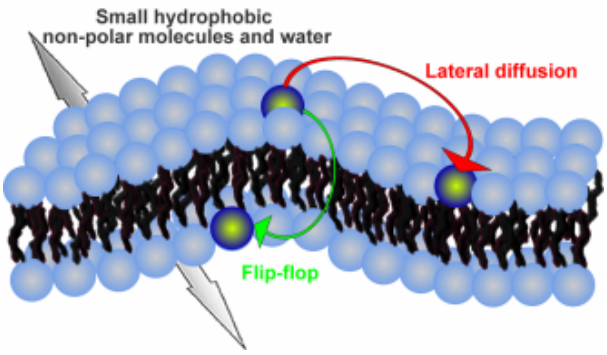

Fig 1.3: A model membrane made of a single lipid. Lipids can diffuse freely in the two-dimensional bilayer matrix. "Flip-flop" phenomena are relatively rare, because they are not energetically favorable. The lipid which undergoes lateral diffusion/"flip-flop" is shown in green.

bilayers self-organize in a closed structure to prevent the contact between the lipid hydrophobic tails and the solvent. Depending on the temperature, a bilayer can be in either a fluid (high temperature) or a gel (low temperature) state. Both states are separated by a well defined phase boundary called main phase transition. In the fluid phase the membrane is isotropic and individual lipids can diffuse rapidly along the two-dimensional membrane surface (fig.1.3), as described by the fluid mosaic model [6]. Due to relatively free rotation around the C-C bond, the saturated fatty acids are highly flexible and there is a considerable disorder in the alkyl chains, as indicated by X-ray diffraction data [6]. There is a possibility for an exchange of lipids between both monolayers of the membrane. This phenomenon is known as "flip-flop". In general the flip-flop rate depends on the membrane composition, it is relatively rare for one component membranes (but frequent for cholesterol), because the hydrophilic head of the lipid has to cross the highly hydrophobic interior of the membrane (fig 1.3), which presents a high energy barrier. Lipid bilayers are impermeable to most polar substances. The living cells control the ion flux in/out the cell by special protein pumps. Lipid membranes are rather permeable to water molecules, although these are polar – maybe due to their small dimensions.

1.3. Mechanical properties of model membranes

Lipid vesicles are easily deformable. The elastic properties of their bilayer not only determine the response to external mechanical stress but also are important indicators of the internal state of the membrane. In the classical theory of elastic sheets [25] one can distinguish three independent modes of elastic deformations: bending, stretching, in-plane shear, as shown in fig. 1.4. Together they characterize the deformation and rate of deformation of the lipid bilayer. These independent shape changes are produced by the application of external forces to a membrane element, as shown in the fig. 1.4. A principal stress per unit length $\boldsymbol{\tau}$ along the membrane contour leads to membrane dilatation; deviatoric

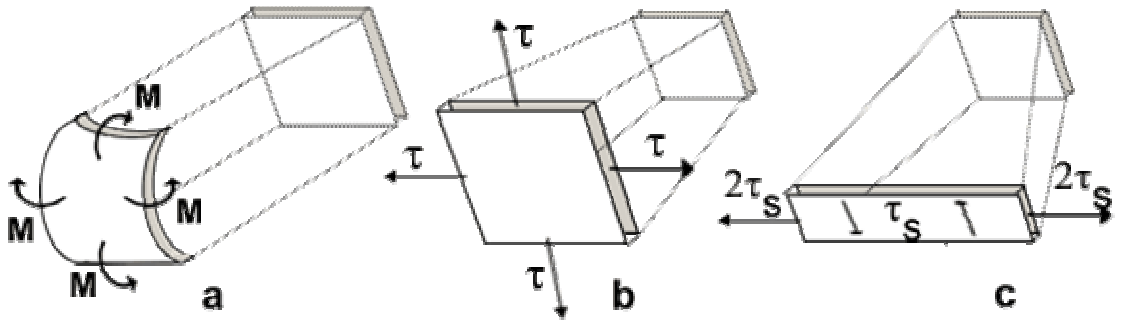

Fig. 1.4: Modes of deformation of a square element of membrane surface: (a) bending, (b) isotropic area dilatation, (c) in-plane extension or surfaces shear at constant area. (for more details see reference [3, 25])

stress τ_s produces shear; and the moment resultant M_{bend} per unit length results in bending or torque.

Area dilatation is characterized by the area expansion/compressibility modulus K, given by the equation

$$\tau = K\alpha = K\frac{(A - A_0)}{A_0} \tag{1.1}$$

where α is the fractional change in the membrane area $\Delta A/A_0$ (ΔA-expanded/shrunk area, A_0-initial membrane area) produced by isotropic membrane stress τ. Typically the membrane expansion is small, not greater than 1-5 % [3]. Experimentally K can be determined by using micropipette technique [3], photon correlation spectroscopy [16], Dynamic Light Scattering (DLS) of LUVs subjected to osmotic stress [32], NMR and X-ray diffraction of strongly dehydrated multibilayer arrays [2]. A typical value for lipids is K=100-200 dyn/cm [3, 16]. For cholesterol containing membranes, e.g. SOPC : cholesterol=1:1, K≈850 dyn/cm [3].

Membrane bending is characterized by the bending rigidity κ, which is the ratio of the membrane bending momentum M_{bend} to changes in the total membrane curvature ΔM:

$$\kappa = \frac{M_{bend}}{\Delta M} \tag{1.2}$$

The energy needed to bend a membrane is in order of Kl_{me}^2 [104], where l_{me} is the bilayer thickness. The corresponding energy for membrane stretching is KA_0. Usually $A_0 \gg l_{me}^2$ and the energy cost for bending will be much lower than the corresponding energy cost for stretching such a membrane. The bending rigidity modulus can be measured by using flickering spectroscopy of giant quasispherical vesicles [37, 38], micropipette technique [3] and fluctuation spectroscopy of prolate vesicles [11, 13]. A typical value is $\kappa \approx 20\ k_BT$.

Surface shear rigidity for a membrane element μ is the ratio between surface shear stress τ_s and shear deformation e_s,

$$\tau_s = 2\mu e_s \tag{1.3}$$

Because the lipid bilayers are laterally isotropic there is no shear rigidity. This mode of deformation however has to be considered when dealing with erythrocytes or membranes made of polymerized lipids.

Viscous Coefficients characterize the viscosity of each of these three modes. They are given by proportionalities between forces and rates of deformation, e.g. the bending surface viscosity of a fluid bilayer is $\eta_b \sim \kappa t_e$, where t_e is the time scale, associated with the alkyl chain conformations (10^{-10}-10^{-5} s, [3]). It is very difficult to conduct experiments at such short time scales, because one needs a very fast CDD camera, which is able to grab frames in the microseconds range. Such measurements however are possible. The viscosities for different phospholipid bilayers in fluid states are estimated to be on the order of 10^{-7}-10^{-6} surface poise (sp) [39]

1.4. Modeling vesicle shapes

The vesicle can attain many different shapes, depending on the experimental conditions like bilayer composition, temperature [13], pH [35], method of vesicle formation, presence of colloidal particles [36] etc. There are many experimentally observed shapes [3, 13], but it is difficult to decide whether the observed shape is an equilibrium one, because a vesicle can occupy a metastable state for time, (much) longer than the duration of an experiment [79, 100]. On the other hand, theoretical studies consider equilibrium shapes and predict shape transformations of vesicles. Matching experimental data and theoretical calculations is a very natural approach to characterize the equilibrium (stationary) vesicle shapes. The present understanding of the diversity of vesicle shapes and shape transformations is based on three models: spontaneous curvature model (SC), area difference model (ΔA) and area difference elasticity model (ADE). The ADE model is a generalization of the two others and we will consider its main features. Later we will point out the cases where ADE approaches SC or ΔA models.

In order to facilitate modeling, one can ignore the bilayer structure and consider the membrane as a mathematical surface characterized by its local geometric properties, known from the differential geometry. It follows that the shape of any surface can be characterized by its mean curvature *M* and Gaussian curvature *G*, defined as [8]

$$M = \frac{1}{2}(C_1 + C_2) \qquad \text{and} \qquad G = C_1 C_2 \tag{1.4}$$

Here C_1 and C_2 are the two principal curvatures of the curvature tensor $\mathcal{M}$. Each leaflet, inner and outer, has its own relaxed (preferred) area denoted as A_0^{in} and A_0^{out} respectively. The actual

area, A^{in} and A^{out}, however, can be bigger or smaller than the relaxed one, which implies energy cost. Let us define relaxed and actual area difference as $\Delta A_0 = A_0^{out} - A_o^{in}$ and $\Delta A = A^{out} - A^{in}$ respectively. Area difference could be induced by leaflet expansion or shrinkage under lateral stress. For GUVs the curvature radii are large compared to the membrane thickness l_{me} and the curvature energy can be expanded in powers of $l_{me}C_i$. As originally proposed by Helfrich [9], up to the second order in curvatures, the elastic energy of such membrane can be presented as

$$\mathcal{H}_{ADE} = \int_A dA 2\kappa\left(M - M_{sp}\right)^2 + \frac{\bar{\kappa}}{2}\frac{\pi}{A l_{me}^2}\left(\Delta A - \Delta A_0\right)^2 \qquad (1.5)$$

Here κ and $\bar{\kappa}$ are the membrane bending modulus and nonlocal bending rigidity. The integral in the first term is calculated over the entire vesicle surface A. It is dimensionless and the energy scale is set by the bending modulus κ. The spontaneous curvature M_{sp} reflects a possible asymmetry between both leaves of the bilayer. The physical origin of spontaneous curvature could be either different chemical environment on both sides of the membrane or a different chemical composition of the monolayers. In the case of a symmetric bilayer, one has $M_{sp}=0$. The second term of (1.5) affects the nonlocal bending rigidity, because the area difference is related to the integrated (non-local) curvature of the membrane as

$$\Delta A = 2 l_{me} \int_A dA\, M \qquad (1.6)$$

The non-local bending rigidity $\bar{\kappa}$ has units of energy and the calculations performed in [12] demonstrate that it is generically of the order of Kl_{me}^2 (see [104]), as the bending modulus κ, where K is the area stretching modulus of the bilayer. The equilibrium shape is found by minimizing (1.5) under the constraints of fixed relaxed (initial) monolayer area difference ΔA_0, constant enclosed volume V and total vesicle surface area A

Let us consider the characteristics of the ADE model. It has four different length scales: R_A, R_V, M_{sp}^{-1} *and* $\Delta A_0/l_{me}$. The first of them is the area equivalent radius, defined as $R_A \equiv \left(A/4\pi\right)^{1/2}$. The second, the volume equivalent radius, is defined as $R_v \equiv (3V/4\pi)^{1/3}$. If all distances are scaled with R_A, there will be only three independent parameters left: *(i)* the reduced volume

$$v = \frac{V}{\left(4\pi/3\right)R_A^3} = \left(\frac{R_V}{R_A}\right)^3 \quad , \qquad (1.7)$$

(ii) the reduced spontaneous curvature

$$m_{sp} = M_{sp} R_A \quad , \qquad (1.8)$$

and *(iii)* the reduced relaxed area difference

$$\Delta a_0 = \frac{\Delta A_0}{8\pi l_{me} R_A} \quad , \tag{1.9}$$

There are two energy parameters in the model, the bending rigidity κ and the non-local bending stiffness $\bar{\kappa}$. If one ignores the thermally excited shape fluctuations of the membrane, it is only the ratio,

$$\alpha = \frac{\bar{\kappa}}{\kappa} \tag{1.10}$$

which is relevant to the shape problem. By using the rescaled parameters, the ADE bending energy can be rewritten as [11]

$$\frac{\mathcal{H}_{ADE}}{(4\pi)^2 \kappa} = \frac{1}{4\pi}\int_A dam^2 + \frac{\alpha}{2}\left(\Delta a - \left(\Delta a_0 + \frac{1}{2\pi\alpha} m_{SP}\right)\right)^2 + const \tag{1.11}$$

where $\Delta a = \Delta A / 8\pi l_{me} R_A$, $m = MR_A$ and $da = d\mathcal{A} / 4\pi R_A^2$. In this expression the sum of the scaled spontaneous curvature and the relaxed area difference Δa_0 represent the effective area difference

$$\Delta \bar{a}_0 = \Delta a_0 + \frac{1}{2\pi\alpha} m_{SP} \tag{1.12}$$

The three relevant parameters of the dimensionless ADE Hamiltonian (1.11) are the reduced volume *v*, the ratio α and the effective area difference $\Delta \bar{a}_0$. The reduced volume is a measure for the enclosed volume of the vesicle and the membrane area available for shape changes. Spherical vesicles (*v*=1), for example, have no free area available for such changes. The parameter α interpolates the ADE model between the SC model (when $\bar{\kappa}$=0) and the ΔA model (when $\bar{\kappa} \to \infty$). For phospholipid bilayers α of the order of unity [12].The parameter $\Delta \bar{a}_0$ reflects the different sources of membrane curvature. The equilibrium shapes, predicted by the ADE model are described in [11] and [13] (see fig 1.5). Possible trajectories in the phase diagram presented in fig. 4.5 are discussed in Chapter 4.

1.2. Polymers

1.2.1. Physics of polymers

Because the goal of this thesis is to understand the behavior of long polymers, anchored to membranes, here we will briefly summarize the physical properties of polymers. They are macromolecules built of large number of small repeating units, called monomers, linked with

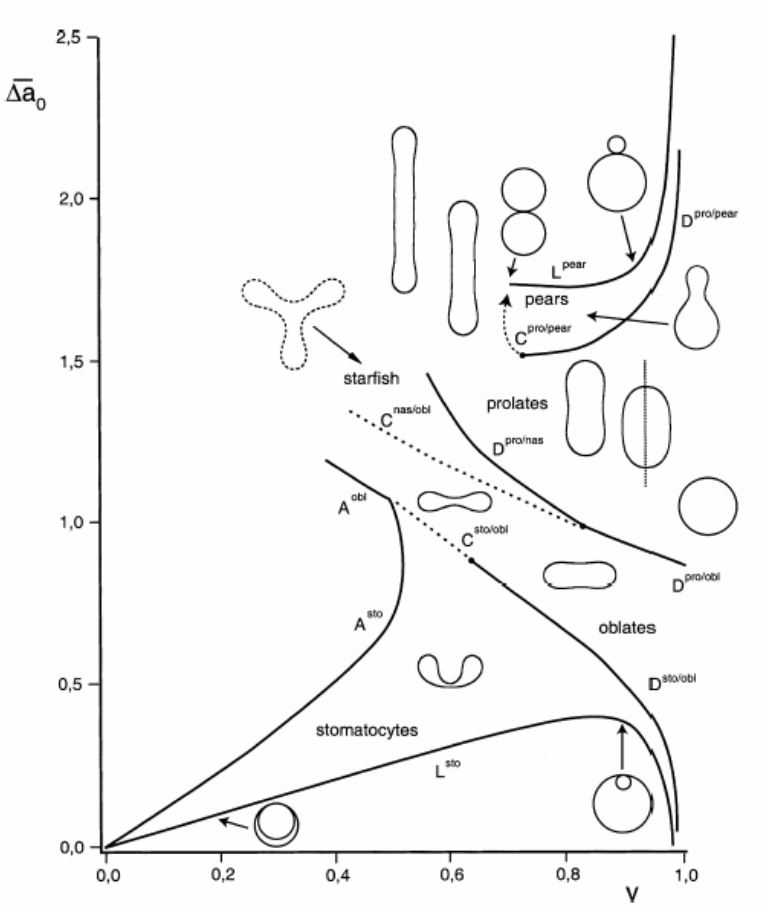

Fig 1.5: Vesicle shape phase diagram. For each region the shapes with lowest energy are indicated with their center of mass, located in the corresponding position in the phase diagram. On the horizontal axis is presented the vesicle reduced volume v; sphere corresponds to $v = 1$. On the vertical axis is shown the effective differential area $\Delta\overline{a}_0$, i.e. the preferred curvature of a vesicle [13]. Vesicle trajectories in this phase diagram are to be discussed in Chapter 4.

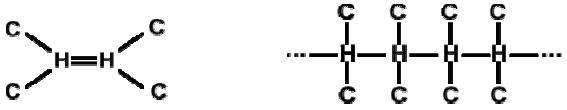

Fig 1.6: Ethylene and polyethylene

covalent bonds. According to the composition, origin and chain architecture polymers can be roughly classified as:

- *Homopolymers*, composed of identical units and *copolymers*, composed of different monomers
- *Biopolymers*, e.g. DNA, RNA and *synthetic polymers*.
- *Linear*, e.g. RNA, *branched*, e.g. polysaccharides, *star-like*, *comb-like*, *cross-linked.*

An example for a synthetic linear homopolymers is polyethylene, made by polymerization of ethylene (fig. 1.6).

The first step in the theoretical modeling of polymer chains is to replaces the real chain with an idealized one. The simplest theoretical model for an ideal chain is the *freely jointed chain* (FJC), which models a homopolymer chain without any monomer-monomer or monomer-solvent interactions. The chain can be presented by $N+1$ position vectors $\{\mathbf{R}_i\}$ of the backbone atoms or equivalently by N bond vectors $\{\mathbf{r}_i\}$, defined as

$$\mathbf{r}_i = \mathbf{R}_i - \mathbf{R}_{i-1} \tag{1.13}$$

Each bond vector is arbitrary orientated - there are no restrictions to the angles υ_i (between $\mathbf{r}_i$ and $\mathbf{r}_{i-1}$) and φ_i (between $\mathbf{r}_{i+1}$ and the plane defined by the two preceding vectors $\mathbf{r}_{i-1}$ and $\mathbf{r}_{i-2}$). The global properties of such chain may be deduced by statistical methods. Quantities of interest are the distribution functions of vectors $\mathbf{r}_i$. One pair of points of the chain is of special interest – the two end points of the polymer. The vector connecting these two points is called *end to end distance* vector $\mathbf{R}_E$ and is defined as

$$\mathbf{R}_E = \sum_{i=1}^{N} \mathbf{r}_i \tag{1.14}$$

This vector is a sum of independent random variables and its distribution function $p(\boldsymbol{R_E})$ can be calculated by applying the central limit theorem (CLT). CLT states that $p(\boldsymbol{R_E})$ obeys Gaussian distribution and can be presented as [15]

$$p(\mathbf{R}_E) = \left(\frac{3}{2\pi \left\langle R_E^2 \right\rangle} \right)^{3/2} \exp\left(-\frac{3R_E^2}{2\left\langle R_E^2 \right\rangle} \right) \tag{1.15}$$

This distribution function is identical with the one for the displacement of a Brownian particle after N uncorrelated steps. As it is apparent from (1.15) $\langle R_E \rangle$=0. This is a direct consequence from the random thermal fluctuations of both terminal ends of the chain. The smallest non-vanishing moment of $\mathbf{R}_E$ is its mean square average $\left\langle R_E^2 \right\rangle$. If a_p is the size of the bond vector $\mathbf{r}_i$, a measure for the polymer size called end-to-end distance, can be defined as

$$R_p = \sqrt{\left\langle R_E^2 \right\rangle} = a_p \sqrt{N} \tag{1.16}$$

FJC models the behavior and the properties of an idealized chain. There are two important characteristics to judge how well the model describes the chains of real polymers: the persistence length (describing the local rigidity of a chain) and the Kuhn's segment (describing the smallest chain segments which still can be considered to be statistically independent on each other).

If the first bond vector $\mathbf{r}_1$ is kept fixed, the persistence length l_p for an infinitely long chain is defined as

$$l_p = \sum_{i=1}^{\infty} \left\langle \frac{\mathbf{r}_1 . \mathbf{r}_i}{r_1} \right\rangle \tag{1.17}$$

The stiffer the chain under study, the further apart we will find the average position of its end point from the (virtually fixed) first bond and the largest we will find for l_p. The persistence length is therefore a suitable quantity which is often used to express the polymer stiffness.

The Kuhn length is introduced in a similar manner. The two experimental quantities which should be considered in the model chain are the mean square end to end distance R_p^2 and the largest extension $R_{E,\max}$ that is theoretically possible for the given polymer structure. These conditions define the appropriate number N_k and length a_k of freely jointed segments. As already was mentioned the ascribed FJC should fulfill the conditions

$$R_{E,\max} = a_k N_k \qquad \text{and} \qquad R_p = a_k \sqrt{N_k} \tag{1.18}$$

The Kuhn length a_k for a given polymer can be defined as the smallest chain segments which still can be considered to be statistically independent of each other. Therefore on length scale smaller than a_k it is possible to replace the segments of the model chain by any convenient kind of segment as the global chain properties are conserved.

Another model of an ideal chain is the Gaussian chain. It is constructed by assuming that the lengths a_i of the chain segment are variables and obey the Gaussian distribution where the standard deviation of the distance between the end points is identical to the effective bond length a. Apart from this, the orientations of bond vectors are considered to be absolutely free as in the FJC model. From here the distribution and partition functions of the chain configuration can be found [14]. All thermodynamic quantities of the chain can be computed from the partition function.

Ideal polymers chains models assume that all long range interactions between the segments of the polymer chain can be neglected, because the segments are well separated along the chain. Most polymers are highly flexible and it may happen that two segments come close to each other (and therefore interact), even though they are well separated from each other along the chain contour. One interaction which is always present in this case is the mutual avoidance of polymer segments: two segments of the chain cannot occupy the same spatial coordinates, because they cannot penetrate in each other. So, the effective interaction between two monomers is always repulsive and as a consequence the chain expands. Even in the case of attractive forces between the segments, the chain will swell while the repulsive steric interactions dominate. This phenomenon is called the *excluded volume* effect. In certain polymer solutions the excluded volume interactions of the polymer chains and the interactions between the chain segments and solvent molecules are exactly balanced and the excluded volume effect disappears. That happens in a special type of solvent, called *θ-solvent*.

The distribution of the end-to-end vector differs qualitatively form (1.15) [15]. The asymptotic behavior at large $\boldsymbol{R_E}$ is different, but still exponential, as in the ideal chain model.

At small $\boldsymbol{R_E}$, however, the deviation from ideal chain is drastic. The definition of the volume, occupied by the extended polymer chain is identical with the ideal chain definition:

$$R_F = \left\langle R_E^2 \right\rangle^{1/2} \tag{1.19}$$

The parameter R_F is called "Flory radius" and its relation with the number of monomers N in the chain is given by the scaling law

$$R_F = a_F N^{\nu} \tag{1.20}$$

The value of the exponent $\nu \cong 3/5$ expresses the difference to the ideal chain where $\nu = 1/2$. The second parameter a_F denotes the effective length per monomer.

1.2.2 Anchored polymers

1.2.2.1. Overview

The membranes of the living cells are always connected to at least two different polymers – the cytoskeleton and the glycocalix. These polymers determine the membrane structure and surface properties. One can mimic membrane properties by fixation of amphiphilic structures to artificial (laboratory made) planar lipid bilayers or vesicles. That can be achieved by several different architectures [17]: *(i)* Polymers connected to a lipid anchor which is inserted in the lipid bilayer core; *(ii)* Polymers with hydrophobic side groups, penetrating into the bilayer; *(iii)* Membrane spanning polymers; *(iv)* Combination of lipid anchoring and attractive interactions between the membrane and the polymer. In the present work, we will focus on polymers anchored to model membranes (fig. 1.7).

The effect of polymers, anchored to (or adsorbed on) lipid vesicles, has been intensively investigated experimentally since the beginning of 1990's [18-20]. A lot of qualitative data has been collected, but systematic studies have not been performed so far. The same problem has been explored theoretically for polymers which are attached symmetrically [21-27] (on both sides) or asymmetrically [21, 28, 29] (on one side only) to membranes. All calculations were based on the following simplifications and assumptions: *(i)* the real membrane is replaced with a mathematical surface with thickness l_{me}; *(ii)* the anchor size is neglected; *(iii)* the polymer is a Gaussian chain (i.e. the excluded volume effects are ignored) with average bond length equal to the Kuhn length a_K (or persistence length instead). Experimentally this situation corresponds to a polymer in θ-solvent; *(iv)* the anchored polymers can freely diffuse along the membrane surface, they do not interact with each other,

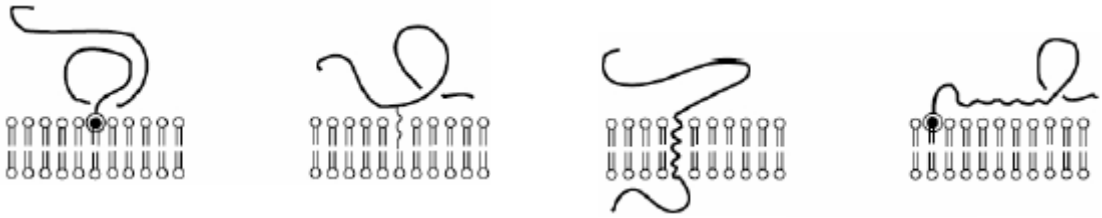

Fig 1.7: Different ways to attach polymer chain to bilayer membranes: (a) lipid anchor, (b) hydrophobic side chain, (c) membrane-spanning polymer segment, (d) anchored and adsorbed chain (taken from reference [17])

except sterically – they cannot penetrate each other[1]. Chronologically the first theoretical works dealt with polymers anchored to membranes with static (fixed) shapes. Later the membrane shape profile was determined analytically.

Let us consider a membrane with area A covered with N polymers. The polymer surface concentration Γ is defined as the number of anchored polymers per unit area. When Γ is low the average distance between polymers, ξ_{an}, is much large than their size R_p. In this very dilute regime they form well separated mushroom-like structures on the membrane surface and therefore is called mushroom regime. It extends up to a certain surface concentration Γ^{ov}, referred as overlap surface coverage. The latter is defined as the concentration at which the surface is completely covered by anchored polymers. For $\Gamma>\Gamma^{ov}$ one enters in a regime, where each polymer chain experiences an additional loss of entropy arising from the confinement by the neighboring chains. This, so called semi-dilute brush regime, has been studied in the context of polymers at rigid surfaces. It extends up to another limiting surface concentration Γ_{max} at which the overall loss of entropy of the chain becomes comparable with the anchoring energy, and the polymers are frequently exchanged between the membrane and the bulk solution.

1.2.2.2. Mushroom regime

Let us consider a smoothly curved membrane segment [10, 30] with mean curvature M and Gaussian curvature G, as defined in (1.7). Compared with a polymer anchored to a flat surface *(M=G=0)*, the curved surface will induce changes in the polymer configurational entropy. It cannot penetrate inside the membrane and therefore has only a half space available

[1] In reference [22] a blob picture has been used and there is some penetration (the innermost blob penetrates inside a spherical or cylindrical surface). Such penetration however is on the local scale, but it is small compared to the relevant scales (e.g. the radius of the surface or the height of the brush).

for shape configurations. In the limit of small deviations from flat surface the excess entropy will be $\Delta S_p(M,G) = S_p(M,G) - S_p(0,0)$ [10] and can be presented as

$$\Delta S_p(M,G) \approx c_s R_p M \tag{1.21}$$

where the coefficient c_s is positive if the membrane curves away from the polymer The entropy gain induced by the curvature of the surface is balanced by the increase of the membrane bending energy ΔE_{me}. For a symmetric bilayer segment which forms a spherical cap with area $A = \pi R_p^2$, the bending energy is given by

$$\Delta E_{me}(M) = \int dA \frac{1}{2}\kappa(2M)^2 = 2\pi\kappa R_p^2 M^2 \tag{1.22}$$

where κ is the membrane bending rigidity. By minimizing the free energy $\Delta F = \Delta E_{me}(M) - T\Delta S_p(M)$, one finds the spontaneous curvature [10, 27]

$$M_{sp}^{pm} = c_s k_B T / 4\pi\kappa R_p = \sqrt{\pi/6}(k_B T/4\kappa)\Gamma R_p \tag{1.23}$$

This induced curvature arises due to entropic interactions of the anchored polymer with the membrane. It is linear in the polymer concentration surface Γ and is larger for smaller polymer size. In [22] it is shown that the anchored polymers lead to membrane stiffening – the bilayer bending rigidity increases to a new value κ_{eff}:

$$\kappa_{eff} \approx \kappa + 0.21 k_B T \tag{1.24}$$

In contrast to the bending rigidity the bending modulus of the Gaussian curvature is found to decrease as

$$\bar{\kappa}_{eff} \approx \bar{\kappa} - 0.17 k_B T \tag{1.25}$$

The predictions for the values of the effective elastic constants (1.24) and (1.25) and the spontaneous curvature (1.23) are relevant on length scales of the order of polymer size R_p. On larger length scales, the presence of polymer mushrooms leads to inhomogeneous elastic constants of the membrane. The theoretical predictions (1.24) and (1.25) have been recently confirmed experimentally by Gompper et al. [105].

There is a second contribution to the spontaneous curvature which is also linear in Γ and arises from the size and geometry of the anchored molecules inserted into the membrane. If there is no exchange of molecules between both monolayers (flip-flop) a simple geometric consideration [26, 27] leads to

$$M_{sp}^{an} = \Gamma A_{an} / 2 l_{me} \tag{1.26}$$

Where A_{an} is the lateral anchor size (about 0.7 nm^2 [31]) and l_{me} is the thickness of the bilayer (about 4nm).

Because the membrane is fluid, the anchored polymers can diffuse and occasionally collide. These collisions between the anchored macromolecules (polymer-polymer interactions) give another contribution to the membrane curvature [26, 27]:

$$M_{sp}^{pp} = \frac{k_B T}{4\pi\kappa} b_2 \Gamma^2 R_p \tag{1.27}$$

where $b_2 = 4\pi R_p^2$ is the second viral coefficient. This contribution arises due to the polymer/polymer interactions and is quadratic in the polymer surface concentration Γ. By equating the spontaneous curvature contributions polymer/membrane (1.23) and polymer/polymer (1.27) interactions one can calculate the crossover surface concentration of the polymer [106]

$$\Gamma^* \simeq \frac{1}{4\sqrt{6\pi}\left(\frac{l_{me}}{2} + R_p\right) R_p} \tag{1.28}$$

In this way one can identify two different mushroom regimes 1 and 2. Regime 1 with $\Gamma<\Gamma^*$ is dominated by the entropically induced polymer/membrane interactions. Regime 2 is governed by the polymer/polymer interactions arising from the excluded volume [26]

In the literature the problem of the membrane shape in the point of anchoring has been considered. Three possible membrane shapes were considered in [10, 22] – smooth (spherical cap), cone-like and catenoid-like and the corresponding spontaneous curvatures were calculated. A different approach was followed in [26, 27]. By using perturbative calculations the shape profile was determined. It is cone-like close to the anchoring point and catenoid-like away from it.

1.2.2.3. Brush regime

When the mean distance between the anchored polymers is smaller than the radius of the polymer coil, the polymers overlap and form a so-called polymer brush. The overlap surface coverage, corresponding to average distance between two anchors $\xi_{an} = R_p$ is given by $\Gamma^{ov} = N^{1-2\nu} / a_k^2$ (proportional, but higher than the overlap crossover surface concentration Γ^*). The maximum coverage is reached in the dense limit $\Gamma_{\max} = N / a_k^2$. In practice it cannot be realized, because as was already mentioned, at this limit the loss of entropy from the steric hindrance by the neighboring polymers within the brush will overcome the anchoring energy.

In reference [22] is shown that in this case and for a good solvent (ν=3/5) the spontaneous curvature M_{sp} is given by

$$a_k M_{sp} \sim N^2 \left(\frac{\xi_{an}}{a_k} \right)^{\frac{13}{3}} \Gamma^{\frac{13}{6}} \tag{1.29}$$

In this case the dependency of the spontaneous curvature on the surface density of polymer is stronger than in the case of mushroom regime 2 (1.27). When the polymers are anchored on one side of the membrane (polymer brush) the membrane bends away from them. As in the mushroom regime, the anchored polymers increase the bending rigidity κ and decrease the Gaussian bending modulus $\bar{\kappa}$ [22]

$$\kappa_{eff} = \kappa + \left(\frac{\nu + 2}{12\nu^2} \right) N^3 \left(\frac{\Gamma}{\Gamma_{\max}} \right)^{\frac{3}{2\nu}} k_B T \tag{1.30}$$

$$\bar{\kappa}_{eff} = \bar{\kappa} - \left(\frac{1}{6\nu} \right) N^3 \left(\frac{\Gamma}{\Gamma_{\max}} \right)^{\frac{3}{2\nu}} k_B T \tag{1.31}$$

These results can be generalized for a bilayer with both surfaces decorated with polymers. Within a small curvature, the contributions of these brushes to the free energy are additive [17]. Thus, for the symmetric case, where the surface coverage on both sides is the same, the spontaneous curvature vanishes and the polymer induced contribution to the bending rigidity is twice the contribution by a single brush.

1.3 Experimental approach

The major subject of this thesis is a systematic investigation of the effect on the elastic properties of lipid membranes induced by anchored long polymers. The polymers are anchored asymmetrically, only on the membrane outer surface, thus inducing spontaneous curvature. As described in the previous chapter theoretical calculations [10, 22, 26, 27] predict two limiting regimes for the membrane spontaneous curvature as a function of the surface polymer concentration: *i)* at low coverage (mushroom regime) the spontaneous curvature scales linearly with the surface density of anchored polymers (see equation 1.23); *ii)* at high surface concentration (brush regime) the dependence is quadratic (see equation 1.27). In both regimes the membrane bending stiffness is expected to increase (see equation 1.24 and 1.28).

We attempt to test the predictions for the mushroom regime by monitoring the morphological changes induced on model membranes. The latter are grafted with polymers with different surface concentrations, always lower than the overlap coverage Γ^{ov}.

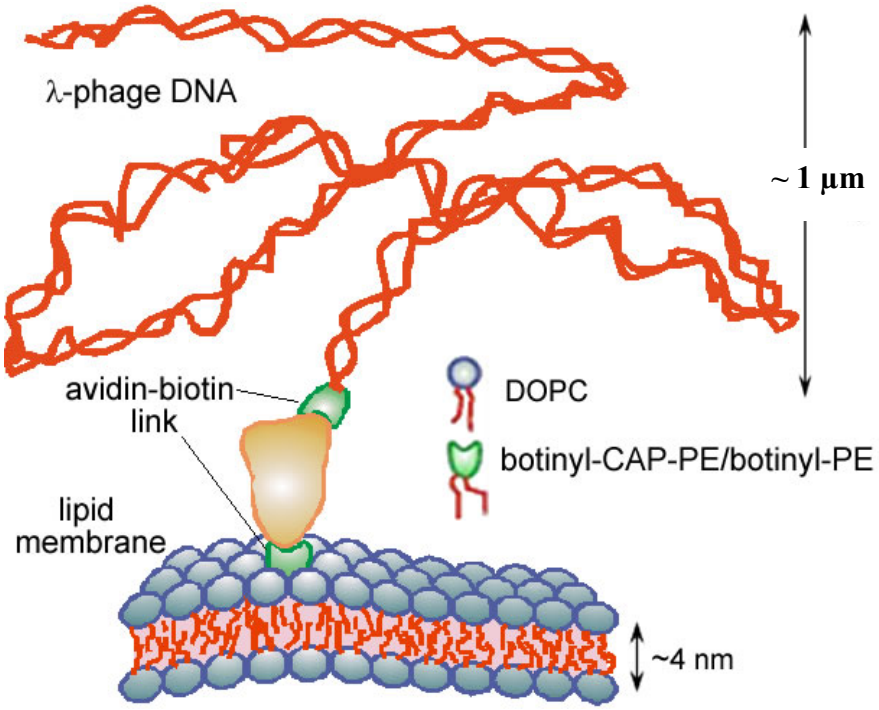

Fig 1.8: λ-phage DNA with biotinylated sticky end is anchored to a lipid membrane via avidin-biotin link. The number of the anchors is controlled by controlling the molar ratio DOPC/biotinyl-PE

Giant phospholipid vesicles, made of zwitterionic phospholipids, DOPC (18:1) and biotinylated lipid (biotinyl-PE or biotinyl-CAP-PE) (18:1), are used. The hydrophilic heads of the PE-lipids are chemically modified with biotin. The purpose of this biotin modification is to enable the molecule to make use of the strong non-covalent bond with avidin. Vesicles are swollen in the presence of avidin. The concentration of bound avidin is controlled by controlling the molar ratio of the biotinylated lipid. The ratio of bound vs. free bulk avidin is proportional to the equilibrium constant of the avidin-biotin reaction. It is assessed with ITC measurements. As long polymers we use λ-phage DNA molecules with a biotinylated 3'-"sticky" end (for details see section 2.2.2). In this way, the DNA molecule is enabled to get use of the strong non-covalent biotin-avidin linkage. When chemically altered, λ-phage DNA can be bound to the avidin, residing on the vesicle surface. Changes in the elastic properties of the membrane as DNA anchored to it are monitored via analysis of the vesicle fluctuations. The membrane spontaneous curvature increases as a function of the surface coverage. To provide a basis for comparison, the same types of measurements are performed with pure (not decorated) and decorated membranes. Because the DNA molecule is fluorescently labeled, the polymers, anchored onto the membrane are visualized with fluorescence measurements. The surface coverage of DNA is estimated with the tool of digital image processing. DNA was

chosen for several reasons: *(i)* the theoretically expected increase in the spontaneous curvature is inversely proportional to the number of monomers in the polymer chain. Due to the large number of base pairs, λ-phage DNA will prevent the model membranes from drastic morphological changes (e.g. shape transformations) – an essential element, especially important for fluctuation analysis experiments (see section 2.3.3); *(ii)* DNA can be reproducibly purified and is always monodisperse. This is an advantage, because the anchoring distance ξ_{an} depends on polymer dimensions and is kept fixed. *(iii)* DNA can be easily chemically modified and fluorescently labeled. Due to its large size, single molecules can be visualized and manipulated; *(iv)* by using proper solvent, the interaction between negatively charged phosphate groups can be completely screened (good solvent).

The experimental techniques and methods we used in this experimental investigation can be summarized as follows:

- The essential data about the surface concentration of avidin anchors, residing on the surface of a vesicle made of DOPC/biotinyl-(CAP)-PE with a given molar ratio is obtained by Isothermal Titrational Calorimetry (ITC), (see Chapter 3)
- The size distribution of extruded Large Unilamellar Vesicles LUVs) was controlled by Dynamic light scattering (DLS) (see Chapter 3)
- The excitation and emission spectra of fluorescently labeled DNA and membranes decorated with DNA were measured by fluorometry (see section 5.4)
- In order to analyze the shape fluctuations of GUVs and to determine the changes in membrane material properties as a function of the surface density of grafted DNA phase contrast microscopy and fluctuation spectroscopy are used (see Chapter 4).
- Vesicles, decorated with fluorescently labeled DNA were imaged by Laser Scanning Confocal Microscopy. High intensity laser beam and photomultiplier are essential to detect the weak fluorescence signal from single molecules (see section 5.5).
- The number of anchored DNA per vesicle is determined by digital image analysis of the confocal microscopy data. (see section 5.5)

Chapter 2

Materials and experimental techniques

2.1. Materials

2.1.1. Lipids and biotin

Three different phospholipids are used in this study: 1, 2-Dioleoyl-*sn*-Glycero-3-Phosphocholine, 18:1 (DOPC); 1, 2-Dioleoyl-*sn*-Glycero-3-Phosphoethanolamine-N-Biotinyl, 18:1 (Biotinyl-PE); 1, 2-Dioleoyl-*sn*-Glycero-3-Phosphoethanolamine-N-Cap Biotinyl, 18:1 (Biotinyl-Cap-PE), (fig. 2.1a). They have identical alkyl chains and different headgroups composition. The headgroups of Biotinyl-PE and Biotinyl-Cap-PE are biotinylated. They contain chemically linked biotin group (fig.2.1b, c). The alkyl chain linking the biotin group to the phosphoethanolamine is longer in the Biotinyl-Cap-PE molecule and if both biotinylated lipids are incorporated in a membrane, the biotin group of Biotinyl-PE will be closer to the membrane surface than the one of the of Biotinyl-Cap-PE. The PE lipid is a sodium salt, which may result in a small positive charge on the vesicles. The lipids and their mixtures (DOPC/biotinyl-PE (biotinyl-CAP-PE) = 10^6-$10^7$1, 10:1 and 1:1) were stored in chloroform. All experiments were conducted at 25^{o}C, which is far above the main phase transitions of both lipids (-17.4^{o}C for DOPC [42] and -8.1^{o}C for DOPE [43]). Therefore, at the experimental conditions, used in this work, the lipid membranes were in fluid state. Differential scanning calorimetry (DSC) experiments with extruded LUV (see section 2.2.1) and lipid molar ratio 10:1 demonstrated that phase separation does not occur and it was assumed that the lipids were homogeneously mixed.

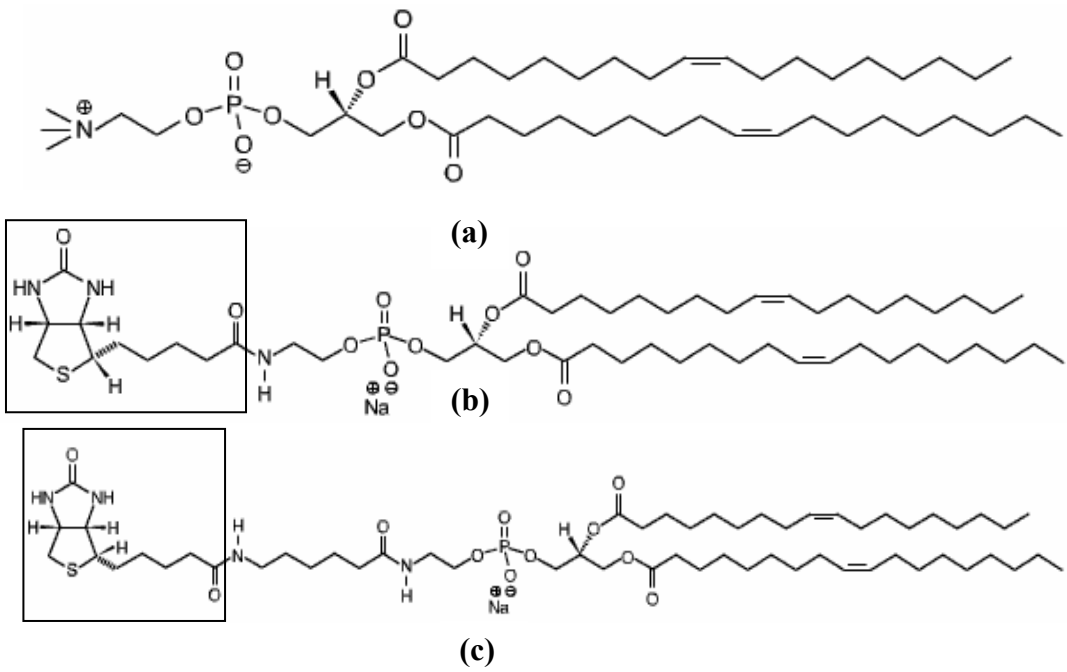

Fig 2.1: Chemical composition and structural formula of DOPC (a), Biotinyl-PE (b) and Biotinyl-Cap-PE (c). The biotin group of Biotinyl-Cap-PE has longer linker with phosphoethanolamine head. The biotin group is shaded in (b) and (c).

Biotin (also known as vitamin H) is a non-aromatic heterocyclic compound. The two rings are fused in a cis configuration and the valeric acid side chain (C2) is also cis in relation to the imidazolidone ring. A variety of derivatives of biotin are available [44] in which the biotin moiety is connected (through the 4-carboxybutyl group) to some linker molecule that can be attached directly to an oligonucleotide.

2.1.2. Avidin and streptavidin

Avidin is a basic glycoprotein with isoelectric point at pH 10 [45]. It is very soluble in water and salt solutions and its conformations are not very sensitive to changes in pH, temperature and ionic strength [44]. The protein crystallizes from high salt solutions and forms a tetragonal crystal. The crystal structure is investigated in [46] and the analysis show that avidin subunits are organized in an orthogonal eight-stranded antiparallel β-barrel (fig.2.2) (the barrel is characterized by the conventional right handed twist with strands connected by extended loops). The protein structure is tetrameric and each subunit is built of 128 amino acids. Its molecular mass and dimensions are 68 kDa [44] and 5.6 x 5 x 4 nm (estimated with X-ray crystallography [46]) respectively. The discovery of avidin by Eakin et al. [47] is closely related to the process of isolation and synthesis of biotin.

The ability of avidin to bind up to four (one per subunit) molecules of biotin with exceptionally high activity (see [44, 88, 107]) is known since the early work on this topic. Because of the very high reaction heat (-88 kJ/mol [44]), the avidin-biotin bond in known as the strongest non-covalent bond. The biotin-binding site within each subunit is located in a deep pocket with interior surface 316 $Å^2$ [46]. The pocket is coaxial with the axes of the barrel and is close to its end (fig 2.2). It contains a set of polar and aromatic amino acids residues, all of which are involved in the tight binding. The position of the residues inside the binding site appears to be especially arranged to provide an optimal fit for biotin. In fact, when the binding site is not occupied, the structure of the bound solvent resembles the shape of the biotin molecule [48]. During the course of binding, biotin replaces the network of solvent molecules, and one of the exposed loops becomes ordered and locks the biotin in the binding site. Biotin (chain B) (see Appendix Avidin pocket for details), makes hydrogen bonds to residues the Ser-16, Ser-73, Ser-75, Ala-39, Asn-12, Asn-118, Tyr-33, Thr-38 and Thr-40. This triggers the formation of a network of hydrogen bonded water molecules. It appears that binding is a random process and there are no detectable interactions between the sites. The presence of biotin completely protects the subunit to which it is bound, but it is important to notice that it does not affect the reactivity of the neighboring subunits [44]. If an avidin molecule binds to a biotinylated surface (e.g. vesicle containing biotin), the presence of wall may introduce some limitations to the binding reaction. Because biotin has to be buries inside the binding pocket, presumably avidin will have to be partially wrapped by the membrane and that will lead to steric repulsion between the surface and the molecule. Moreover, an avidin molecule probably can bind two biotins from the surface, because it has two biotin-binding sites (two subunits) close to it.

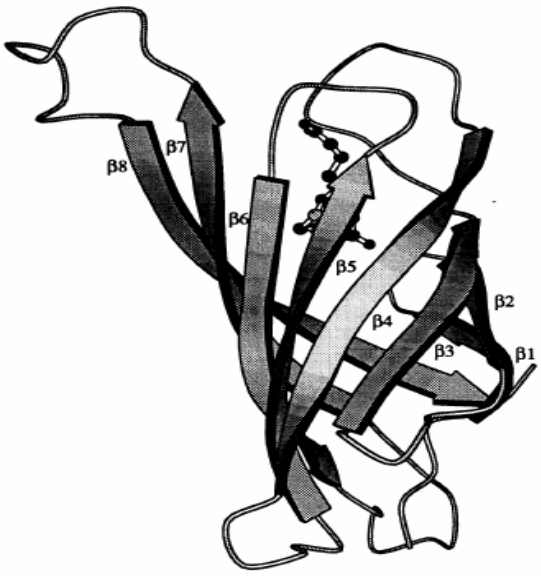

Fig 2.2: A RASMOL [46] ribbon diagram of avidin biotin monomer, with the eight strands β-barrel labeled. Biotin molecule is shown in a ball and stick model.

The avidin-biotin complex is very firm and any dissociation of biotin is so low that re-equilibration of biotin after the initial binding can be ignored [44]. The presence of bound biotin substantially increases the thermal stability of the pure avidin. The denaturation temperature increases from 85°C [44] to 132°C [49]. Moreover, the complex remains stable in

experimental conditions like 9 M urea solution, pH range 2 to 13, and is not denatured in 7M guanidine hydrochloride [50].

Streptavidin is another biotin binding protein. Although its chemical composition is (quite) different from avidin, the properties of both proteins are remarkably similar. Streptavidin also has a tetrameric structure, where each subunit can bind a biotin group with activity as high as the one of avidin and with the same reaction heat [44]. Unlike avidin, its isoelectric point is close to pH 7 and therefore it is neutral at the pH of our working buffer. Streptavidin however tends to crystallize when anchored on a biotinylated membrane [51]. This results in drastic membrane stiffening. Moreover membrane fluctuations decrease and may even vanish [51]. Avidin does not crystallize. In [51] it has been added as a non-crystallizable impurity in a 2D streptavidin crystal in order to dilute the streptavidin concentration on the biotinylated membrane surface and to allow uninhibited growth of large crystal domains. Streptavidin crystallization is pH sensitive and does not occur at pH > 7 [51]

2.1.3. λ-DNA

The abbreviation DNA originates from DeoxyriboNucleic Acid. The DNA is a polymer whose chemical composition contains four types of units (bases) – Adenine, Guanine, Thymine and Cytosine, abbreviated as A, G, T and C respectively. Every single nucleotide consists of a base, a deoxyribose sugar and a phosphate group. The bases fall in two categories - purines (A and G) and pyrimidines (C and T) (fig. 2.3.a). A purine has a pair of fused rings; a pyrimidine has only one ring. The DNA is a molecule with several levels of organization. The chemical sequence of the bases defines the primary structure of a single strand. There are higher orders of organization (e.g. the strands organize in a helical structure). Due to the specificity of the chemical structure of the bases A can only bind T (via two hydrogen bonds) and G can only bind C (via three hydrogen bonds) (fig. 2.3.a). This binding is known as a base pair (bp).

James Watson and Francis Crick elucidated the double helical structure of DNA (1953) by the detailed analysis of x-ray diffraction patterns and careful model building. Their model has the following main features:

- The DNA molecule consists of two polynucleotide strands that wind around common axes with a right-handed twist to form an approximately 2 nm diameter double helix (fig. 2.3b). The two strands are *antiparallel* (one runs from 5’ to 3’, while the other is oriented from 3’to 5’) and wrap around each other such that they cannot be separated without

unwinding the helix. The bases occupy the core of the helix and the sugar phosphate chains are coiled around its periphery.

- The planes of the bases are nearly perpendicular to the helical axis. Each base forms a base pair with a base from the opposite strand. It is the hydrogen bonding interactions (fig. 2.3a), a phenomenon known as *complementary base pairing*, that result in the specific association of the two chains in the double helix.
- The "ideal" B-DNA helix has 10 bp per turn (a helical twist of 36° per bp), the base pairs are 0.34 nm apart and the helix has a pitch (rise per turn) of 3.4 nm.
- B-DNA has two deep exterior grooves that wind between the sugar-phosphate-chains because of the helix axes passing approximately through the center of each base pair. The grooves are of unequal size, because: i) the top edge of each base pair is structurally distinct from the bottom edge, ii) the deoxyribose residues are asymmetric. The grooves are named *minor groove* (the smaller one) and *major groove* (the bigger one) (2.4b).

In this PhD-work the individual double stranded DNA molecule representing the whole genome of the bacteriophage Lambda has 48502 base pairs (λ-DNA) [40] was used. It has total length 17.2 μm [40], gyration radius Rg≈500 nm, [41] and because of the phosphate groups the whole molecule is negatively charged. It has single strand overhangs of 12 nucleotides on each 5'-end. The sequences of these overhangs are different, but complementary, because the DNA is circular in the host cells [2]. The modern molecular

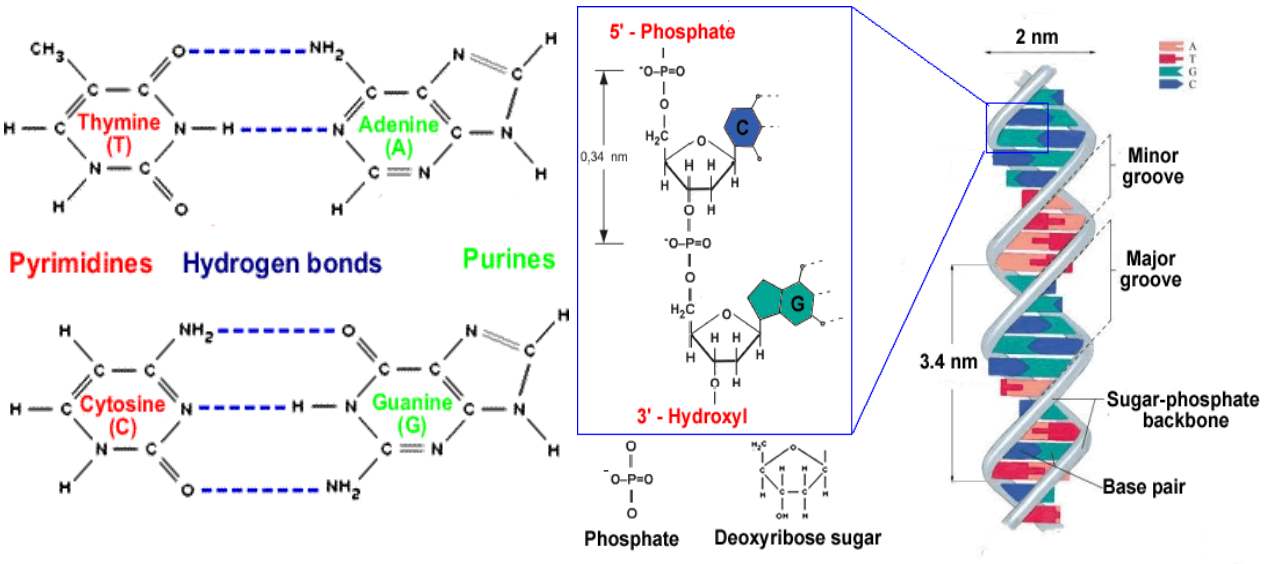

Fig 2.3: (a) The chemical structure of the DNA bases and the formation of base pairs, due to hydrogen bonding, (b) The structure of B-DNA, represented with a color-coding for the bases. A small fragment of one polynucleotide strand is zoomed to demonstrate its structure.

biology made the engineering of the DNA ends possible and specific 12 bp long nucleotides can be synthesized and ligated to one or both 5'-ends.

2.1.4. Working buffer

Almost all biological molecules like proteins and nucleic acids have charged functional groups, e.g. carboxyl and amino residues. When dissolved, these functional groups can undergo acid-base reactions and therefore the properties of the molecules may vary with the acidity of the solvent. In the experimental system investigated in this thesis one may expect that the charged phosphate and hydroxyl groups from the DNA backbone and the avidin residues will be involved in acid-base reactions. Such reactions would modify the experimental system in an uncontrollable way, but they could be prevented by keeping the pH constant. The latter requires the usage of buffer.

Due to their physiological pH [1], HEPES (4-(2-Hydroxyethyl)piperazine-1-ethanesulfonic acid) based buffers have many biological and clinical applications. Their advantages can be summarized as follows: i) low temperature sensitivity of HEPES dissociation constant [52], ii) they have been used for clinical investigations of ligand-protein interactions [53], iii) they do not serve as a sulfur source for growth of bacteria, tested under anaerobic conditions [54]. The working buffer, used for all stock solutions in this thesis, is HEPES-based: 10 mM HEPES (pK 7.47 [1]), 5 mM ascorbic acid (also known as Vitamin C, pK 4.01 [1]). The presence of ascorbic acid shifts the pH of the buffer solutions to acidic value. It was adjusted to pH 7 with NaOH. The ascorbic acid was added to reduce the bleaching of the fluorescent dye during fluorescence measurements.

2.2. Preparational procedures

2.2.1. Preparation of vesicles

Two different types of vesicles were used in this PhD work – giant unilamellar vesicles (GUV) and large unilamellar vesicles (LUV). GUV are with cell size, can be visualized with an optical microscope and allow working with individual vesicles. They were used in the fluctuation spectroscopy experiments. Due to the smaller size (50-500 nm) LUVs cannot be visualized with optical microscopy. Unlike giant vesicles, samples with a very narrow size distribution can be reproducibly prepared. LUVs were used in the isothermal titrational calorimetry (ITC) experiments.

2.2.1.1 Large Unilamellar Vesicles (LUVs)

The preparation of extruded LUVs follows the procedure outlined in [55, 56]. Chloroform solutions of 10 mM DOPC / biotinyl-PE (or biotinyl-CAP-PE) (100:1, 10:1 or 1:1) were prepared in a flat bottomed test bottle and the solvent was evaporated under nitrogen flow. To ensure the complete removal of the chloroform the samples were placed in a desiccator and dried for 2 hours under vacuum. The phospholipid film was dispersed in 2 ml of the working buffer and vortexed 3 minutes. The lipid suspension was extruded consecutively through polycarbonate membranes with pore diameters 400, 200, 100 and 50 nm (20 times through each). The applied pressure on the extruder (LiposoFast^{TM}, Avestin Inc., Ottawa, ON, Canada) pistons did not exceed 20 psi (137 kPa). The vesicles were extruded at room temperature (25^{o}C), which is above the main phase transition temperature of the lipids

2.2.1.2 Giant Unilamellar Vesicles (GUVs)

The procedure for preparation of GUV was similar to the method developed by Yang et al [57]. Chloroform solutions of DOPC/biotinyl-CAP-PE (10^6-10^7:1) with total lipid concentration of 2 mg/ml were prepared. Five droplets of the solution (about 25 μl) were deposited and spread with Hamilton® syringe on roughened Teflon® plate. Afterwards the plate was carefully placed in 10 ml bottle and dried for 6 hours under vacuum. Without any agitation, the plate was placed in an oven and hydrated for 8-10 hours in water vapor atmosphere and at constant temperature (37^{o}C). The bottle was than carefully filled with 5 ml buffer solution of sucrose with osmolarity 150-200 mOsm/g. The sucrose solution contained avidin, sufficient to bind the whole amount of biotin. The bottle was tightly closed and placed in the oven (37^{o}C). The addition of avidin to already formed vesicles was avoided, because it was causing vesicles clustering. The typical cloud of concentrated vesicle suspension was observed within 24-30 hours. The vesicles were stored in the oven until use. On the average, the vesicle sizes were in the range 10-20 μm. GUVs were observed with an optical microscope in phase contrast mode.

2.2.2. DNA botinylation

A nucleotide with sequence 5'-GGG-CGG-CGA-CCT-biotin-3' is ligated to one of the two 5'-ends of the used λ-DNA. It is complementary to only one of them. The attachment of this nucleotide to the DNA molecule is referred as DNA botinylation. (fig. 2.4). The

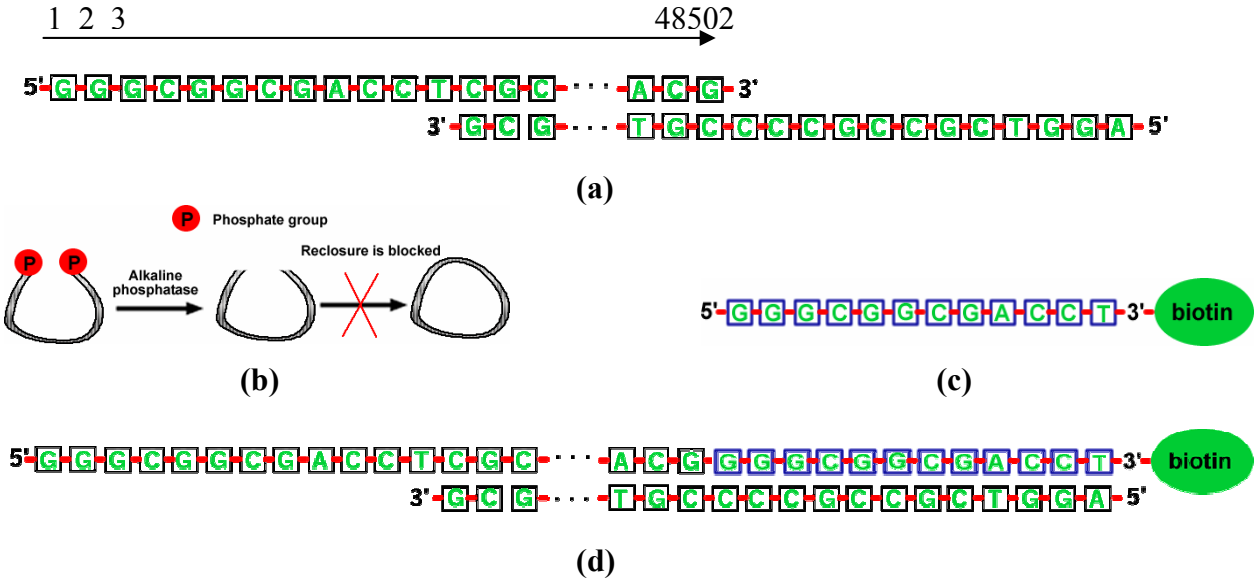

Fig 2.4: (a) The λ-phage DNA sequence [40] and both 5'-ends overhangs (sticky ends), (b) Alkaline phosphatase removes the 5'-ends phosphate groups and prevents the molecule from reclosure, (c) 12 bp long nucleotide with 3'-biotinylated end, (d) the biotin group allows binding to avidin

enzyme T4 DNA ligase catalyzes the ligation reaction. This enzyme is encoded by bacteriophage T4 [2] and facilitates a joining reaction between DNA molecules involving the 3' - hydroxyl and the 5' - phosphate termini. It also catalyzes the covalent joining of two segments to one uninterrupted strand in a DNA duplex, thus providing that no nucleotides are missing at the junction (repair reaction). Since both overhangs have complementary sequences, the presence of T4 ligase can favor the reaction between 3' and 5' ends of the same molecule. The latter process is known as recirculation (reclosure). The ligase requires 5' phosphoryl termini and if they are not present, reclosure will not be possible. To avoid reclosure we perform dephosphorylation, which is the process of removing the 5' phosphate groups. The DNA can be dephosphorylated with the enzyme alkaline Phosphatase Calf Intestinal (CIP). This enzyme catalyzes the removal of 5' phosphate groups (fig 2.4). The treatment with alkaline phosphatase prepares templates in DNA for 5'-end ligation. (The nucleotide is not treated with CIP and its 5'-phosphate group, necessary for the ligation, is present)

The dephosphorylation and ligation protocols developed in [58] are used without further modifications as follows:

Dephosphorylation protocol:

1. Incubation in thermo-mixer for 60 min at 37°C of
   - 12 µl H_2O
   - 2 µl Reaction buffer (Concentration 10 x)
   - 5 µl ($5 \cdot 10^{10}$ molecules) λ-DNA (500 µg/ml)
   - 1 µl Alkaline Phosphatase (10 Units/µl)
2. Deactivation of the enzyme for 60 min at 65°C.

Ligation protocol:

1. Incubation in thermo-mixer for 180 min at 21°C of
   - 5 µl H_2O
   - 1 µl Reaction buffer (Concentration 10 x)
   - 2 µl ($5 \cdot 10^{9}$ molecules) dephosphorylated DNA
   - 1 µl ($5 \cdot 10^{10}$ molecules) nucleotide 5'-GGG-CGG-CGA-CCT-biotin-3' (80 nM)
   - 1 µl T4-DNA-Ligase (400 Unit/µl)
2. Addition of 15 µl H_2O

The biotinylated DNA was stored in a freezer at -20°C.

2.2.3. DNA fluorescent labeling

We attempt to visualize the biotinylated DNA by labeling it with the fluorescent dye TOTO-1 (513/531). The dye is essentially not fluorescent except when bound to DNA or RNA. It has very high affinity for nucleic acids [59] and thus dye-DNA complex dissociation almost does not occur in the dilute solutions needed to resolve single molecules. The ratio TOTO-1/bp is 1/5 which is a reasonable compromise, because higher ratios may result in self quenching, while lower ratios would lead to low fluorescence signal (fluorescence intensity).

One may expect that the intercalation of TOTO-1 into the double helix modifies the DNA structure and physico-chemical properties. Indeed, the labeling with this molar ratio dye/bp results in an increase of the total DNA length with approximately 30% [60], i.e. the total length of λ-DNA reached 22 µm (reported in [61]). Just for comparison, similar labeling ratios with other dyes like ethidium bromide and DAPI reflect in an increase of 40% and 17% respectively [62]. The DNA persistence length is not sensitive to the presence of the dye and remains its native value of about 50nm [63], even at very high ratios dye/bp (up to 1/3) [60].

The fluorescent labeling protocol was as follows:

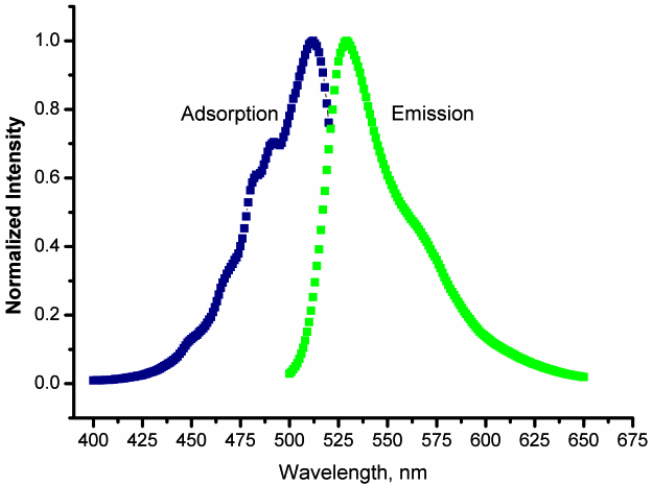

Fig 2.5: Adsorption and emission spectra of TOTO-1/λ-DNA complex at a dye/bp ratio of 1:5. The concentration of DNA is 6.2×10^{-10} M (3×10^{-5} M bp) for both adsorption and fluorescence measurements. All spectra were normalized to facilitate comparison

A Mixture of DNA and dye with molar ratio dye/ bp=1/5 was prepared in purified and deionized water under reduced illumination. The vessel with the mixtures was tenderly shaken for 2 hours in a thermo-mixer at room temperature. The adsorption and emission spectra of the complex were measured (fig 2.5) with fluorometer and compared with the catalog data [64]. Because the fluorescent dye is susceptible to photo degradation, the vessels with the solutions of the dye and the DNA-dye complexes were wrapped in aluminum folio and stored at -20^{o}C until use. The samples were diluted in the working buffer prior to every experiment.

3. Experimental techniques

3.1. Isothermal titrational calorimetry (ITC)

Almost every physical (non covalent binding) and chemical reaction are accompanied by a release or uptake of heat. An experimental method to measure this heat is Isothermal Titrational Calorimetry (ITC), which measures the heat associated with mixing and reaction of two solutions of different compositions. In the recent years ITC has become the technique of choice for thorough studies of association reactions, particularly in biochemical processes, involving specific non-covalent interactions between a ligand and a macromolecule (e.g. antigen-antibody or ligand-receptor interactions) [65]. The advantages of the technique are the modest experimental constraints for obtaining data, the small working volume needed for one measurement, the relatively fast data acquisition (e.g. ~3 hours/experiment), and high sensitivity (1μcal for 1 ml cell,[65], [66])

In many cases it is desirable to obtain information about the equilibrium of a chemical process. Usually reaction equilibrium is characterized by the change in Gibbs free energy ΔG, defined as

$$\Delta G = \Delta H - T\Delta S \qquad (2.1)$$

where ΔH and ΔS are the changes in the system enthalpy and entropy respectively. Among a variety of techniques, used to determine equilibrium constants, only ITC with a single measurement can

- Directly determine the equilibrium constant of a process K, ΔG, and ΔH.
- From these values to calculate the entropy change ΔS

Moreover by performing measurements at different temperatures, the heat capacity C_p of the specimen can be obtained.

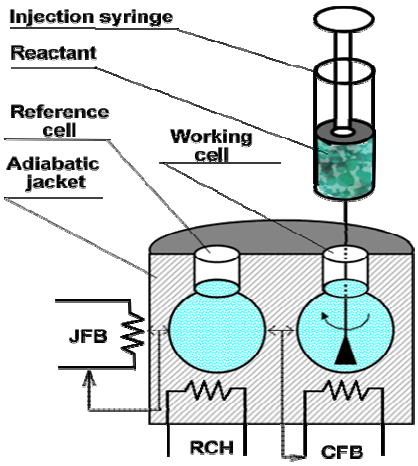

Fig 2.6: Detailed view of the ITC cells, the adiabatic jacket and the location of all heaters and all electric feedbacks [reproduced from [65], [66].

A schematic diagram of the working setup and principle of a titrational calorimeter is shown in fig. 2.6. The machine has two identical cells – a reference cell and a measuring cell, which are surrounded by an adiabatic jacket. Both have the same volume of approximately 1ml, which in our machine (VP-ITC Microcalorimeter, MicroCal, MA, USA) is 1.442 ml. The reference cell is filled with the same solvent/buffer as the one in which the reagent in the measuring cell is dissolved. Usually the measuring cell contains a solution of "target" molecules, and a reactant is injected (titrated) via a computer controlled syringe. The content of the measuring cell is constantly stirred 300-500 rpm (typically 350 rpm) by the syringe flat tip. The reactant, interacting with the target molecules, is injected in small aliquots of typically 5-10 µl (10 µl for all experiments, presented in this thesis). This results in a consumption or release of heat in the measuring cell. The calorimeter is working in a power compensation mode, which means that all heat effects arising from the injection are actively balanced by the machine feedback keeping the cells at the same temperature. In practice this is realized by a very precise measurement of the temperature difference between the two cells. The reference cell is heated constantly with a very low power (Reference Cell Heater or RCH). The mixing and the reaction processes can be considered as "isothermal" within the duration of the experiment, because the change in temperature is very low (30-60 mK/h) [65]. The working cell is equipped with another heater (Cell Feed-Back or CFB), the power of which is controlled by a feedback mechanism eliminating every temperature difference between the reference and the measuring cells. If any heat is released or consumed in the measuring cell due to the injection of reactant, a

change in the CFB power is required to restore identical temperatures in both cells. The heat flow of CFB is measured and recorded as a function of time via computer with a special data acquisition board. The adiabatic jacket of the instrument is heated by a third heating system (Jacket Feed-Back or JFB) keeping the temperature of the adiabatic shield exactly the same as the one of the reference cell - in the absence of temperature gradient the cell cannot exchange any heat with the environment..

An instrument equilibration precedes every ITC experiment. The purpose of this equilibration is to set the temperatures of both cells and the adiabatic jacket to the desired values. After a stability test (maintaining temperatures for a certain period), the machine baseline is fixed. Every injection produces a heat peak, which is due to addition of certain amount of reactant into the measuring cell. The integration of the heat flow over time yields the heat per injection. The time integral between consecutive injections is set in such way to allow equilibration of the system, e.g. the heat signal reaches back the baseline. The integration is accomplished over the area, delimited by the heat peak signal and the baseline. The released/adsorbed heat per peak can be related to the equilibrium constant of the process and ΔH via a binding/insertion model.

3.2 Microscopy observations on giant vesicles (GUV)

3.2.1. Overview

Light microscopy provides a two-dimensional magnified image of the specimen. It allows us to observe fine details of the investigated object and in certain cases (confocal microscopy) - to reconstruct the 3D image. The specimen can be positioned, oriented and focused precisely. The brightness and the contrast of the image can be adjusted to bring out desired features of the specimen structure. Equipped with a CCD camera and computer controlled accessories, e.g. frame grabbers, micropipette manipulators etc, the optical microscope is a powerful tool to study the micro-sized world.

The optical resolution of a microscope determines how well the small details of the specimen will be resolved. It is defined as the ability to distinguish two very small and closely-spaced objects at distance d_{min} as separate entities.

$$d_{\min} = 1.22\left(\frac{\lambda}{NA_{obj} + NA_{cond}}\right) \tag{2.2}$$

Fig 2.7: Numerical aperture (NA) of an optical device (picture adapted from [68]

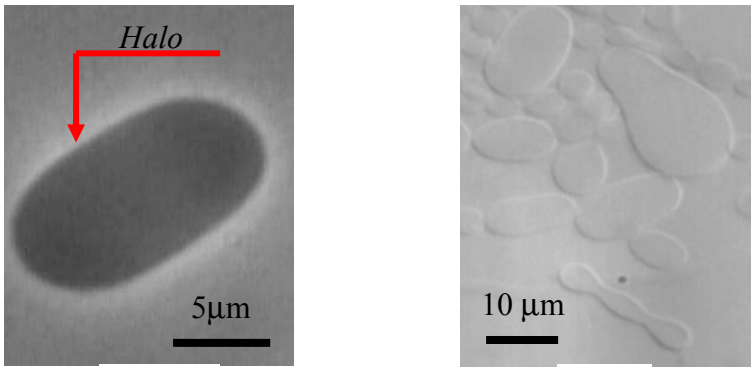

(a) **(b)**

Fig 2.8: Specimens observed in transmitted light (a) Lipid vesicle observed with a phase contrast 40x objective;(b) Polymrerozomes observed with a DIC 40x objective [81].

where NA_{obj} and NA_{cond} are the numerical apertures of the objective and condenser respectively and λ is the wavelength. The numerical aperture of an optical device is define as

$$NA = n\sin(\theta) \tag{2.3}$$

where n is the refractive index of the medium between the specimen and the device (objective or condenser) lens and θ is the halve cone angle of light captured by the objective (fig. 2.7). The resolution of a typical optical microscope is about 0.2 µm. The sizes of GUVs are in the range 0.5-100 µm. Therefore the giant vesicles can be observed and investigated with different methods of optical microscopy: phase contrast microscopy, differential contrast microscopy, confocal microscopy etc.

3.2.2. Phase contrast microscopy

The living cells and many other biological specimens belong to the class of phase objects that are difficult to study with ordinary bright field microscopy. Phase objects are called the unstained samples that do not adsorb light (do not affect the intensity), but slightly alter the phase of the light diffracted by them, usually by retarding with approximately ¼ wavelength as compared with the undeviated light passing through or around the specimen unaffected. The human eyes can perceive only changes in light amplitude (intensity). In the early 1930's Zernike developed a method, now known as Phase contrast microscopy, for generating contrast in biological specimens , changing these invisible phase differences into observable amplitude differences By speeding up the direct light with ¼ wavelength Zernike created a phase difference of ½ wavelength between the light, deviated from the investigated

object, and the direct light. As a result, the direct and diffracted beams are able to produce a destructive interference. Such a procedure results in the details of the image appearing darker against a lighter background (fig. 2.8a).

Lipid vesicles, just like the living cells, are unstained objects and the phase contrast microscopy is a convenient tool for their visualization and observation. In experiments usually the contrast is enhanced by using solutions with different refractive indexes inside and outside the vesicle, e.g. the vesicle shown in fig. 2.8a encompasses sucrose solution, while the external solution is glucose one. The vesicle is surrounded by a bright white stripe, which usually is referred as halo. The halo effect appears due to imperfections in the elements of the phase contrast optical system [67]. Due to the very steep gradient in the grayscale gamma between the specimen and the bright halo, the vesicle edge can be very precisely detected. The last feature is essential for the contour detection of fluctuating vesicles, used in the fluctuation spectroscopy [11].

3.2.3. Differential interference contrast microscopy (DIC)

Some unstained specimens are nearly transparent, and relatively thick, such as whole cells. Thick specimens do not give a clear phase contrast image. This section presents a method for obtaining a contrast image from this type of specimens, the Differential interference contrast (DIC) microscopy. The illumination in DIC consists of a beam of polarized light. The beam is separated (by using a Wollaston prism, [67]) into two ones, which have different polarizations and slightly different paths. The distance between the beams is less than the resolving power of the objective. The split light beams enter and pass through the specimen where their wave paths are altered in accordance with specimen's varying thickness, slopes and refractive indexes. After passing through the specimen and the objective lenses, both beams are focused above the rear focal plane where the horizontal separation between the two beams is removed (by a second Wollaston prism). As a final step, the two beams are converted to the same polarization angle. Thus both beams can interfere in the microscope intermediate image plane and to produce amplitude contrast. This contrast reflects the optical path difference between the two beams that was introduced by the specimen.

In contrast with the phase contrast microscopy the halo effect is not present in the DIC image (fig. 2.8.b). The image has a very realistic three-dimensional appearance. This appearance however is not an entirely true representation of the specimen, because it can be

easily changed, by adjusting the movable Wollaston prism. The latter makes the DIC microscopy not a very appropriate method for measuring distances, which is essential if a specimen quantification is needed (e.g. in the experiments with vesicles). DIC however has numerous advantages as compared to phase contrast microscopy – the possibility to provide optical staining (color), precise focusing in the focal plane (without confusing images from above and below it), and excellent resolution. The micropipettes technique experiments (used exclusively for vesicle study) are usually conducted with DIC microscopy.

3.2.4. Fluorescence microscopy

Fluorescence microscopy is one of the most powerful experimental techniques in biomedical, biophysical and biochemical research. Depending on the nature of the investigated object (entire cells, cell organelles, single molecules, the product of chemical reactions, etc) or on the type of collected information (e.g. qualitative or quantitative) different techniques of fluorescence microscopy can be used. The technique of attaching a fluorochrome molecule to an antibody was developed by Albert Coons in 1941 [68]. In 1950 Coons and Kaplan [68] developed the fluorescein isothiocyanate (FITC) immunofluorescence which today is widely used for localization of single molecules. In 1991, B.J. Trask [69] described a method of fluorescently labeling specific sequences of DNA. The method is known as fluorescence *in situ* hybridization (FISH). Today there are methods for direct labeling of the DNA probe with a fluorescent molecule. In this thesis is used such method and λ- DNA is stained with TOTO-1 (see section 2.2.3). In 1992, D.C. Prasher et al. [70] cloned the jellyfish gene which codes for the "green fluorescent protein" (GFP). It is used as a fluorescent indicator for monitoring gene expression in a variety of cellular systems, including living organisms and fixed tissues.

The basic task of the fluorescent microscope is to permit excitation light to irradiate the specimen and then to separate the much weaker re-radiating fluorescent light from the brighter excitation light. Thus only the emitted light reaches the eye or other photosensitive detector (e.g. CCD camera or photographic film). Usually the fluorescently labeled object shines against a dark background with sufficient contrast to allow detection. Very often, in order to enhance the contrast, the images are made by using a combination of fluorescence and DIC microscopy, taking advantages of the feature of both contrast enhancing techniques. There are two common problems, appearing in each fluorescence microscopy measurement – *photobleaching* and *quenching*.

The phenomenon of *photobleaching* (also commonly referred to as *fading*) occurs when a fluorescent dye permanently loses the ability to fluoresce due to photon-induced chemical damage and covalent modification. The dye is not destroyed but rather irreversibly photochemically altered. The lifetime (when fluoresce) of the dye may vary from less than a minute (observed in this work) up to 10 minutes [68]. The photobleaching can be reduced by limiting the exposure time of the dye to illumination or by lowering the excitation energy. However, these approaches also reduce the measurable fluorescence signal. As alternative methods one may use some of the wide variety of synthetic antifade reagents, which can significantly reduce the rate of photobleaching. In this work, 5 mM ascorbic acid was added in the working buffer as antibleaching component.

The fluorescence *quenching* is a kind of non-radiative relaxation from excited energy levels to the ground state (see Jablonski diagram in *Appendix B*). It arises from a variety of competing processes that induce such relaxation, which may be either intramolecular or intermolecular in nature. Because non-radiative transition pathways compete with the fluorescence relaxation, they usually dramatically lower or, in some cases, completely eliminate emission. Most quenching processes act to reduce the excited state lifetime and the quantum yield of the affected dye molecules. In order to avoid quenching, the DNA molecules, used in this work was labeled with ratio dye/bp=1/5 (higher ratio would lead to frequent collisions between the dye molecules and therefore to quenching).

3.2.5. Confocal laser scanning microscopy

Confocal laser scanning microscopy (CLSM) is a relatively new light microscopy imaging technique which has found wide applications in the biological sciences [71]. Due to the sharp focusing of the laser beam, the illumination of the points above and below the area of interest is eliminated. Moreover, the light emitted from the sample is focused on the confocal pinhole, which eliminates the fluorescence from the out of focus points. In comparison with an ordinary fluorescent microscope, where the excitation beam is focused on a relatively large area (much larger than the investigated object) in CLSM the excitation beam can be focused only on the specimen. The corresponding intensity of the fluorescence emission is much higher (and therefore much easier for detection) in the experiments conducted with CLSM. Such sharply focused laser beam, however, results in faster photobleaching of the fluorescent dye.

In order to determine the number of anchored and fluorescently labeled DNA to a vesicle, one has to perform up/downs scans over its entire surface and to detect the fluorescence emission from every single molecule. The vertical resolution of an optical microscope is usually about 3 times worse than the lateral one (which is about 0.2 μm) and is entirely comparable with the gyration radius of a λ-DNA molecule (0.5 μm, [41]). Thus the anchored DNA cannot be resolved with up/down scans, because its size is below (or comparable) with the vertical resolution. The corresponding vertical resolution of a confocal microscope is 0.3 μm, which is sufficient to visualize the polymers, residing on vesicle surface.

Maybe the main advantage of CLSM is its ability to make 3D optical cross sections of a specimen – such as an entire cell a piece of tissue etc. A computer-controlled CLSM produces digital images which can be processed and analyzed with the tools of digital images analyses

2.3. Fluctuation spectroscopy of prolate vesicles

2.3.1. Overview

Two principal parameters characterizing the elastic energy of an amphiphilic interface are the bending modulus κ, which sets the energy scale and the spontaneous curvature M_{sp}, which describes the preferred curvature of the interface. Although these two parameters can be varied by various control parameters in the lab [71], their absolute values cannot be directly measured. There are several experimental methods which yield information about the bending modulus – tether formation [72], deformation of giant vesicles in electric field [73], flickering spectroscopy of giant quasi-spherical vesicles [37, 38], thermal shape fluctuations of tubular vesicles [74], micropipette aspiration [3,75] and neutron scattering [76], but none of them gives information about the spontaneous curvature. The knowledge of the spontaneous curvature is desirable for several reasons: *i)* it plays the key role in determining the morphology of bio-membranes, lipid vesicles and polymrerozomes [3, 77]; *ii)* it is crucial for maintaining the spatial organization of traffic between, cellular organelles and the plasma membrane [78]; *iii)* it is believed that the functions of some membrane proteins are regulated by monolayer spontaneous curvature [15]. In spite of its importance, only one experimental method for the measurement of the spontaneous curvature has been developed [11]. It is a straightforward procedure, based on the analysis of thermal fluctuations of giant non-spherical

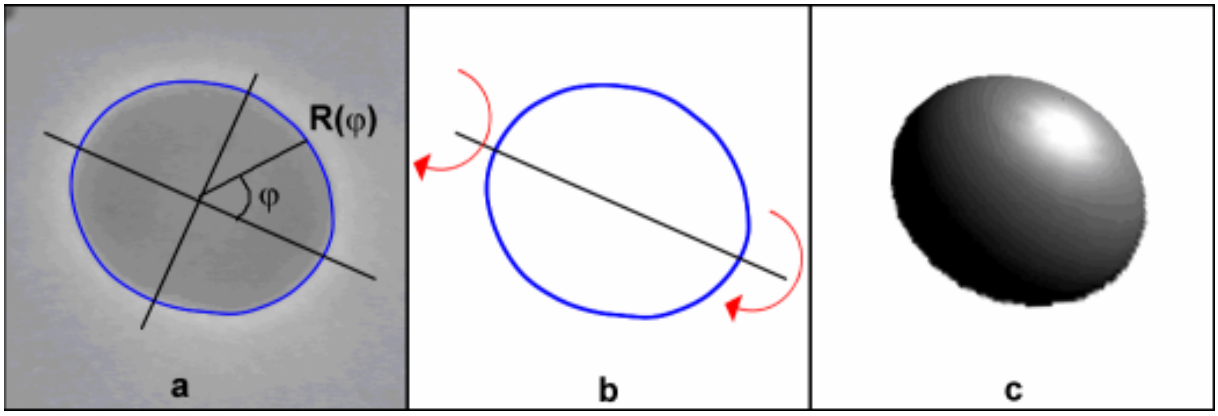

Fig 2.9: (a) A 2D image, of a fluctuating vesicle placed in the focal plane of the phase contrast objective. The contour is represented in polar coordinates (R,φ). The steep intensity gradient between the characteristic light halo and the dark vesicles separates the exterior and interior of the vesicle, b) every closed contour is rotated around the axis of symmetry of the prolate vesicle, (c) 3D vesicles morphology is inferred from the rotational shape [11].

vesicles. The method deals with a branch of axisymmetrical vesicle shapes, called "prolates", because of their up-down symmetry and resemblance to prolate ellipsoids (when their reduced volume is not too much smaller than unity). The region in the ADE phase diagram to which these prolate vesicles belong is shown in fig. 1.5 (section 1.4). Vesicle fluctuation spectrum contains information about both, the spontaneous curvature and the bending modulus [79]. By employing this method it is possible in a single experiment to measure both elastic properties simultaneously

At room temperature all non-spherical vesicles, due to excess of free area undergo thermal fluctuations. If a fluctuating prolate vesicle is "fixed" in the focal plane of the microscope (remains there for time, longer than the experiment) its fluctuation spectrum can be analyzed and yields information about κ and M_{sp}. The complete procedure of extracting the elastic constants from the fluctuation spectra is described in details elsewhere [11, 79]. Here we will outline the basic steps to be followed to obtain these data.

2.3.2. Contour detection and digitization

Experimentally, series of 2D images of fluctuating vesicles are recorded with a CCD camera and stored in the computer memory. There the images are analyzed and a closed contour around a vesicle is detected. The algorithm needs between 0.4 and 0.6s to find a contour, depending on the vesicle size. Thus for a video frequency of 30 frame/s only every

15th frame is processed. If a coordinate system in which the x-coordinate lies along the long axis of the vesicle is chosen, the contour can be represented in polar coordinates (R,φ) as:

$$R(\varphi) = R_0 \left\{ 1 + \sum_n a_n \cos(n\varphi) + \sum_n b_n \sin(n\varphi) \right\} \qquad (2.4)$$

where the angle φ is measured from the positive x-axis (fig. 2.9). In eq. (2.4) the contour is expanded in Fourier series and the amplitudes $\{a_n, b_n\}$ are numerically calculated. Time dependent amplitudes encode the full experimental information. The first (linear) term in (2.4) describes a circle with radius R_0. Nonzero coefficients describe deviation from the circle. Theoretically, for every axisymmetrical shape like prolate, the amplitudes b_n are zero and are not a subject of further consideration. The amplitudes of odd modes should average to zero for an up/down symmetric vesicles. However, $\langle a_3 \rangle$ typically has small, but statistically significant nonzero value [11]

Vesicles fluctuate around their equilibrium shape, described by the ADE model. These equilibrium shapes, however, are for T=0. Since all experiments are conducted at room temperature, one should consider the equilibrium shapes at that temperature. The equilibrium shape can be found by statistical analysis of shape fluctuations. A quantity yielding information about the mean shape of the thermal fluctuations are the mean square average values of the amplitudes: $\langle a_n^2 \rangle = \langle (a_n - \langle a_n \rangle)^2 \rangle$. When the thermal fluctuations are small, they obey Gaussian distribution and their contribution to the mean square amplitudes goes like [79]:

$$\left\langle a_n^2 \right\rangle \propto \frac{k_B T}{\kappa} \qquad (2.5)$$

When the mean shape amplitudes are found, one has to deduce the zero temperature information from the room temperature data in order to compare experiment with existing theoretical predictions.

2.3.3. Monte Carlo simulations

The data about the membrane elastic properties, obtained with the fluctuation spectroscopy, is qualitative. The method yields a dimensionless number, proportional to their real values. The latter can be obtained when the measured fluctuation spectra are matched to the corresponding spectra of vesicles, generated with Monte Carlo simulations. The simulations use the full Hamiltonian of the ADE model and take into account the contribution

of the gravitational forces acting on the vesicle. The complete procedure of matching the experimentally measured fluctuation spectrum with the spectrum generated with such simulations is described in details elsewhere [80]. For a given vesicle, the bending rigidity κ, the spontaneous curvature M_{sp} and the reduced volume v are determined simultaneously.

Chapter 3

Binding of avidin to biotinylated membranes (ITC study)

3.1. Introduction (overview and motivation)

The avidin-biotin bond is known since the early 1950's and due to its high affinity has been widely exploited for various physical and biological applications [82-86]. Although the binding reaction is relatively well studied, its efficiency may depend on reaction conditions such as pH [87], ionic strength [44, 88], temperature [83] etc. Of course, one may expect different reaction efficiency in systems with different architecture: *(i)* binding of free avidin to free biotin; *(ii)* binding of free avidin to the surface of biotinylated membrane (studied in this chapter); *(iii)* binding of a biotinylated molecule (DNA, antibody, etc) to avidin-lipid membrane complex (this case was used further but due to the very low concentrations of DNA, used in our experiments was not studied with ITC; see machine sensitivity discussion below).

A detailed investigation of binding streptavidin to biotinylated giant vesicles was performed by Ratanabanangkoon et al. [51]. The authors showed that such binding is possible, but depends very strongly on pH. Streptavidin tends to form two-dimensional crystals on the membrane surface, which results in a drastic membrane stiffening [51]. The latter effect suppresses membrane fluctuations, which are essential for the fluctuation spectroscopy used in this work (see section 2.3.3). Avidin, on the other hand, does not crystallize, as required in our experiments and was chosen as a better biotinylated membrane – DNA linker.

Unlike streptavidin, the isoelectric point of natural avidin is at pH 10. Thus the protein molecule will have a positive net charge at physiological pH (pH 7). The presence of charge may involve electrostatic (unspecific) interactions between the membrane and the protein, may influence the equilibrium of avidin binding to biotin, and thus, alter the reported very high equilibrium constant K (see reference [44], [88] and [107]). Because the reaction

product depends on reaction conditions, it is not known what will be the relation between free (bulk) avidin, unoccupied biotinylated lipids (incorporated in a lipid membra ne) and formed avidin-biotin bonds, under the reaction conditions of our experiments. The key question to be answered is how much avidin will bind on a vesicle with a given surface density of biotin at given experimental conditions. This question is of central importance, since by varying the number of anchoring sites (avidin-biotin complexes) on a vesicle surface one may control the surface density of DNA to be anchored. Binding of avidin to biotinylated lipid membranes has been studied with AFM [84], fluorescent microscopy [85] and equilibrium dialysis [88]. Qualitative data have been obtained, but detailed quantitave information about the binding process is still missing.

Such information we attempt to obtain by using high sensitivity Isothermal Titrational Calorimetry (ITC) (see section 2.3.1).

We titrate avidin solutions with solutions of biotinylated large unilamellar extruded vesicles (LUV). The amount of biotin on the membrane is defined by the DOPC/biotinyl-PE molar ratios used to prepare the vesicles. The ITC is highly sensitive, and can measure reaction heats down to about 1 μcal for 1 ml volume. The enthalpy ΔH of avidin-biotin reaction has been determined by Green [50] and is about -88 kJ/mol. Because the thermal resolution of the instrument is about 1 μcal it is straightforward to calculate the minimal number of necessary bonds which would generate a measurable signal – the concentration of available for binding biotin should be above 10^{-8} M. The typical concentration of biotin used with swelled GUVs is about 10^{-11} M. To achieve detectable signal for the ITC measurement we use higher concentration of biotin. The experimental system with best performance was found to be 10 mM vesicle solutions with DOPC/biotinylated lipid molar ratio of 10:1[95]. The performed measurements can be classified in three groups depending on the concentration of biotin relative to the concentration of avidin in the working cell:

1. *Excess of avidin.* In this case the heat flow throughout the measurement should remain approximately constant. Presumably, all accessible biotin groups introduced with each injection interact with the bulk avidin in the measuring cell. The injection volume of biotinylated vesicles solution is constant, and the produced heat per injection is expected to be constant as well.

2. *Intermediate case (Molar ratios close to 1:1 avidin to biotin)*. Maybe the system of greatest complexity is the one with comparable amounts of avidin and biotin. Initially the avidin is in excess and the measured signal should be approximately constant as in the previous case. With increase in the amount of injected biotin in the cell (i.e. by further

injections), the amount of available for binding avidin will decrease, resulting in a dropping down of the injection signal.

3. *Large excess of biotin*. The expectations are for a very fast exhaustion of all available avidin followed by leveling out of the injection signal. When the whole amount of avidin is bound the only signal to be measured should originate from dilution of cell content (or injected vesicle dilution).

The lipid membranes used in these experiments (made of DOPC and biotinyl-PE/biotinyl-CAP-PE) are neutral, but zwitterionic. Due to the presence of ions in the working buffer (10 mM HEPES, 5 mM ascorbic acid) a neutral vesicle can obtain a small charge. Indeed, ζ-potential measurement with extruded vesicles (molar ratio DOPC/biotinyl-CAP-PE 10:1), demonstrated that the latter have surface potential of *-35* mV. Membrane surface potential was estimated theoretically with Gouy-Chapman theory [31] (we assumed that the working buffer completely dissociates and each biotinyl-CAP-PE has an uncompensated negative charge of -1 while the other lipid is neutral. Indeed, extruded vesicles of DOPC did not exhibit any potential. The calculated value of the surface potential of DOPC/biotinyl-CAP-PE vesicles is *-40* mV, which is in good agreement with the experimentally measured potential. Because avidin has a positive net charge at the working pH, one has to take into account the electrostatic interactions between the protein and the membrane. In fact, due to attractive interactions the avidin concentration close to the membrane is larger than the bulk equilibrium concentration. If the total bulk concentration of avidin is $C^t_{A,0}$, then the corresponding concentration at (close to) the membrane surface will be:

$$C^t_{A,m} = C^t_{A,0} \exp\left\{-\frac{zF\psi}{RT}\right\} \tag{3.1}$$

where *z* is the protein charge (note that at the working pH avidin is slightly positively charged), *F* is the Faraday's constant and ψ is the membrane surface potential. For example if the avidin charge is *z=1*, then from (3.1) one finds that $C^t_{A,m} \approx 4C^t_{A,0}$. From here as total bulk concentration (close to the membrane surface) will be referred $C^t_{A,m}$. $C^t_{A,0}$ is controlled experimentally (total protein concentration in the measuring cell), but $C^t_{A,m}$ is the relevant concentration when binding to a biotinylated membrane is considered.

As explained in section 2.1.2., each avidin molecule has four identical avidin binding sites (*ABS*) and when vesicles are titrated in avidin, every *ABS* can bind a biotin. However, due to geometrical constraints (the biotin groups are not free but fixed in the two dimensional

matrix of the bilayer) it is possible that not four ABS participate in the binding process. Thus one has to take into account the effective total concentration of ABS, C_A^t, rather the total concentration of avidin $C_{A,m}^t$. Both concentrations are related as follows:

$$C_A^t = nC_{A,m}^t, \quad n = 1..4 \tag{3.2}$$

Further in the text it will be demonstrated that when averaged over an ensemble of avidin-biotininylated vesicles *n* can have a non-integer value. The total concentration of biotin, injected into the working cell is $C_{B,0}^t$. Only about 60% of it, however, will be on the outer surface of the vesicle and therefore [65]- available for binding. The total concentration of available for binding biotin $C_{B,0}^t$ is then related to C_B^t as

$$C_B^t = 0.6C_{B,0}^t \tag{3.3}$$

We consider the binding process as a chemical reaction between an ABS (*A*) and available biotin (*B*). Then if we denote with *ΔH* and *AB* the reaction enthalpy and the formed avidin-biotin bond, the equilibrium of the system can be described as

$$A + B \underset{}{\overset{K}{\rightleftharpoons}} AB + \Delta H \tag{3.4}$$

Here *K* is the equilibrium constant:

$$K = \frac{C_{AB}}{C_A^f C_B^f} \tag{3.5}$$

where C_{AB}, C_A^f and C_B^f are the concentrations of the formed avidin-biotin bonds, free *ABS* and free available biotin respectively. The equilibrium constant yields the necessary relation between the bulk concentrations of reactants (*ABS* and biotin) and the concentration of the complex. The mass balance equation of a chemical reaction states

$$\begin{aligned} C_B^f &= C_B^t - C_{AB} \\ C_A^f &= C_A^t - C_{AB} \end{aligned} \tag{3.6}$$

Thus, for the equilibrium constant by combining (3.5) and (3.6) we obtain:

$$K = \frac{C_{AB}}{(C_A^t - C_{AB})(C_B^t - C_{AB})} \tag{3.7}$$

This equation can be rewritten and solved for to the unknown concentration C_{AB}:

$$(C_{AB})_{1,2} = \frac{1}{2}\left(\frac{1}{K} + C_A^t + C_B^t\right) \pm \frac{1}{2}D \tag{3.8a}$$

$$D = \sqrt{\left(\frac{1}{K} + C_A^t + C_B^t\right)^2 - 4C_A^t C_B^t} \geq 0 \tag{3.8b}$$

The determinant (3.8b) is never negative; both solutions of the quadratic equation (3.8a) are real. The bigger root is non-physical, because the concentration of the product cannot exceed the total concentration of the reactants. Further we will use the obtained expression for the concentration of formed bonds to interpret the heat release in the ITC experiments.

3.2. Experimental procedure and data analysis

All ITC experiments are conducted with freshly extruded LUVs with diameter 60-70 nm. Prior to every experiment, the injection syringe is filled with vesicles, containing available for binding biotin with total concentration C_B^t. The working cell is filled with protein solution with effective concentration of *ABS* C_A^t. The vesicles are injected in fixed aliquots of volume V_{inj}=*10*μl. The timing between two consecutive injections, depending on the avidin concentration, ranges between 7 and 15 min. With every *i* injections, the reaction volume increases as:

$$V_{cell}^i = V_{cell}^0 + iV_{inj} \tag{3.9}$$

Here V_{cell}^0 is the initial cell volume (for our setup $V_{cell}^0 = 1.442$ ml). Every injection produces a characteristic heat peak, the integration over time of which gives the equivalent *heat per injection,* h_i. If ΔH (as defined before) is the enthalpy of formation of avidin-biotin bond, then the relation between h_i and ΔH is

$$h_i = \delta C_{AB,i} V_{cell} \Delta H + h_{dil} \tag{3.10}$$

where $\delta C_{AB,i}$ is the change in the concentration of formed ABS-biotin bonds as a consequence of the i^{th} injection and h_{dil} is the heat associated with dilution of the vesicles and the protein solution. The heat of dilution is measured in two separate experiments with injections of vesicles in buffer and buffer in avidin. Within the experimental error h_{dil} does not change with injection number and is almost constant (for fixed vesicle and protein concentrations). It was determined to be 4 μcal and further was subtracted from the

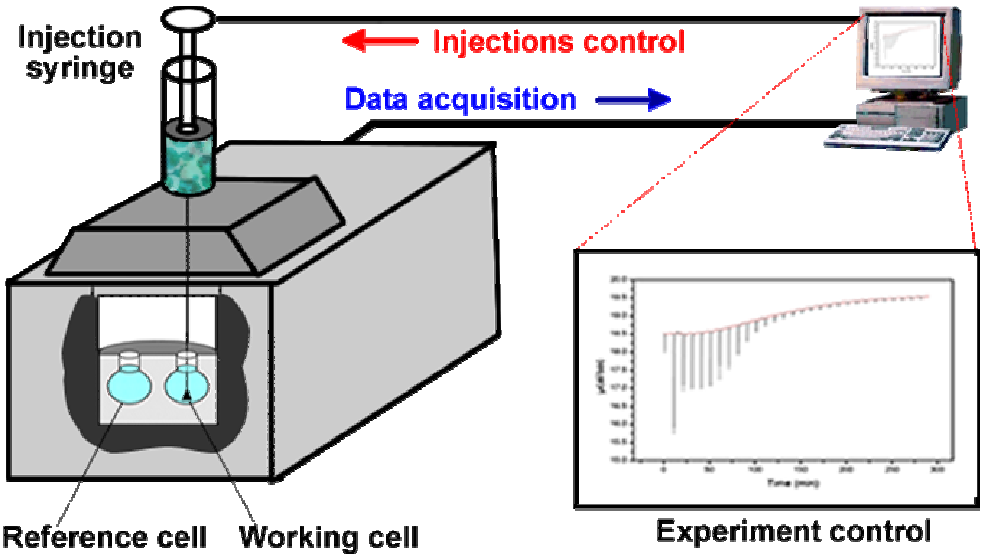

Fig 3.1: A schematic diagram of a titration calorimeter. The cartoon on the left reveals the location of the reference and measuring cells within the machine body. The injection syringe is controlled by a computer driven step motor. Data acquisition is accomplished in real time and the heat flow is displayed on computer screen.

experimentally measured heat per injection. The concentrations of avidin and biotin inside the working cell change after each injection (fig. 3.1):

$$C_{A,i}^{t} = \frac{V_{cell}^{0}}{V_{cell}^{0} + iV_{inj}} C_{A}^{t} = \frac{V_{cell}^{0}}{V_{cell}^{i}} C_{A}^{t}$$
$$C_{B,i}^{t} = \frac{V_{cell}^{0}}{V_{cell}^{0} + iV_{inj}} C_{B}^{t} = \frac{V_{cell}^{0}}{V_{cell}^{i}} C_{B}^{t} \qquad (3.11)$$

The data analysis, based on the chemical equilibrium model (3.5), is particularly simple. After i lipid vesicle injections, the total concentration of complex is $C_{AB,i}$ and the released cumulative heat is

$$H_i = \sum_{k=1}^{i} h_k = C_{AB,i} V_{cell}^{i} \Delta H \qquad (3.12)$$

The unknown $C_{AB,i}$ in (3.12) can be replaced by (3.8a).

$$H_i = \sum_{k=1}^{i} h_k = \frac{1}{2}\left\{\left(\frac{1}{K} + C_{A,i}^{t} + C_{B,i}^{t}\right) - \sqrt{\left(\frac{1}{K} + C_{A,i}^{t} + C_{B,i}^{t}\right)^{2} - 4C_{A,i}^{t} C_{B,i}^{t}}\right\} V_{cell}^{i} \Delta H \qquad (3.13)$$

Because the reaction enthalpy ΔH is known (-88 kJ/mol) the experimentally measured cumulative heat in (3.13) can be fitted by using the equilibrium constant K (3.5), the avidin charge z (defined in 3.1) and the number of occupied binding sites per avidin molecule n

(defined in 3.2) as fitting parameters (n and z enter the equation 3.13 via the current avidin concentration $C^t_{A,i}$).

As an alternative to (3.13) it is possible to fit the individual heat per peak δh_i (released heat per injection) as a function of the increase of lipid concentration in the working cell. Fitting of δh_i values is usually considered to be more reliable than fitting the integrated curve, because integration introduces smoothing of curves. If the biotin concentration in the cell is increased with $\delta C^t_{B,i}$, the concentration of AB will increase with $\delta C_{AB,i}$. That can be expressed mathematically by taking derivative of $C_{AB,i}$ (3.8a)

$$\delta C_{AB,i} = \left\{ \frac{1}{2} + \frac{C^t_{A,i} - \frac{1}{2}\left(\frac{1}{K} + C^t_{A,i} + C^t_{B,i} \right)}{\sqrt{D}} \right\} \delta C^t_{B,i} \tag{3.14}$$

The heat per injection, corresponding to an increase with $\delta C_{AB,i}$ is in the concentration of complexes is

$$\delta h_i = \left(\frac{1}{2} + \frac{C^t_A - \frac{1}{2}\left(\frac{1}{K} + C^t_A + C^t_B \right)}{\sqrt{\left(\frac{1}{K} + C^t_A + C^t_B \right)^2 - 4C^t_A C^t_B}} \right) dC^t_{B,i} V_{cell} \Delta H \tag{3.15}$$

The heat per peak h_i (3.15) is fitted with the same adjustable parameters (K, n and z) used to fit (3.13).The values of the fitting parameter, obtained from (3.15) and (3.13) were compared and were found to be the same within the fit error

3.3. Experimental results

The approach to ITC study of avidin binding to biotinylated vesicles, followed in this work, was to conduct experiments with fixed [95] molar ratio DOPC/biotinyl-PE (DOPC/biotinyl-CAP-PE), while the concentration of avidin was varied. If not mentioned otherwise, the investigated system was 10 mM extruded vesicles with lipid molar ration 10:1, where vesicles are titrated in avidin solutions with different concentrations. If a vesicle made of lipids with this molar ratio (10:1) is completely covered with avidin, some biotins on its surface will remain unbound (fig 3.2) and their number is straightforward to be estimated. In *Appendix C* it is shown that that only about 60% of the total amount of biotin, residing on the outer vesicle surface can be bound by avidin and this amount does not depend on vesicle size.

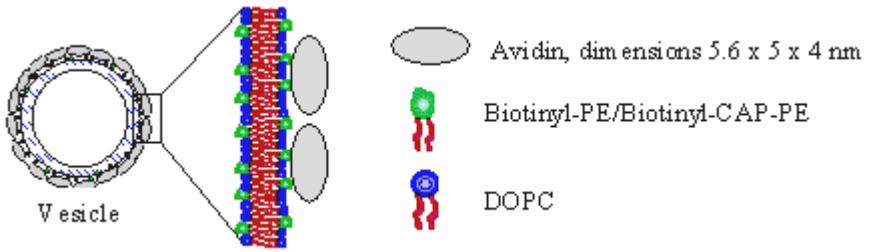

Fig 3.2: Lipid vesicle densely packed with avidin. Due to high surface density of biotin, the area occupied by an avidin molecule will be larger than the one occupied by two neighboring biotins and it is possible that some avidins are connected to wo biotins

The remaining about 40% are located between two neighboring avidins or are covered by the protein (without being bound). The average distance between two biotins on the surface is smaller than the avidin dimensions (5.6 x 5 x 4 nm [46]) and every avidin covers two or more biotinylated lipid heads. Because the membrane is planar one may expect that one avidin binds two biotins.

As mention in the introduction of this chapter, the experimental results can be classified in three categories depending on the biotin/avidin ratio in the system.

3.3.1. Excess of avidin

Chronologically, the first experiments were performed with biotinyl-PE (fig.2.1b) and avidin concentrations 0.05 mM and 0.043 mM. Later it was found that the experiments yield better results (stronger signal and better reproducibility) when the biotinylated lipid is replaced with biotinyl-CAP-PE (fig.2.1c), which has longer linker between the biotin group and the phosphoethanolamine head. Only experiments with 0.043 mM avidin were conducted with the new lipid. The concentration of available for binding biotin in the injection syringe was 0.5 mM and it was injected in 10 μl aliquots in the measuring cell. Due to avidin high concentration it is in excess after each injection – the titrated vesicles bind a tiny protein fraction and the total bulk concentration of avidin does not change significantly. When the next portion vesicles are injected, it is still in excess (in comparison with biotin concentration inside the cell). Presumably when titrated, every vesicle is immediately densely covered with avidin (fig 3.2). Such vesicle is unable to bind more protein and will remain inactive till the end of experiment.

3.3.1.1. Experiments with biotinyl-PE

A representative data of measured heat flow (0.043 mM avidin in the working cell) is shown in fig 3.3a. As expected, the signal indicates exothermic reaction occurring in the cell (release of heat when avidin binds biotin). The area of all peaks is constant (within some

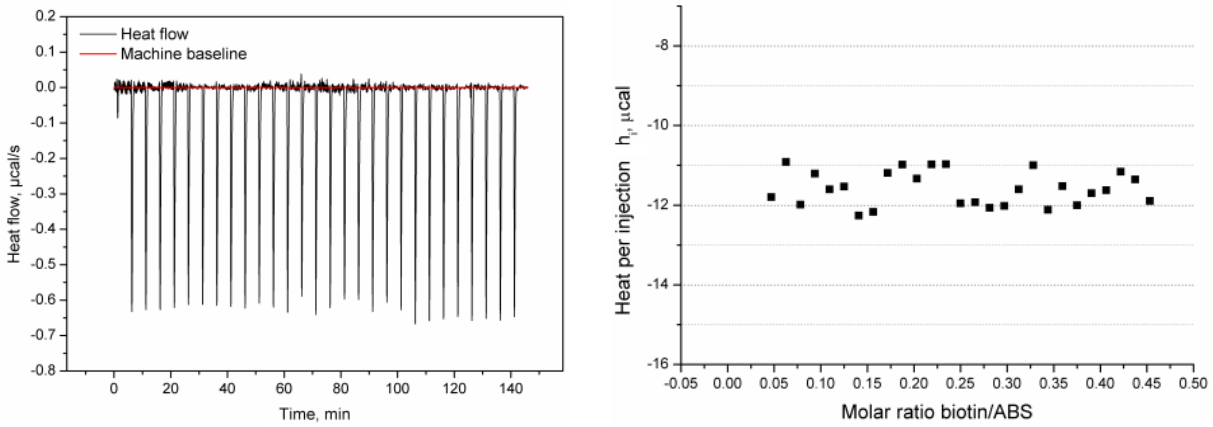

Fig 3.3: (a) Heat flow as function of time for an experiment with biotinyl-PE and 0.043 mM avidin (b) The released heat per injection is calculated from the area of each peak. The latter is determined in respect to the machine baseline. With the increase of molar ratio biotin/ABS in the cell, the amount of released heat does not change (within the machine resolution of about 4 µJ) presumably due to identical processes occurring in the measuring cell. The equilibrium constant K=2.4 mM^{-1} was calculated directly from the experimentally determined heat per injection (see the text for details).

experimental error), which corresponds to a release of identical amounts of heat. The latter is an indication for identical processes occurring inside the measuring cell after every injection of the same amount vesicles. Quantitative data about the latter was obtained from the heat flow signal of the corresponding injection and the baseline (fig 3.3b). Because the processes occurring after every vesicle injection were identical, the chemical equilibrium model was not used. In order to obtain the fitting parameters of the model one has to compare the heat response from several different system compositions (e.g. several molar ratios biotin/ABS inside the working cell). The equilibrium constant K was determined directly from the heat per injection data (by using equation 3.15). It was assumed that the process of binding of avidin to a biotinylated membrane is identical in the cases of biotinyl-PE and biotinyl-CAP-PE (see the text further). The chemical equilibrium model was used to fit the data from the experiments with biotinyl-CAP-PE. The obtained data (presented in Table 1) for the number n of occupied ABS per avidin molecule and the avidin charge z were averaged (n=2.4, z=1.02) and plugged in equation 3.15 (n and z are hidden parameters and participate in 3.15 via the total concentration C_A^t of avidin in the cell). The obtained value for the equilibrium constant were K=0.4 mM^{-1} (averaged over two experiments) for 0.043 mM avidin and K=0.5 mM^{-1} (averaged over two experiments) for 0.05 mM avidin.

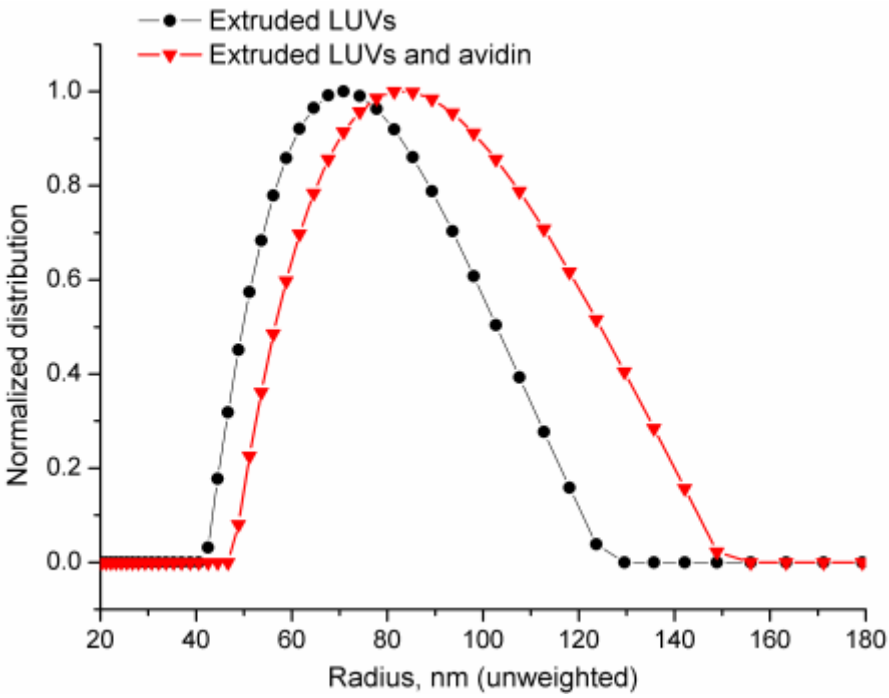

Fig 3.4: Size distribution of extruded LUV and LUV-avidin (0.043 mM avidin) complex (taken out of ITC measuring cell) as determined by dynamic light scattering. The distribution of the complex is shifted towards bigger radii and it is broader. Because avidin is not detectable, probably the increase in size is due to formation of small aggregates (e.g. two vesicles linked together by a single avidin).

As noted before (section 2.2.1.1) prior to every experiment the vesicle size distribution was determined with a Dynamic Light Scattering (DLS) measurement. When all injections were completed the content of the measuring cell (vesicles coated with avidin) was taken out and the size distribution was measured again. Due to avidin small dimensions, the intensity of scattered light from avidin solutions only is very low, much lower (50-100 times [89]) than the one detected from vesicle solutions. When the size distribution of the vesicle-avidin solutions is investigated, the contribution of bulk avidin appears only as a background and can be ignored. Therefore such measurement yields only vesicle size distribution. Such size distribution of the complex (0.043 mM avidin) is shown in fig 3.4. It is broader and the average size is bigger than the corresponding one of GUV. Probably, the increase is due to formation of aggregates, e.g. two vesicles bound by a single avidin molecule. Because the increase is relatively small, the aggregates should be small as well. Another possible reason for this increase is some vesicle shape transformations, induced by anchored avidin, which alter vesicles hydrodynamic radius. Evidences supporting aggregation hypothesis will be presented in the next sections.

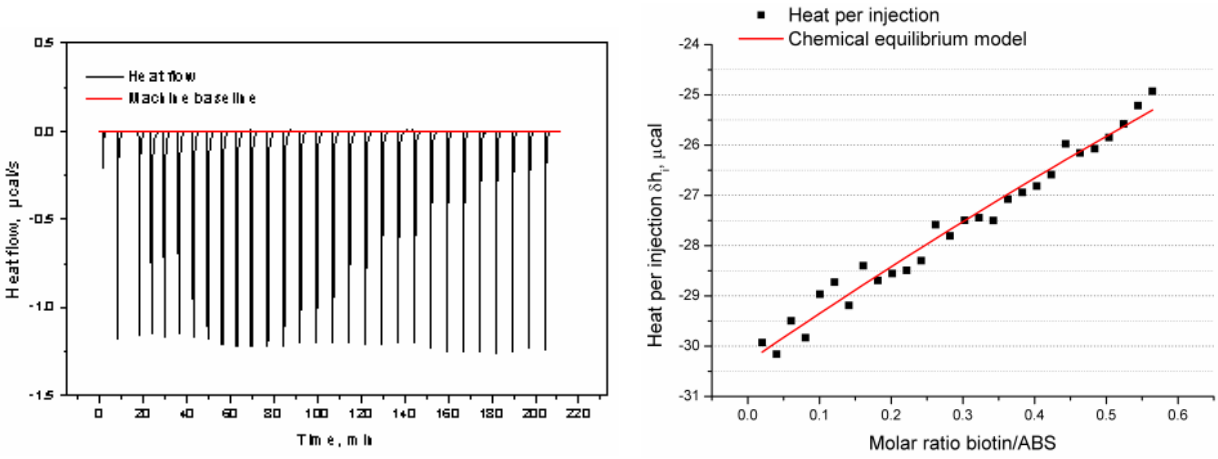

(a) **(b)**

Fig 3.5: (a) Heat flow as a function of time for an experiment with 0.043 mM avidin. The released heat is calculated from the area of each peak. The latter is determined in respect to the machine baseline. Notice the stronger signal in the experiment with biotinyl-CAP-PE; (b) the heat per injection decreases with the increase the amount of biotin in the cell. The fitting parameters were obtained by fitting the experimental data with the theoretical model. The obtained values of fitting parameters of the latter were K=2.7 mM^{-1}, n=2.3, z=0.9.

3.3.1.2. Experiments with biotinyl-CAP-PE

A representative data of measured heat flow (0.043 mM avidin) is shown in fig 3.5a. As in the previous case (with biotinyl-PE) the signal indicates an exothermic reaction occurring in the measuring cell. The depth of every peak seems to be same (within some experimental error), which should corresponds to release of identical amounts of heat. Notice the stronger signal than the heat flow, measured in the experiment with biotinyl-PE (fig. 3.3a). The corresponding heat per injection is shown in fig. 3.5b. Unlike the constant signal, detected in the experiment with biotinyl-PE (fig. 3.3b) a well pronounced trend is observed – with the increase of the molar ration biotin/ABS inside the ITC measuring cell, the amount of released heat decreases. Although the depth of every peak is the same, the area seems to be different, decreasing with the increase of the molar ratio biotin/ABS. Presumably the latter occurs due to exhaustion of the free for binding protein inside the bulk. Obviously this result contradicts with the one obtained with biotinyl-PE, where such decrease in trend was not observed.

A comparison of experimentally determined heat per injection and the corresponding heat predicted by the chemical equilibrium model is presented in fig 3.5b. The obtained values of fitting parameters were K=2.7 mM^{-1}, n=2.3, z=0.9. Further in the text the obtained data is to be compared with the one, obtained from the experiments with biotinyl-PE.

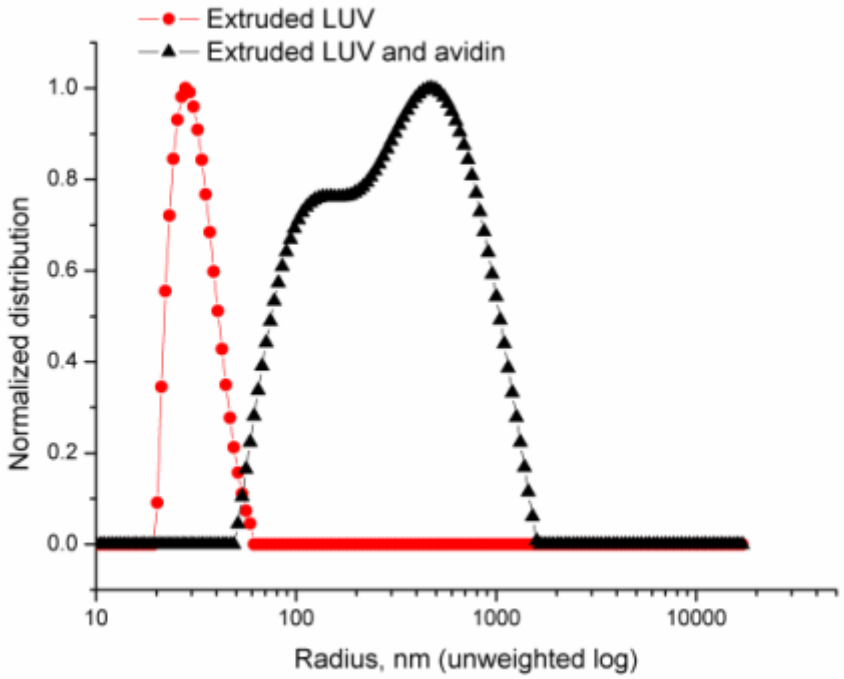

Fig 3.6: Size distribution of extruded LUV and LUV-avidin (biotinyl-CAP-PE, 0.043 mM avidin) solution (taken out of ITC measuring cell). The distribution of the complex is shifted towards bigger radii and it is much broader. Since avidin is not detectable, probably the increase in size is due to formation of aggregates (e.g. several two vesicles linked avidin molecules).

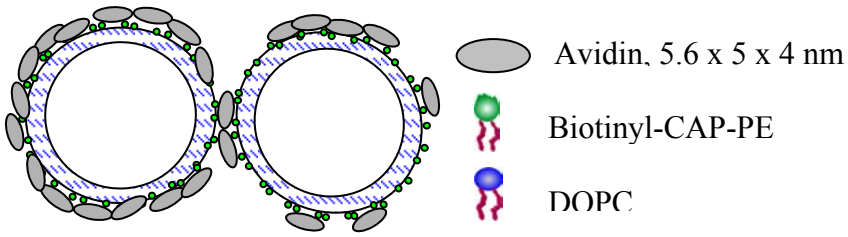

Fig 3.7: Mechanism of biotinylated vesicle aggregation, mediate by avidin. Each protein can bind up to four biotins and can serve as a linker between two different vesicles. A small aggregate of two vesicles can bind new ones, thus increasing its size.

As in the case with biotinyl-PE vesicle size distribution was determined with DLS prior the experiment and after all injections were completed. The LUVs -avidin solution taken out of the ITC measuring cell was very turbid. The intensity of scattered light was low and the resulting size distribution is shown in fig 3.7. The average size is shifted to much bigger values and the distribution function is remarkably broader. The relevant hypotheses to explain such a big shift is aggregation of vesicles mediated by avidin. Every avidin has four ABS and because avidin is a globular protein due to high membrane surface density of biotin a single

avidin can bind two different vesicles. Such avidin bridge is actually a very strong bond (about 75 k_BT) if each protein binds two biotins – one from one vesicle, and other from another. During the initial injections each vesicle binds free avidin from the bulk. Therefore the concentration of free avidin decreases and only ABS from already bound avidin are available for further binding. Those ABS bind the vesicles introduced in the measuring cell by the next injections. This mechanism (sketched in fig 3.7) may generate big aggregates of avidin bridged vesicles. One may expect that the bigger the molar ratio biotin/ABS is the bigger the aggregates will be. Probably there is a "critical" point of this molar ratio, where the aggregation process actually starts. This point is to be answered in the next sections.

As expected (because of the lower signal, fig 3.3a), the equilibrium constant for ABS-biotinyl-PE reaction is lower than for the ABS-biotinyl-CAP-PE one. Presumably avidin cannot easily access biotin groups on the surface of biotinyl-PE containing membranes, because the biotins are very close to (or partially buried in) the vesicle membrane. The values of the other two fitting parameters for both lipids are very close, probably due to identical binding mechanisms – each avidin binds at least two biotins ($n>2$) and due to its charge ($z\approx1$) experiences attractive interaction with the membrane. As discussed before, the latter increases protein concentration in the vicinity of the membrane, increasing the probability for realizing an ABS-biotin bond. Due to the better performance (higher signal) of the experiment with biotinyl-CAP-PE all of the following experiments were conducted with this lipid only.

3.3.2. Intermediate ratios (close to 1:1)

These experiments were conducted with biotinyl-CAP-PE (fig.2.1c) and avidin concentrations 0.01 mM and 0.02 mM. The concentration of available for binding biotin (see equation 3.3) in the injection syringe was 0.5 mM and with every injection 10 μl vesicles were introduced in the measuring cell. Initially, due to the large number of formed ABS-biotin bonds, the released heat flow was very intensive, resulting in a strong signal. With further addition of biotin in the cell, the amount of available for binding bulk avidin decreases, resulting in a decrease of the injection signal. A typical time evolution of heat flow data is presented in fig 3.8a. As in the previous case with excess of avidin, the initial injections produced a strong signal and peak heights are comparable – presumably due to identical processes in the cell. When the bulk protein concentration is exhausted, resulting in fewer ABS-biotin bonds with further injections. Note that the signal is significantly lower than the corresponding one, shown in fig 3.5b, measured with the system 0.043 mM avidin

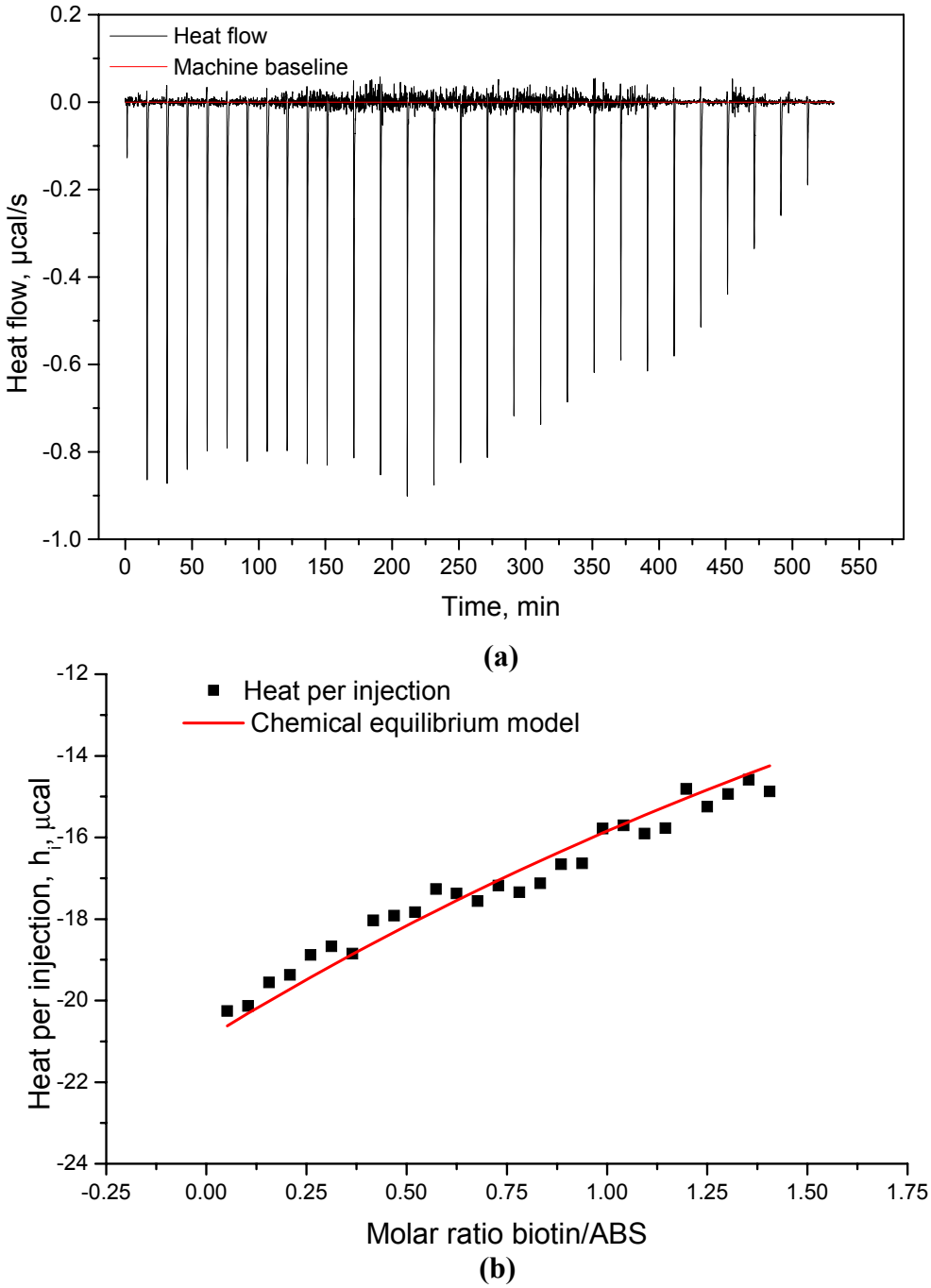

Fig 3.8: (a) Heat flow, measured as a function of time for an experiment with 0.01 mM avidin. For the first injections, bulk avidin is in excess and due to identical processes occurring in the cell after each injection, the heat peaks are identical. When a fraction of avidin is already bounded, the bulk concentration is significantly reduced, resulting in lowering down the released heat; (b) Fitting experimentally determined heat peaks per injection and the predictions of the chemical equilibrium model. With the increase the molar ratio avidin/ABS in the measuring cell, the amount of released heat decreases.

and vesicles containing biotinyl-CAP-PE (as in this case). Quantitative data about the equilibrium constant K is obtained by fitting the experimentally measured heat per injection h_i with the chemical equilibrium model ((3.5) and (3.15)). The fitting parameters again were the number occupied binding sites per avidin n, avidin charge z and the equilibrium constant K.

The theoretical model is compared with experimental (0.01 mM avidin) data in fig 3.7b. The obtained values of fitting parameters were K=4.3 mM^{-1}, n=2.5, z=1.2 (averaged over three experiments). The same procedure was followed to obtain the value of fitting parameters for the experiments with 0.02 mM avidin and they were found to be: K=2.1 mM^{-1}, n=2.5, z=1.1 (averaged over three experiments).

Again, after the completion of the ITC measurement the LUV-avidin mixture was taken out of the measuring cell. In some samples there were small (but visible with naked eye) aggregates. As in the case with excess of avidin, the sample was very turbid and DLS measurements showed similar shift to the one presented in fig 3.6. The distribution function was much broader and the average size was shifted to much higher values (about 100 times). Presumably aggregate formation follows the same mechanism sketched in fig 3.7.

3.3.3 Excess of biotin

The biotinylated lipid, used for this study was again biotinyl-CAP-PE (fig.2.1c). As in the other cases (excess of avidin and intermediate ratios) vesicles were titrated in avidin but of lower concentrations: 0.0025 mM and 0.005 mM. The concentration of available for binding biotin inside the injection syringe was 0.5 mM and it was injected in identical amounts of 10 μl. If the equilibrium constant K for avidin binding to biotinylated membranes is as high and for free avidin – free biotin reaction (the highest measured value is K=10^{12} mM^{-1} [88, 44, 107]), the avidin should be exhausted after the first injection. Thus, the very strong initial signal was expected to drop down, because all ABS in the bulk had to be occupied. No more bonds were to be formed and the only measurable heat was expected to come from dilution of the cell content with all further injections.

The expected behavior, typical for a very large equilibrium constant K, was not confirmed experimentally. A representative raw (the baseline has not been subtracted) heat flow data for avidin concentration 0.005 mM is shown in fig 3.8. Indeed, dropping down of the signal was observed, but it is remarkably slower than expected. At the moment of the 16^{th} injection where all avidin must have been bound, the heat flow inexplicably (but experimentally reproducibly) changes its behavior - a jump towards reaction with much smaller heat effect was observed (fig 3.9). The following injections resulted in a very low signal of the heat flow, comparable with dilution of the cell content (determined in separate of control experiments).

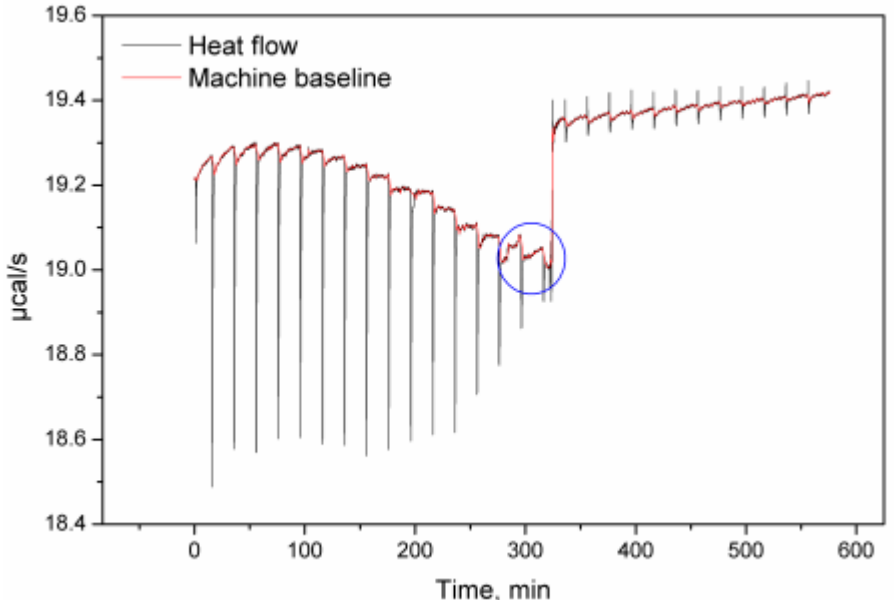

Fig 3.9: Raw data of the heat flow, measured as function of time. The signal is dropping down due to exhaust of bulk avidin (0.005 mM). The blue circle denotes the point of precipitation (discussed further in the text).

Attempts to measure size distribution of LUV-avidin mixture from the experimental chamber were made. When the mixture was taken out, large visible with naked eye aggregates were present inside. Their size distribution couldn't be determined with DLS, because they were too big and thus reflecting too much light. A possible mechanism of vesicles aggregation in excess of biotin is sketched in fig 3.10.

So far aggregation was observed in the cases with excess of biotin. Since the number of occupied ABS per avidin is used as a fitting parameter it is essential to know at what molar

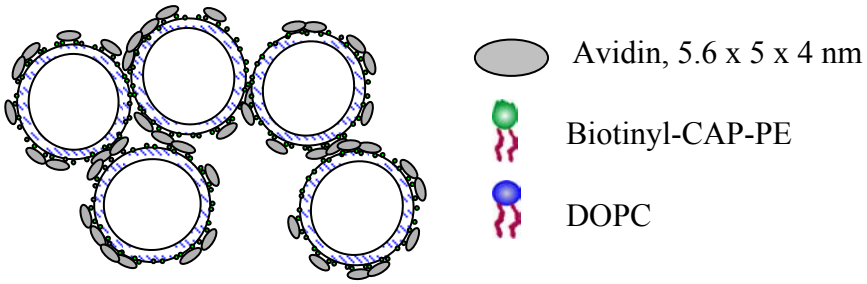

Fig 3.10: Mechanism of assembly of large vesicle aggregates. Due to large excess of biotin, the bulk concentration of avidin binding sites (ABS) is exhausted. Every avidin can bind up to four biotins and thus it can serve as a linker between two different vesicles. With every further titration, the number of vesicles in the measuring cell will increase. Due to lack of free bulk avidin the new vesicles will bind the protein, which already has been bounded by other vesicles, thus assembling larger structures (aggregates). At a certain number of bounded vesicles the aggregate becomes very large and sediments.

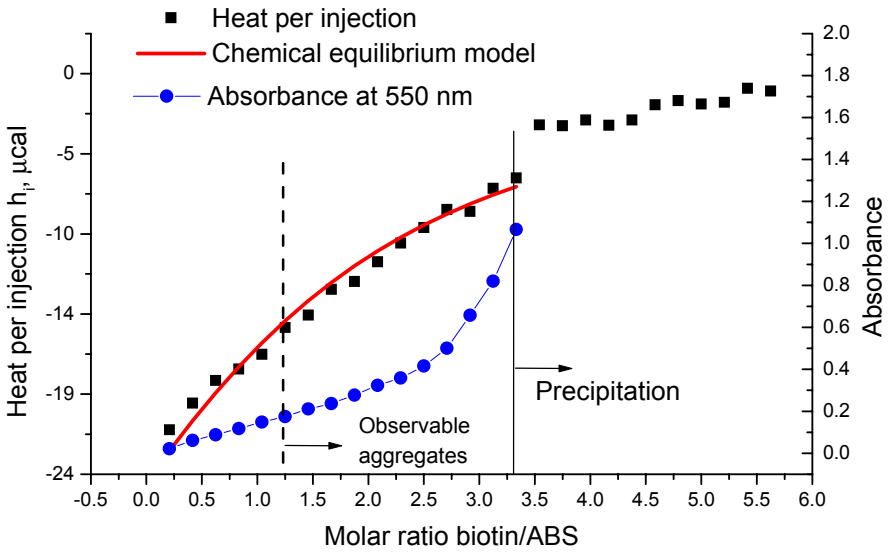

Fig. 3.11: Integrated heat peaks for LUVs injected in 0.005 mM avidin and absorption spectrum at 550 nm. Due to precipitation, only the first 16 injections were taken into account when fitting the data with the chemical equilibrium model (equation 3.5). With increasing molar ratio biotin/ABS (increasing amount of titrated biotin) in the cell, the absorbance increases due to specimen aggregation.

ratio biotin/ABS the aggregates appear. Absorbance measurements, simulating an ITC experiment were conducted as follows:

1. Absorbance from avidin (0.005 mM and 0.0025 mM) and from vesicle solution was measured separately.
2. Avidin solution (the same volume and concentration as in the ITC measuring cell) was continuously stirred via a magnetic stirrer. Vesicles (10 µl) were manually titrated via a pipette with this solution.
3. Absorbance from avidin-vesicles solution was measured after each titration
4. Vesicles absorption was subtracted from the resulting data.

Absorbance and integrated heat peaks data is presented in fig 3.11 (0.005 mM avidin). Unlike closed ITC measuring cell, the transparent UV-absorption cuvette allows visual contact with the specimen. Small (but visible with a naked eye) aggregates were observed when the 6th portion vesicles was titrated (molar ratio biotin/ABS=0.62). A human eye can resolve only objects bigger than 0.5 mm and the size of a single LUV was about 50-100 nm, the aggregates formed up to the 5th injection were already huge, containing hundreds of vesicles. Therefore one may expect that almost all ABS will be occupied. There are two distinct regimes of linear increases in absorption, as is indicated in fig 3.11. The first of them (up to biotin/ABS=2.5) is probably due to aggregation of vesicles. The second one (above biotin/ABS=2.5) could be referred as “aggregation of aggregates”. When biotin/ABS>3.3, the aggregates sediment.

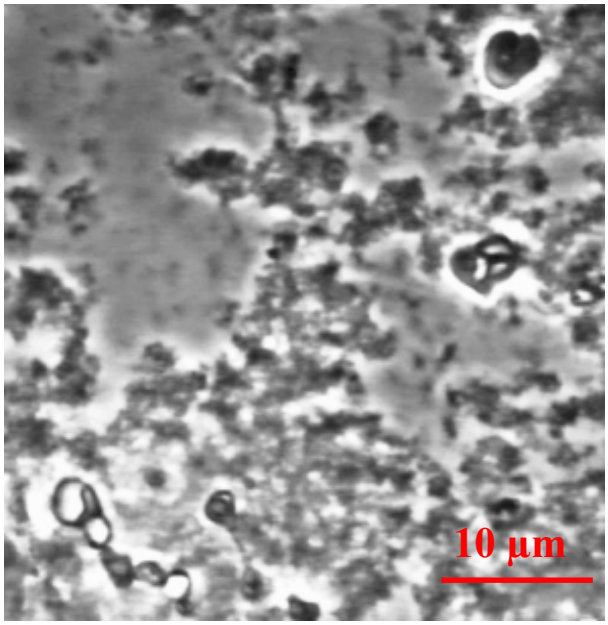

Fig 3.12: Aggregates formed of vesicles via avidin bridges. The sample was observed in transmitted light with 100x phase contrast objective

Sedimentation could be the reason for drastic change in the heat flow signal, shown in fig 3.9. Aggregates were examined with optical microscope equipped with 100x immersion phase contrast objective. Single LUV cannot be observed, because their dimensions (50-100 nm) are far below the resolution of the optical microscope (about 0.2 µm). The aggregates, however, are with micron sizes (much bigger than a single LUV) and have complicated branched structure (fig. 3.12).

Quantitative data about the equilibrium constant K was obtained by fitting the experimentally measured heat per injection h_i with the chemical equilibrium model ((3.5) and (3.15)). The fitting parameters again were the number of occupied binding sites per avidin n, avidin charge z and the equilibrium constant K. Only data preceding the precipitation (first 16 injections) were taken into account. The obtained values of the fitting parameters were K=9.5 mM^{-1}, n=2.5, z=0.7 (averaged over three experiments).). The same procedure was followed to obtain the values of fitting parameters for the experiment with 0.0025 mM avidin and they were found to be: K=8 mM^{-1}, n=2.2, z=1.2.

3.3.4. Streptavidin coated nanospheres

Streptavidin coated polysterene nanospheres were considered as an alternative method to link biotinylated membranes and DNA. The spheres we used were densely covered with streptavidin and their average diameter was 70 nm. Unlike avidin, streptavidin does not have uncompensated charges at pH 7 (pH of the working buffer). While an avidin can bind up to

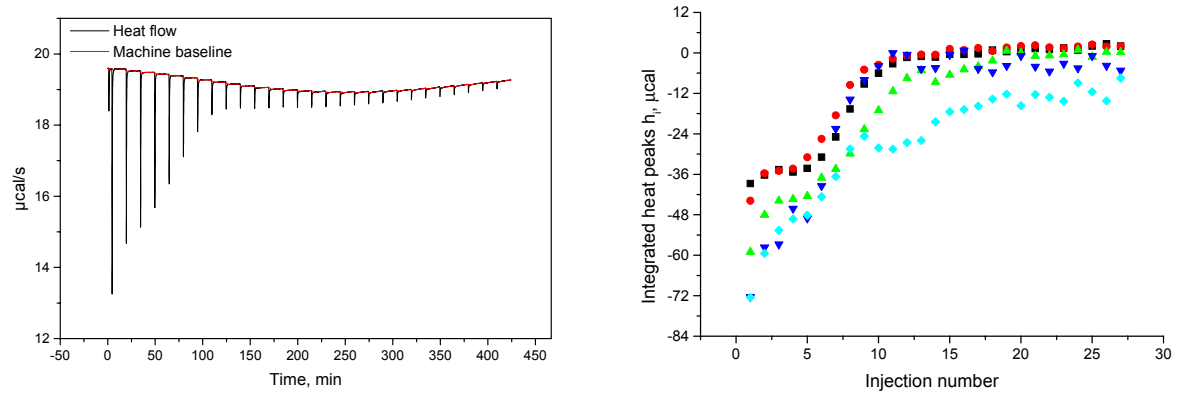

Fig 3.13: (a) Raw data heat flow (base lane is note subtracted) per injection, measured as function of time. The signal is leveling down due to exhaust of bulk avidin concentration of streptavidin (microspheres). Microspheres concentration is 10^{-6} mM. Notice the heat flow high intensity and well defined base line; (b) Integrated heat peaks for the injections of 10 mM DOPC/biotinyl-PE (1:1) vesicle (average diameter 200 nm) in 10^{-6} mM nanosphere solution. Integrated heat peaks are plotted versus injection number, since in this experiment, the exact molar ratio of available for binding avidin and streptavidin is not known

four biotins, each microsphere has about 2000 available (see [102]) ABS (measured with fluorescently labeled biotin [90]). The experiments of binding avidin to biotinylated membranes of 10 mM LUVs with molar ratio DOPC/bionylated lipid 10:1 in general produced relatively low signal. The latter was reflected in badly defined baseline (relatively low signal/noise ratio). In order to detect stronger signal, the amount of biotinylated lipid was increased to 50% of the total amount of lipid.

All experiments were conducted with 10 mM extruded vesicles, DOPC/Biotinyl-CAP-PE 1:1. Because the nanospheres diameter is relatively large, vesicles bigger than in all previous experiments were used - average diameter of about 200 nm. Two different bulk concentrations of nanospheres were used – $5x10^{-7}$ mM and 10^{-6} mM. The same experimental procedure, as described before, was followed – vesicles were titrated in nanospheres solution.

A typical heat flow data is shown in fig 3.13a. The first seven injections result in a strong signal. Notice the signal intensity rises up to 6 µcal/s – much higher than any experiment with avidin (fig 3.3a, 3.5a, fig 3.8a and fig 3.9). When the first 6-7 injections were completed, heat flow drops down to a value, comparable with dilution heat of injection of vesicles in buffer (or buffer in nanospheres). This fast signal decrease indicates that the whole amount of ABS on nanospheres was exhausted and no streptavidin ABS were available for further binding. The next injections introduce new vesicles, increasing biotin excess in the measuring cell. Although available for binding biotin was in excess, visible aggregates and precipitation was not observed. The latter is not an indication for absence of aggregates. The

nanospheres we used were colored in blue and their stock solution (and all dilute solutions) was quite turbid. The high turbidity may have hindered the observation of visible aggregates.

Several integrated peak curves (form different experiments) are shown in fig 3.13b. The experiments were not reproducible. The chemical equilibrium model was not used to fit the experimental data. One possible reason for the lack of reproducibility is that streptavidin is not free in the bulk, but fixed on the nanospheres surface, which introduces steric constraints on the streptavidin-biotin interactions.

Nanospheres were abandoned as a possible linker between a biotininylated membrane and DNA, due to the following reasons: *i)* the concentration of ABS cannot be controlled precisely – an error with one microsphere introduces about 2000 more/less ABS. Probably this is the main reason for the irreproducible experiments; *(ii)* Due to the irreproducibility of all ITC experiments of binding on vesicles with surface biotin anchors, no quantitative analysis of the data was possible; *iii)* In the presence of nanospheres GUV suitable for the fluctuation analysis experiments (see section 2.2.3) could not be prepared (due to the large number of defects).

3.4. Discussion and conclusions

The purpose of this ITC study was to answer the important question of how many avidins will bind on a vesicle with a given surface density of biotin at given experimental conditions. Series of experiments were conducted where avidin solutions of different concentrations were titrated with extruded LUVs. Vesicles with total lipid concentration 10 mM were made of DOPC/biotinyl-CAP-PE (biotinyl-PE), with molar ratios 10:1 and 1:1. Depending on the concentration of biotin relative to the concentration of avidin in the ITC-machine working cell, three regimes were investigated: *i)* Excess of avidin (protein concentrations 0.05 mM and 0.043 mM); *ii)* Intermediate case (avidin concentrations 0.02 mM and 0.01 mM); *iii)* Excess of biotin (0.005 mM and 0.0025 mM avidin). It was assumed that the ABS-biotin binding reaction can be described in terms of a chemical equilibrium model with three fitting parameters. The quantities, used as adjustable parameters were the equilibrium constant K, the number n of occupied ABS per avidin molecule and the avidin charge z.

As noted in [107] the literature data about the equilibrium constant of the avidin-biotin bond has not been systematically collected and many biotin derivatives, including the d-biotin, used in this work, have not been systematically studied (see Table V in reference [44]

Avidin concentration mM	*Equilibrium constant K, mM^{-1}*	*Number of occupied ABS/molecule*	*Avidin charge*
0.0025	8	2.2	1.2
0.005	9.5	2.5	0.7
0.01	4.3	2.5	1.2
0.02	2.1	2.5	1.1
0.043*	0.4	2.4**	1.02**
0.043	2.7	2.3	0.9
0.05*	0.5	2.4**	1.02**

Table 1: Fitting parameters of the chemical equilibrium model.
* Experiments conducted with biotinyl-PE
** Averaged over the experiments performed with biotinyl-PE

for a list with the available data). This makes relatively difficult to compare our results with the literature data, because depending on the experimental conditions the equilibrium constant for the different biotin derivatives, varies in a wide range (see [107]). Probably the closely related to d-biotin derivatives, studied at pH 6.8 are 1'-N-Methoxycarbonylbioyin and 3'-N-Methoxycarbonylbioyin methyl ester and the reported equilibrium constants were $2.5.10^3$ mM and 10^6 mM respectively (reference [44]). The obtained data from our ITC-study is presented in Table 1. Obviously equilibrium constant for our system is smaller than the reported ones. That difference may originate from the chemical difference between d-biotin and the other two biotin derivatives. Moreover the literature data is obtained for the case of chemical equilibrium between free avidin and free biotin molecules. Presumably the difference is due to geometrical constraints imposed by the vesicle surface - in our case biotin is not free in the bulk but is chemically linked to PE-lipid heads, incorporated in the membrane. When a vesicle is made of biotinyl-CAP-PE, the biotin group is about 1.5 nm above the membrane; in the case of biotinyl-PE containing vesicles, biotin lies on its surface. An additional complication arises from membrane fluctuations – they may hinder ABS-biotin binding. Thus, presumably the biotinylated membranes bind much fewer avidins than the same amount of free bulk biotin would bind.

When attached to the two dimensional membrane surface, the biotin groups loose entropy. Thus, by taking into account equation (2.1) (and assuming that the change in the enthalpy does not change if the biotin is attached to the membrane), one may expect a decrease in the Gibbs free energy ΔG. The latter is related to the equilibrium constant K as

$$K = \exp\left(-\frac{\Delta G}{k_B T}\right) \tag{3.16}$$

Because of the exponent in (3.16) even small changes in ΔG (e.g. due to loose of entropy) implies large changes in K (e.g. large decrease due to the loose of entropy).

There is a significant discrepancy between the equilibrium constant, determined for the cases with different molar ratio biotin/avidin. Actually the difference between biotinyl-PE and biotinyl-CAP-PE membranes was to be expected. Due to the shorter link between the biotin group and the PE-lipid head the biotin is much closer to (or partially buried in) the membrane and therefore is less accessible for the avidin. In this case one may expect fewer ABS-biotin bonds and correspondingly – smaller equilibrium constant. There are three possible reasons to explain the difference between experiments conducted with biotinyl-CAP-PE and different protein concentrations

1. Both concentrations – avidin and biotin – are very low. When the equilibrium constant is low as well, the ratio signal/noise is low too. As a consequence, the machine baseline is not well defined, introducing errors in the heat per injection values (determined from experimentally measured heat flow in respect to the baseline)

2. When bound to the membrane, avidin can bind up to two biotins from vesicle surface. Due to the spatial orientation of ABS, this probably is not possible without some mechanical stretching or torsion of the avidin. That could lead to protein denaturation, whose heat effect cannot be separated from the heat released due to binding.

3. In the case of excess of biotin, aggregation of vesicles was detected. Such big (visible with a naked eye) aggregates may have their own heat contribution (e.g. from dynamical assembly and disassembly) which cannot be separated from the heat of binding.

In the chemical equilibrium model two fitting parameters - the number of occupied ABS per molecule n and avidin charge z - appear in the product $\sim n\exp\{-zF\psi/RT\}$, which in fact is minimized by the fitting procedure. The global minimum of the fitting function however could be the same for several pairs of parameter value. Therefore the value for n and z may not be precise, but that does not have any impact on the value of K. For each protein concentration the chemical equilibrium model yields almost identical value (n=2.3-2.5) for the number of occupied ABS per molecule. Presumably either one avidin binds two biotins from the same vesicle or two biotins from two different vesicles (probable mechanism of vesicles aggregation). As was already mentioned, in order to bind two neighboring biotins (from the same vesicle), the avidin molecule or the membrane should deform and that may not be energetically favorable. The energy of thermal denaturation of streptavidin for example (which is very similar to avidin) if on the same order as the energy of the ABS-biotin bond.

Chapter 4

Change in membrane elastic properties due to polymer anchoring in mushroom regime: analyses of membrane fluctuations

4.1. Overview and motivation

The goal of this work is to test experimentally the theoretical predictions for the change in the material properties (bending rigidity, κ and spontaneous curvature, M_{sp}) of lipid vesicles induced by anchored polymers. In section 2.2.2 we described the membrane behavior depending on the surface concentration of polymers. In both surface concentration regimes (mushroom and brush) an increase in κ and M_{sp} is expected. The following discussion summarizes the theoretical understanding of the curvature and bending rigidity effects arising from anchored molecules [10, 22 27, 29]. Vesicles with anchored polymers have also been studied experimentally [93] by using optical microscopy. The authors demonstrated that vesicles undergo morphological transformations as a consequence of the anchored polymers. These experimental studies however were not systematic and the obtained results were only qualitative - neither the amount of anchored polymers was controlled nor investigation of the changes in κ and M_{sp} were conducted. This lack of systematic experimental studies reflects the difficulty to measure the absolute values of membrane material elastic properties (κ and M_{sp}). These properties can be quantified by analyzing the membrane thermal fluctuations [11, 79]. One version of the latter method is the fluctuation spectroscopy of prolate vesicles (see section 2.3). By employing this technique one can analyze the membrane fluctuations in real time and obtain information about both parameters (κ and M_{sp}) simultaneously from one experiment on a single vesicle.

We attempt to quantify the changes in membrane spontaneous curvature and bending rigidity, induced by long (48502 bp) double stranded λ-DNA with different surface concentrations. The surface concentration of grafted polymers is always lower than the

overlap coverage Γ^{ov} (see section 1.2.2), for λ-DNA Γ^{ov}= 0.75μm^{-2} [91]), thus the DNA coverage is always in mushroom regime. The working surface concentrations which were studied are given in terms of the overlap concentration Γ^{ov} and were equal to $0.03\Gamma^{ov}$, $0.06\Gamma^{ov}$, $0.12\Gamma^{ov}$, $0.3\Gamma^{ov}$ and $0.6\Gamma^{ov}$. Anchoring was achieved by making use of the very strong non-covalent avidin-biotin bond between avidin covered vesicles and biotinylated DNA. Giant unilamellar vesicles (GUVs) made of DOPC and biotinyl-CAP-PE were prepared by swelling in the presence of avidin (see section 2.2.1.1). The amount of avidin used in the process of swelling was in excess relative to the total amount of biotin. In the previous chapter, depending on the molar ratios of avidin and biotin, three different regimes were investigated: excess of avidin, intermediate case and large excess of biotin. The averaged on all regimes (only the cases with biotinyl-CAP-PE, used in GUVs) equilibrium constant was found to be K=5.3 mM^{-1}. Because of the large excess of avidin we expect that all biotin groups residing on the vesicle surface are bound. Unlike the case with extruded vesicles used in the ITC study, the average distance between neighboring biotins on the surface is large (ranging between 0.8μm and 2.6μm) and a single avidin molecule probably cannot bind two biotins. The amount of biotin on the surface was controlled by varying the molar ratio biotinyl-CAP-PE/DOPC (ranging between 10^{-5} and 10^{-4} molar percents for the different surface concentrations). As explained in section 2.1.3 the "sticky" end of the DNA molecule was ligated with a nucleotide with biotinylated end. The latter makes it possible to anchor the DNA molecule to avidin covered membranes. Due to the very low concentration (about 10^{-13} M) of DNA it was impossible to determine the amount of anchored molecules with an ITC measurement, because the released heat would be below the machine resolution. Instead we attempted to estimate the number of anchored DNA by series of confocal microscopy measurements, conducted with vesicles with different surface concentration of anchors, and fluorescently labeled DNA (see section 2.2.3)

4.2. Sample preparation. Flow chamber

For the purpose of this study only GUVs were used. They were prepared by spontaneous swelling as described in Chapter 2 (section 2.2.1.1). The vessel with swollen vesicles sample (stored in the oven at 37^{o}C before use, see section 2.2.1.1) was opened prior to each experiment. A small amount of sucrose solution from the sample (about 150 μl) was taken out and the osmolarity of the solution was measured. The typical osmolarities were ranging between 150 and 200 mOsm/g. A glucose solution (in the same buffer as the sucrose

one) with slightly higher (about 5-7 mOsm/g) osmolarity was prepared. The characteristic vesicle cloud was gently taken out of the bottle with a pipette and was diluted in the glucose solution. The latter achieves three effects: *(i)* deflation of the vesicles (more free excess area, necessary for the fluctuation spectroscopy experiments); *(ii)* enhancing the contrast due to refractive indexes difference inside/outside the vesicle; *(iii)* due to the higher density of sucrose (than glucose), the vesicles sediment on the bottom of the vessel.

A Teflon microchamber was fixed with silicon grease to a hollow metal holder and then was sealed with a microscope cover glass, fixed again with silicon grease (fig 4.1a). The hollow metal holder was connected to a continuously running thermostat, set to 25^{o}C. Thus the chamber was tightly sealed and temperature regulated. The enclosed volume (about 500 μl) was connected to external vessel via two pipes tightly screwed to the chamber. One of these two pipes was dipped in the vessel with the sample and the other was connected to a computer controlled micropump. The pump applies sucking pressure and introduces a controllable amount of the sample inside the chamber with flow rate of about 400 μl/min.

Initially the microchamber was filled with albumin solution (1 mg/ml). The protein was let to adsorb on the chamber walls for 15 min. The excess (not adsorbed) albumin was removed by flushing 4 ml buffer (the same buffer where the vesicle cloud was dissolved). Thus the cover glass was coated with albumin, preventing the adhesion of vesicles to the glass. After removing the excess protein, the vesicle solution was introduced in the chamber. In order to avoid temperature induced effects, the whole experimental setup was let to equilibrate for 1 hour before the experiment was started.

4.3. Experimental procedure

To study the membrane fluctuations of GUVs we used phase contrast video microscopy combined with a computer controlled system for image acquisition and processing (fig 4.1b). When introduced in the microchamber due to the excess of free area, at 25^{o}C (room temperature) all non-spherical vesicles undergo detectable thermal fluctuations. A fluctuating prolate vesicle can be “fixed” in the focal plane of the microscope if the density of the solvent inside is higher than the density of the solvent outside. Sometimes this “trick” is called gravitational stabilization. In our experiments the content of vesicle volume was sucrose solution and outside was glucose. The vesicle is heavier than the solvent and lies on the bottom of the experimental chamber, a microscope cover glass, where the microscope can be focused. This stabilization seems to be sufficient to keep the long axis of a prolate vesicle

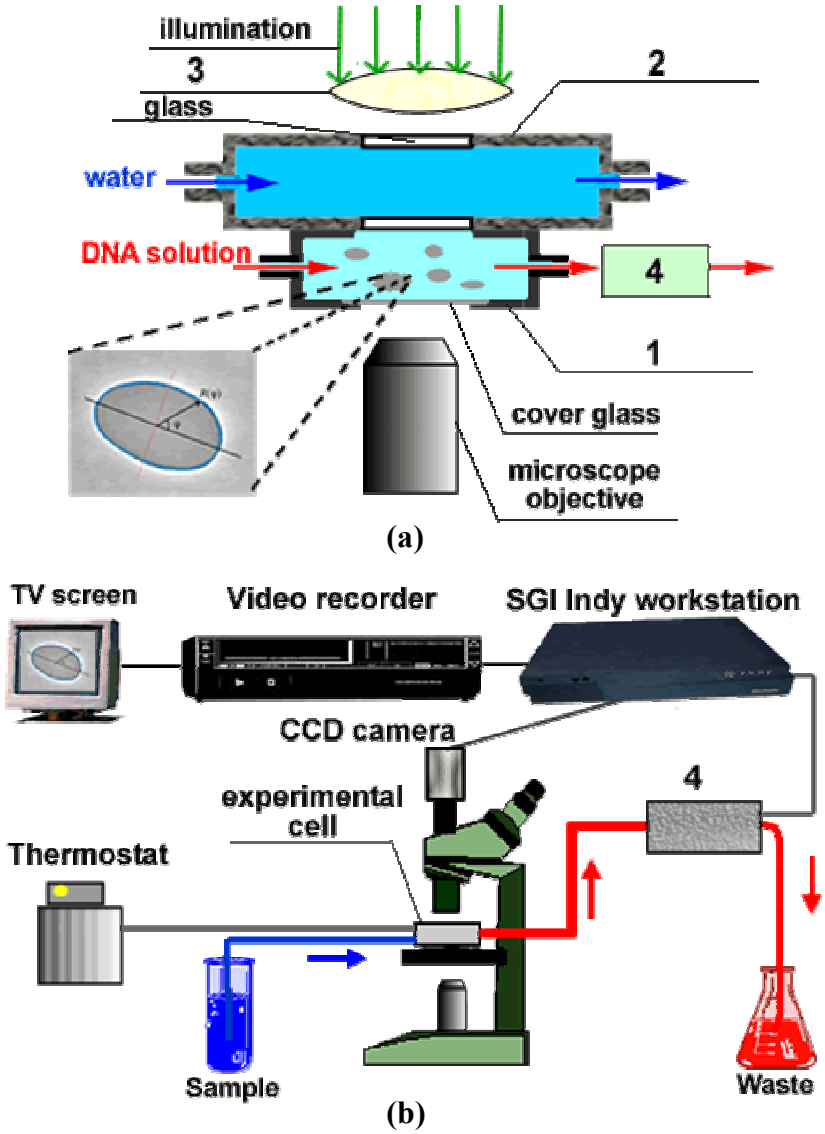

Fig 4.1: (a) A Teflon microchamber (1) is tightly fixed on a hollow, connected to a thermostat, metal holder (2). The running water enables microchamber illumination from the microscope condenser (3). The content of the chamber can be exchanged via a computer controlled micro pump (4). Due to density difference vesicles lie on the bottom of the cell, where the microscope objective is focused; (b) the micropump creates a sample (DNA, albumin etc) flux through the whole chamber. The sample, which is sucked out of it, is stored in a waste container. The microscope is equipped with a CCD camera, whose output signal is send to a SGI workstation. There vesicle contour is digitalized and analyzed. The live picture is recorded on a video tape and for visual control is shown on a video monitor

in the focal plane of the microscope. The long axe fluctuations up/down are negligible [11] and it can be assumed that the vesicle lies in the focal plane.

When the temperature equilibration was completed, the content of the microchamber was scanned. The vesicles visible in the microscope focal plane at the bottom of the chamber usually were highly diverse in (different) shape and size. Some of them were topologically

complex and multilamellar including small vesicles inside larger ones, vesicles with obvious defects, vesicle partially adhered to other vesicles or to the chamber wall, etc. The whole vesicle population was examined to find a "good" vesicle – non-spherical, large enough, unilamellar, fluctuating and without any visible defects. The percentage of usable vesicles was far below one percent. With the means of optical microscopy one cannot observe defects smaller than microscope resolution. When a good vesicle was found its fluctuation spectrum was examined. The image from the CCD camera was send to a SGI Indy workstation. There the 2D contour was digitized and analyzed as described in section 2.3. The signal from the camera was recorded on a video tape and the live picture was simultaneously shown on a video monitor. About 10 min were enough to obtain good statistics about the fluctuation modes of the vesicle. Further in the text such 10 min data set we will refer as to a "measurement". The latter can yield the spontaneous curvature and the bending stiffness of the membrane in this interval of time. A sequence of 10 min measurements will be further referred as to experiment. Usually within 30 minutes three independent measurements were conducted for every "good" – looking vesicle. If the fluctuation spectrum was reproducible, the next step was undertaken; if not – the data was discarded and the microchamber was scanned again for another good vesicle. The next step was to flush gently (with the lowest possible speed of the pump, 200 μl/min) about 500 μl buffer (the same buffer where the vesicle cloud was dissolved) through the chamber. There were two questions to be answered:

1. Is the vesicle fluctuation spectrum affected by shear stress?

Presumably every vesicle is exposed to shear stress from the solvent when DNA solution is introduced inside the chamber. Such stress may result in a change in the vesicle fluctuation spectrum and it must be distinguished from DNA induced changes. Again within 30 minutes three new measurements were conducted with the same vesicle. The fluctuation spectra were obtained and compared with the ones determined before flushing buffer. If a significant difference was detected the microchamber was scanned again for another good vesicle.

2. Does the vesicle lie freely on the bottom of the chamber or is it attached to it?

The cover glass was coated with albumin to prevent adhesion of the vesicles to the chamber wall, because they tend to adhere to glass surfaces. If adhesion is established it will break the vesicle rotational symmetry (assumed by the fluctuation spectroscopy contour digitizing algorithm). Thus in such case the fluctuation spectra cannot be appropriately interpreted. If the vesicle was not drifting while flushing the buffer it was considered as attached and the microchamber was scanned again for another good vesicle.

When the good vesicle was not attached to the cover glass and its fluctuation spectrum did not change significantly under shear stress about 2 ml DNA solution (approximately four times the cell microchamber volume) with concentration about 10^{-13} M was flushed through the chamber with the lowest possible pump flush rate (200 μl/min). Due to the special microchamber geometry almost every point was accessible for the DNA flux created by the pump. The flux however was not everywhere homogeneous and generally the position of the vesicle in the flowing chamber matters. It may be expected that the DNA in the vicinity of a particular vesicle would depend on its location inside the microchamber. This introduced a certain error in the experimental data, because the vesicle position in the chamber could not be controlled. The vesicle spectrum was analyzed as described in section 2.3. The obtained data reflects the changes in the membrane spontaneous curvature and the bending modulus, induced by the anchored DNA molecules.

4.4. Experimental results

By following the experimental procedure, outlined in the previous section, series of experiments with five different surface concentrations of anchors – $0.03\Gamma^{ov}$, $0.06\Gamma^{ov}$, $0.12\Gamma^{ov}$, $0.3\Gamma^{ov}$ and $0.6\Gamma^{ov}$ – were conducted. To facilitate comparison, the concentration of DNA, introduced in the microchamber in each experiment was always in excess and was kept constant, about 10^{-13} M. Thus the amount of anchored polymers depended only on the number of anchors on the vesicle surface. Moreover the asymmetry on both sides of the membrane, arising from the presence of macromolecules in the bulk, is the same for all experiments. The experiments with each surface concentration of anchors showed changes in the membrane spontaneous curvature. Depending on the scale of effect, the obtained data can be classified in three concentration categories:

1. *Group1: Low surface concentration of anchors*

Fluctuation analysis was performed before and after DNA was introduced in the microchamber. The changes in membrane material properties were obtained from the fluctuation spectra. In this category fall the surface concentrations $0.03\Gamma^{ov}$ and $0.06\Gamma^{ov}$

2. *Group2:Intermediate surface concentration*

In some experiments, the vesicles budded when DNA was introduced in the microchamber. In this case the fluctuation spectroscopy cannot be used, because vesicle symmetry was broken, while for the fluctuation analyses it is assumed that the vesicles are axisymmetrical. The change in the spontaneous curvature in this case was estimated from the size of the bud

and the "mother" vesicle. In other experiments, with the same surface concentration of anchors, the vesicle did not but, and the changes in membrane material properties were obtained from the fluctuation spectra. In this category fall the surface concentrations $0.12\Gamma^{ov}$ and $0.3\Gamma^{ov}$

3. *Group 3: High surface concentration and vesicle budding*

In all experiments in this group the investigated vesicles budded when DNA was introduced in the microchamber. The change in the spontaneous curvature was estimated from the size of the bud and the "mother" vesicle.

4.4.1. Low surface concentration of anchors

4.4.1.1. Surface concentration $0.03\Gamma^{ov}$

This is the lowest surface concentration of biotin anchors used in this work. It corresponds to 1 anchor per 44.4 μm^2 of vesicle surface. Presumably in the process of swelling (section 2.2.1.1) each biotin may be expected to bind an avidin molecule. Because of the high avidin concentration in the bulk relative to the surface concentration of biotinylated lipid (biotinyl-CAP-PE), presumably due to the large distance between the biotins (much bigger than the protein dimensions) each avidin may be expected to bind only one biotin. Thus the other three ABS may remain unoccupied and may become DNA anchoring sites or simply anchors. When the biotinylated 3'-end of a DNA molecule (section 2.2.2) establishes contact with an anchor, an ABS-biotin bond is formed and the 3'-end remains fixed to the vesicle surface.

Typical time series of the first two amplitudes from the Fourier expansion of the digitized contour (2.4) - a_2 and a_3 - are shown in fig. 4.2. The first of them (4.2a) was recorded when the vesicle fluctuation spectrum was examined and tested for constancy – prior to flushing buffer through the chamber (identical time series were recorded after that, data not shown). The second (4.2b) was measured after DNA was introduced in the chamber and the vesicle was equilibrated. A drop in the average value of a_2 and a well pronounced decrease in membrane fluctuations were observed. Similar trends were observed in the amplitudes with bigger numbers (data not shown) (identical time series were recorded for the mean square amplitudes $<a_2^2>$ and $<a_3^2>$, where similar decrease in their values was observed, data not shown).

As pointed out in section 2.3 when the thermal fluctuations are small, they can be considered as Gaussian and mean-square amplitudes are proportional to k_BT/κ. Typical histograms, based on the data presented in fig 4.2, are shown in fig 4.3. The amplitude

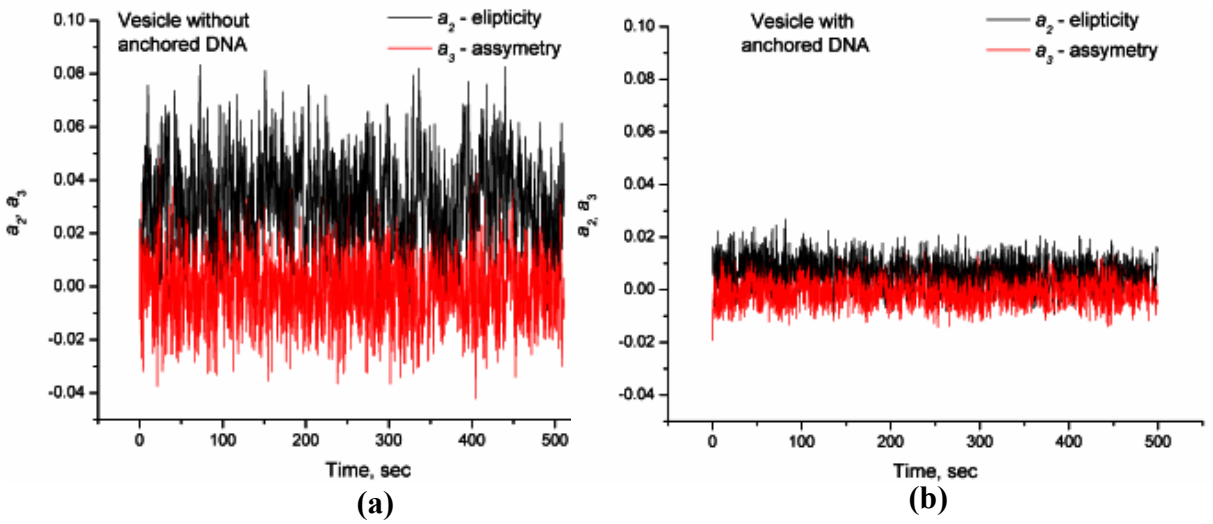

Fig. 4.2: Time series of the a_2 and a_3 amplitudes, 0.03Γ^{ov}. To facilitate the comparison the scales of the vertical axes (a, b) are set to be the same: (a) prior to flushing buffer into the chamber and (b) at the end of experiment, when a well pronounces effect (due to anchored DNA) on the fluctuation spectrum was observed. Notice the drop down in a_2. Due to the anchored DNA, the membrane fluctuations almost vanished.

distribution for the vesicle without anchored polymers is much broader, than the corresponding one for the same vesicle with anchored polymers. Actually the amplitudes for vesicles with reduced volume close to unity, as the vesicle with anchored polymers (image 2 in fig. 4.3), show deviation from Gaussian distribution [11]. Vanishing of the membrane fluctuations as a consequence of anchored polymer is expected because the mean amplitudes of the fluctuation spectrum are inversely proportional to the bending stiffness, which is expected to increase (1.24).

When DNA solution was flushed through the microchamber the prolate shaped vesicle underwent shape transformation to a spherical shaped one. This transition is reflected in the shift of the average value (the histogram maximum) of a_2, which is in fact the vesicle elipticity. The contour of the 2D vesicle cut tends to attain circular shape. The method assumes vesicle axial symmetry (section 2.3) and therefore the whole vesicle shape tends to sphere. The average value of a_3 (vesicle asymmetry) remains the same, close to zero. As is obvious from the images (fig 4.3) the 2D contour has a long axis of symmetry (needed for contour digitization, section 2.3) before DNA was introduced. The distributions of both amplitudes are remarkably narrower – the deviations from the average values are smaller, reflecting the reduced membrane fluctuations.

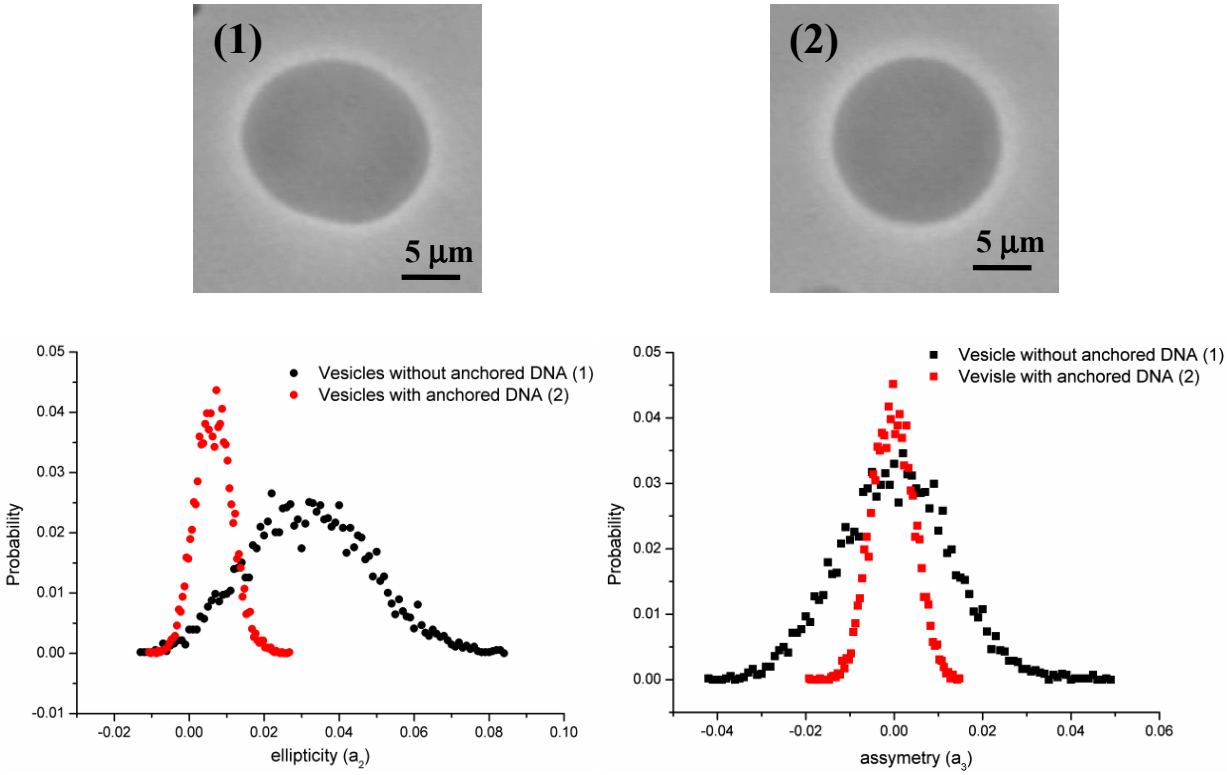

Fig 4.3: Typical histograms for the amplitudes a_2 and a_3, based on the time series, presented in fig 4.2. When decorated with DNA, the vesicle undergoes a shape transformation from prolate to sphere; the deviations from the mean value are smaller, reflecting the vanishing thermal fluctuations. Vesicles were observed in transmitted light with a 40x phase contrast objective. The surface concentration of anchors is $0.03\Gamma^{ov}$.

The effect of anchored DNA on the spontaneous curvature and the bending modulus was quantified by analyzing the changes in the amplitudes of membrane fluctuations. According to equation (2.5) the bending modulus κ can be determined from the slope of the function $\langle a_n^2 \rangle \sim k_B T/\kappa$, where n is the amplitude number. The mean square amplitudes $\langle a_n^2 \rangle$ of the experimentally determined amplitudes for three independent experiments with a single vesicle (before flushing buffer, after that, and after introducing DNA in the experimental microchamber) are shown in fig 4.4, plotted versus $1/n$. They are calculated form the time series measurements as standard deviation from amplitude mean values. The initial slope (before flushing buffer) and the one after buffer was flushed are slightly different. The difference however is much smaller than the effect of DNA, which is well pronounced and resulting in a decrease of the mean square amplitudes especially in $\langle a_2^2 \rangle$ and $\langle a_3^2 \rangle$. Due to this decrease the $\langle a_n^2 \rangle$ drop below their initial values, indicating an increase in the bending stiffness [92]. The question whether the anchored DNA leads to a (measurable) change in the bending stiffness can be answered if the amplitudes of the experimentally determined

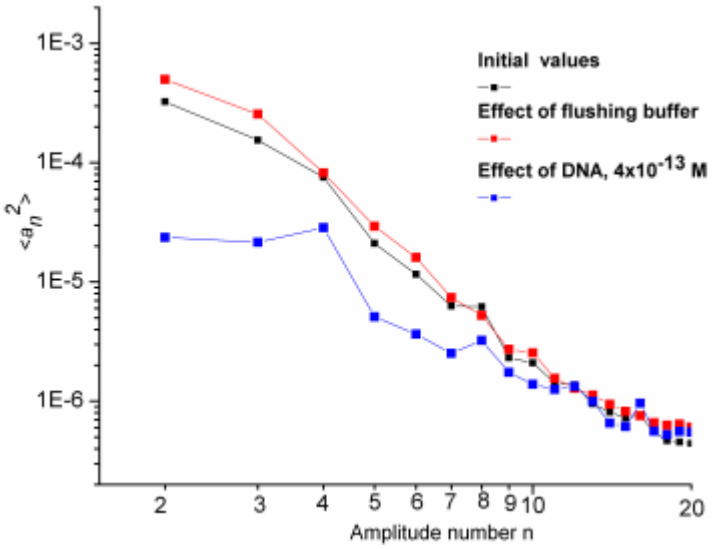

Fig 4.4: The mean square amplitudes for three different experiments – before flushing buffer through the chamber, after that and at the end of the measurement, when DNA reduced thermal fluctuations were observed. The first amplitude cannot be distinguished from zero and is not shown. The surface concentration of anchors is 0.03Γ^{ov}.

fluctuation spectrum are matched with the corresponding amplitudes generated with MC-simulations (section 2.3.3).

The change in the spontaneous curvature, induced by the anchored DNA was determined in a similar way. There in no analytical relation between the spontaneous curvature and the fluctuation spectrum. The following empirically deduced relation was used instead:

$$m_{sp} \propto \frac{\langle a_3^2 \rangle}{\langle a_2^2 \rangle} \tag{4.1}$$

Here m_{sp} is the defined in equation (1.8) reduced spontaneous curvature. The absolute value of m_{sp} can be obtained when the experimentally measured fluctuation spectrum is compared with MC-generated fluctuation spectra, as described in section 2.3.3.3 (such comparison was not performed in this wok). The reduced spontaneous curvature is related to the spontaneous curvature M_{sp} with the equation $m_{sp}=R_A M_{sp}$, where R_A is the area equivalent radius (see section 1.4). The latter was experimentally determined for every investigated vesicle. Because the exact value of the reduced spontaneous curvature in (4.1) is not known, we deduce the quantity M'_{sp} which a fluctuation spectroscopy experiment gives

$$M'_{sp} = \frac{1}{R_A} \frac{\langle a_3^2 \rangle}{\langle a_2^2 \rangle} \propto M_{sp} \tag{4.2}$$

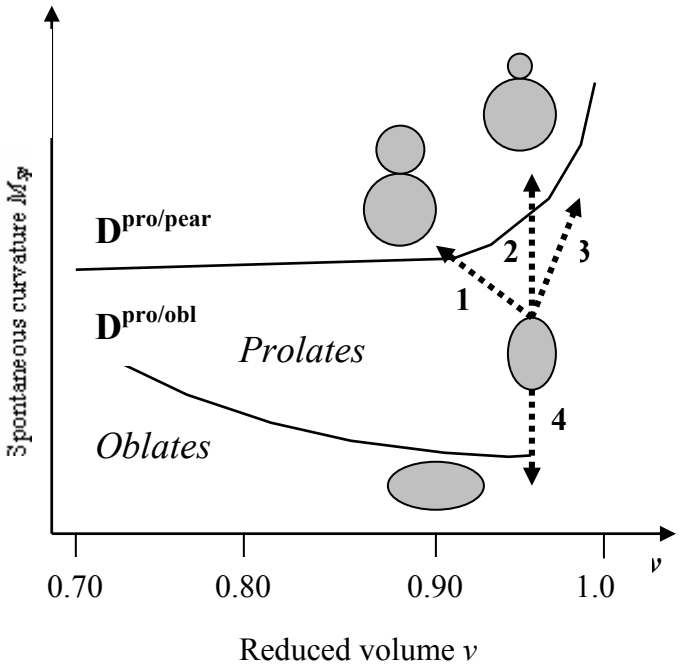

Fig. 4.5: Schematic representation of the prolate region of the ADE phase diagram (fig. 1.5). A prolate vesicle can move by following different trajectories: (1) decrease in the reduced volume v, increase of the spontaneous curvature M_{sp} and budding; (2) v=const, increase in the spontaneous curvature and budding; (3) increase of the reduced volume and the spontaneous curvature without budding; (4) v=const, decrease of M_{sp} and prolate-oblate transition. The vesicle can follow trajectories, which are not shown (see [12]).

Equation (4.1) is based on the work [11] about trajectories of vesicles in the phase diagram of ADE-model (fig. 1.5). Let us consider a prolate vesicle, whose spontaneous curvature increases due to anchored polymers. If the reduced volume is not too small[2] (see fig. 4.5), it can move up in the diagram and undergo budding transition. This transition corresponds to an increase in the spontaneous curvature. Close to the budding transition the amplitude the value of a_3 and the mean square amplitude $\langle a_3^2 \rangle$ are maximal [11]. If the spontaneous curvature decreases, then a prolate vesicle moves down in the phase diagram to prolate-oblate transition, the elipticity a_2 and the mean square $\langle a_2^2 \rangle$ are maximal [11]. Thus if the spontaneous curvature of such vesicle changes the change can be characterized by analyzing the vesicle trajectory in the phase diagram. Several possible vesicle trajectories in the prolate region of the ADE phase diagram are sketched in fig. 4.5. Even if a vesicle follows the trajectories 1 and 3 where the reduced volume changes the spontaneous curvature can be estimated from (4.1) (only if the change of the reduced volume is not too big). The reduced volumes of the vesicles presented in this work are in the range from 0.914 to 0.999. The reduced volume (defined in equation 1.7) is a measure for the enclosed volume of the vesicle and the membrane area available for changes. Spherical vesicles (v=1), for example, have no free area available for shape changes.

In this work we aim to check the change in the spontaneous curvature, induced by anchored DNA. The polymer induced effect should be distinguished from the vesicle spontaneous curvature, which arises from other factors (e.g. asymmetrical distribution of particles in leaflets of the bilayer, different salt concentrations inside/outside the vesicle, flip-

[2] The vesicle should remain in the prolate region of the ADE phase diagram

flop effects etc). As already described, there are three distinct phases in every experiment: test for stability of the fluctuation spectrum, shear stress test and flushing DNA. Because of the selection of vesicles whose fluctuation spectrum is not affected from shear, one may expect that the measured spontaneous curvature M'_{sp} is identical for the first two phases. Let us denote this quantity as $M'_{sp,ini}$. Let us denote the corresponding spontaneous curvature at the end of the experiment (at the end of the third phase, where DNA was introduced) with $M'_{sp,fin}$. We assume that all factors, which may induce spontaneous curvature result in $M'_{sp,ini}$ (during the last phase the experimental conditions are kept the same and the presence of DNA is the only new factor). Thus the effect from the anchored DNA can be separated from the other factors if one considers the difference $\Delta M'_{sp} = M'_{sp,fin} - M'_{sp,ini}$. Further in the text $\Delta M'_{sp}$ will be considered as the DNA induced spontaneous curvature. Moreover it was found (by making statistics count over 60 vesicles) that $M'_{sp,ini}$ varies in a broad range (0.0002÷0.005 μm^{-1}, data not shown). Presumably the value of $M'_{sp,fin}$ will depend on the initial spontaneous curvature of the vesicle. By using $\Delta M'_{sp}$ (instead $M'_{sp,fin}$) one can compare the changes in the spontaneous curvatures of different vesicles (see section 4.5).

In fig 4.6 the time evolution of the ratio $\langle a_3^2 \rangle / \langle a_2^2 \rangle$ is shown. In fact this is data from the experiment, presented on fig 4.4, but we are show all measurements conducted in the frame of one experiment with a single vesicle. The whole experiment (as described before) is separated in three phases - test of fluctuation spectrum constancy, shear stress test by flushing buffer and pumping DNA inside the experimental microchamber. In the figure the phases are separated with vertical dashed lines. Obviously the flushing buffer does not have a measurable influence on the fluctuation spectrum, unlike flushing DNA which in contrast changes significantly the membrane fluctuations. The increase in the spontaneous curvature was not observed immediately after DNA was introduced in the microchamber, presumably because this vesicle was close to the edge of the microchamber, away from the DNA flux created by the pump. In this case it is expected that the DNA molecules need some time to diffuse to the place where the vesicle is located. Further in the text as a final change for the ratio $\langle a_3^2 \rangle / \langle a_2^2 \rangle$ we have taken the maximal reached equilibrium value. For this experiment it was found that $M'_{sp,ini}$=0.0155 μm^{-1}, $M'_{sp,fin}$=0.0227 μm^{-1} and $\Delta M'_{sp}$=0.0072 μm^{-1}. On the average the value of $\Delta M'_{sp}$ for this surface concentration of anchors is 0.0064 ± 0.0011 μm^{-1}, averaged over two vesicles. The reduced volumes of vesicle A (at the beginning of the

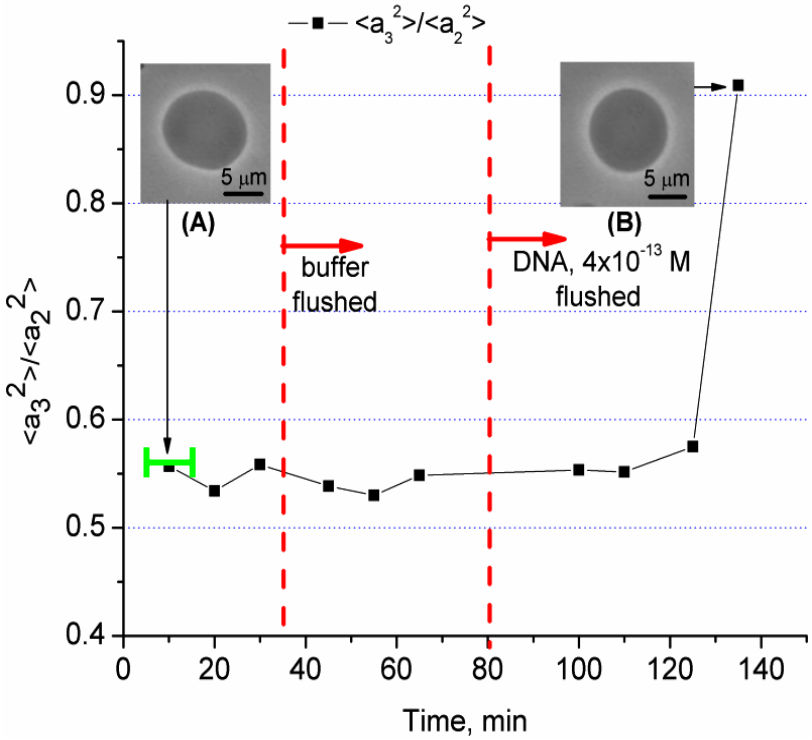

Fig. 4.6: Time evolution of the membrane spontaneous curvature (expressed in terms of the ratio $<a_3^2>/<a_2^2>$). Each point corresponds to a single measurement with duration of approximately 10 min and lies in the middle of such 10 min interval, representing the measurement duration (shown with a green line for the first measurement only). The two vesicle images (A) and (B) present the DNA induced shape transformation prolate to spherical vesicle. The dashed lines separate the three steps followed when the experiment was conducted – test of fluctuation spectrum constancy, shear stress test by flushing buffer and flushing DNA. Flushing buffer does not induce any changes in the spontaneous curvature M_{sp}, while the introduction of DNA results is a drastic increase in $<a_3^2>/<a_2^2>$. No further measurements were conducted after the last, presented in the figure, because the fluctuations vanished and a fluctuation spectroscopy was not possible. The reduced volumes of vesicle A and B are 0.9989 and 0.9999. The surface concentration of anchors is $0.03\Gamma^{ov}$.

experiment) and B (at the end of the experiment) (fig. 4.6) are 0.9989 and 0.9999. The vesicle follows trajectory 3, shown in fig. 4.5 – the reduced volume decreases, the spontaneous curvature increases, but the vesicle remains in the prolates region (no budding was observed). Because vesicle volume is osmotically fixed (remains constant) the decrease in the reduced volume is due to loss of free area. The latter is the reason for the reduced vesicle fluctuations when DNA was introduced in the measuring chamber.

4.4.1.2. Surface concentration $0.06\Gamma^{ov}$

This is the second surface concentration of anchors (1 anchor per 22μm^2 vesicle area) classified in *Group 1* (low surface concentration of anchors), where the anchoring of DNA did not induce vesicle budding. The changes in membrane material properties were deduced in

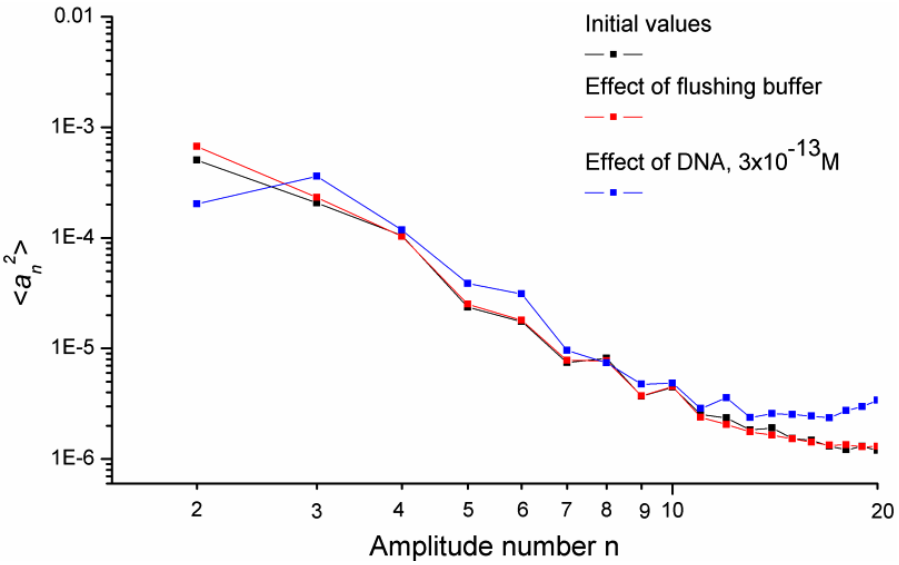

Fig. 4.7: The mean square amplitudes for three different experiments – before flushing buffer through the chamber, after that and at the end of the experiment. The first amplitude cannot be distinguished from zero and is not shown. The surface concentration of anchors is 0.06Γ^{ov}.

the same manner as for the previous surface concentration - from the change in amplitudes of the fluctuation spectrum. Experimental data for the mean square amplitudes $\langle a_n^2 \rangle$ for three different measurements on a single vesicle (before flushing buffer, after that, and after introducing DNA in the experimental microchamber) is shown in fig. 4.7. The initial slope of the mean square amplitudes versus the amplitude number and the one after exposing the vesicle to shear stress are identical – the membrane bending rigidity does not react to shear stress. When DNA was introduced in the microchamber, a shift down in $\langle a_2^2 \rangle$ and up in $\langle a_3^2 \rangle$ was observed. As in the case with surface concentration *0.03Γ^{ov}*, due to this shift the slope is worse defined and the error from the linear fit is bigger than the fit error of the same slope before introducing DNA. Therefore a possible increase in the bending stiffness cannot be resolved, because it would be smaller than the experimental error. The shift in the mean square amplitudes (while $\langle a_3^2 \rangle$ increases $\langle a_2^2 \rangle$ decreases) after pumping DNA according to equation (4.1) corresponds to an increase in the membrane spontaneous curvature. The time evolution of the ratio $\langle a_3^2 \rangle / \langle a_2^2 \rangle$ for all measurements performed within a single experiment is shown in fig. 4.8. Each point lies in the middle of 10 minute interval, corresponding to the duration of a single measurement. The three phases of the experiment are separated by vertical dashed lines. The shear stress did not induce any measurable effect on the spontaneous curvature. In contrast the change in the spontaneous curvature, induced by the anchored DNA molecules is very well pronounced as a big increase in the ratio $\langle a_3^2 \rangle / \langle a_2^2 \rangle$. The increase was not observed immediately, presumably because this vesicle

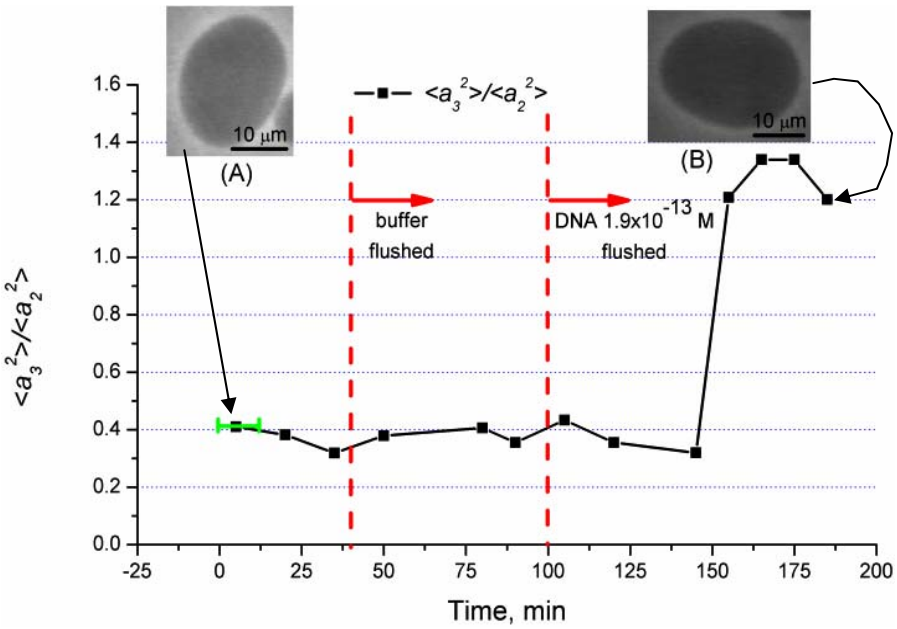

Fig 4.8: Time evolution of the ratio $\langle a_3^2\rangle/\langle a_2^2\rangle$ for a vesicle with surface concentration of anchors $0.06\Gamma^{ov}$. Each point corresponds to a single measurement and lies in the middle of 10 minutes interval, representing the measurement duration (shown with a green line for the first measurement only). Both vesicle pictures (A) and (B) are to underline that no shape transformations were observed. The dashed lines separate the three steps of the experiment– test of the fluctuation spectrum constancy, shear/adhesion stress test by flushing buffer and flushing DNA. The last steps results in a drastic increase in M_{sp}. The reduced volumes of vesicle A and B are 0.995 and 0. 0.975

was close to the edge of the microchamber, away from the DNA flux and some time for DNA diffusion was necessary. Notice the plateau region at the end of experiment – the spontaneous curvature does not increase any more, but fluctuates around an average value. Presumably the whole amount of avidin anchors on the vesicle surface is occupied and the fluctuations around the final average value of the spontaneous curvature are due to the experimental error. A second possibility is if the whole amount of DNA close to the membrane is bound and no further binding of DNA is possible (this scenario however is not very probable, because the DNA in the flow chamber is in excess, see *Appendix F*). For this experiment it was found that $M'_{sp,ini}$=0.0097 μm^{-1}, $M'_{sp,fin}$=0.0328 μm^{-1} and $\Delta M'_{sp}$=0.0072 μm^{-1}. On the average the value of $\Delta M'_{sp}$ for this surface concentration of anchors is 0.0146 ± 0.008 μm^{-1}, averaged over three vesicles. The reduced volumes of vesicle A (at the beginning of the experiment) and B (at the end of the experiment) (fig. 4.8) are 0.995 and 0. 0.975. The vesicles follows trajectory 1, but does not cross the phase boundary and remains in prolates region (no budding was observed).

4.4.2. Intermediate surface concentration of anchors

4.4.2.1. Surface concentration $0.12\Gamma^{ov}$

This is the lower of two surface concentrations of anchors falling in *Group 2* (intermediate surface concentrations), corresponding to 1 anchor per 11 μm^2 of vesicle surface. The main difference from the data presented in *Group 1* is that while some of the experiments proceed as in the first group, in others the vesicles budded when DNA was introduced in the microchamber. In case of budding the fluctuation spectroscopy measurement cannot be performed because the technique assumes that the vesicle is axisymmetrical (section 2.3) and a bud attached to its surface (inner or outer) breaks the symmetry. Nevertheless the spontaneous curvature can be estimated from the sizes of the bud (and the "mother" vesicle). In other experiments, with the same surface concentration of anchors, the investigated vesicles did not bud, and the changes in membrane material properties were obtained in the same way as for the experiments from *Group 1*.

In fig. 4.9 (a, b) is presented data from an experiment where no morphological transformations were observed. The mean square amplitudes $\langle a_n^2 \rangle$ for three different measurements with a single vesicle (before flushing buffer, after that, and after pumping DNA in the experimental microchamber) are shown in fig 4.9a. Similarly to the experiments with lower surface concentration of anchors, flushing buffer does not have any measurable impact on the bending stiffness (proportional to the slope defined from the function $\langle a_n^2 \rangle \sim k_B T/\kappa$). The effect of DNA is expressed in a decrease in $\langle a_2^2 \rangle$ and an increase in $\langle a_3^2 \rangle$. Such change, according to (4.1) indicates an increase in the spontaneous curvature. The slope however does not change significantly and a possible increase in the bending stiffness is smeared within the experimental error. An increase in the membrane spontaneous curvature was observed immediately after DNA was introduced in the microchamber (fig 4.9b). The effect of DNA is much stronger than the effect of flushing buffer only. There are two distinct, well defined, regions in the spontaneous curvature evolution curve: *(i) before and after flushing buffer*. In this region the spontaneous curvature fluctuates, presumably due to the experimental error, *(ii) after DNA was introduced*. The spontaneous curvature increases after the fist 30 min after DNA was flushed through the microchamber. The polymer molecules need some time to diffuse to vicinity of the vesicle. Moreover once there, the biotinylated end has to find an anchor, residing on the membrane surface. Presumably the

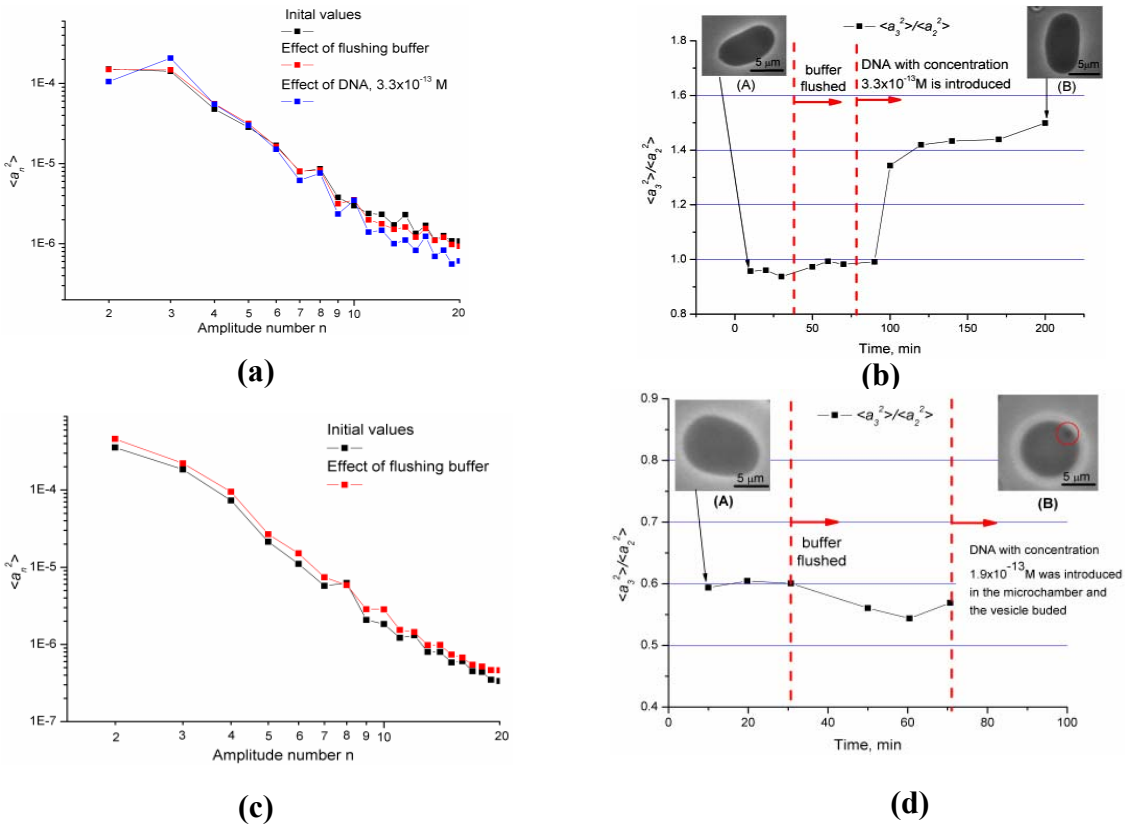

Fig 4.9: Two different types of DNA induced changes in the membrane material properties – increase in the spontaneous curvature without (a, b) and with (c, d) morphological transformations; (a) the mean square amplitudes for three different measurements – before flushing buffer through the chamber, after that and at the end of the experiment, (b) The time evolution of the ratio $<a_3^2>/<a_2^2>$. Each point corresponds to a single measurement and lies in the middle of 10 minutes interval, representing the measurement duration. The reduced volumes of vesicle A and B are 0.932 and 0.914; (c) the mean square amplitudes for two different measurements – before flushing buffer through the flow chamber and after that. When DNA was introduced in the microchamber the vesicle budded and the fluctuation spectroscopy measurement was interrupted; (d) the introduction of DNA resulted in a drastic increase in the spontaneous curvature, accompanied with bud formation, shown with a red circle. The bud remained connected to the "mother" vesicle and its size was about 1.2 μm. The reduced volume of vesicle A is 0.954. See *Appendix D* for detailed image. The surface concentration of anchors is $0.12\Gamma^{ov}$.

reason for the plateau region (no further increase of the spontaneous curvature) is that all avidin anchors on the vesicle surface have been occupied and no further binding of DNA was possible. For this experiment it was found that $M'_{sp,ini}$=0.0282 μm^{-1}, $M'_{sp,fin}$=0.0445 μm^{-1} and $\Delta M'_{sp}$=0.0163 μm^{-1}

The second type of experiments from this group is the one where the vesicles budded when DNA was introduced in the microchamber. These experiments were conducted in the same way as was described before – by separating the whole experiment in three phases.

Figure 4.9c shows the mean square amplitudes as a function of amplitude number. Only measurements before and after flushing buffer were possible, because of the vesicle budding when DNA was introduced. Notice the excellent reproducibility of the amplitude data. The slope is well defined and the bending rigidity can be found by matching the experimentally measured and the generated with Monte Carlo simulations fluctuation spectra. This bending stiffness however is a property of a membrane without anchored DNA. Due to vesicle budding similar measurements were impossible when DNA was introduced.

The time evolution of the spontaneous curvature is shown in fig. 4.9d. In fact it slightly decreased when the buffer was flushed. Even though bigger than any other buffer induced change, it is still smaller than the DNA induced effects. When DNA was pumped in the experimental chamber, the vesicle budded. The bud was very small (diameter of about 1.2 μm), indicating a very big increase in the spontaneous curvature. For a spherical surface the spontaneous and the geometrical curvatures are identical, defined as *1/R*, where *R* is the surface radius and therefore the smaller the radius, the bigger curvature. The bud image is much darker than the glucose solution, surrounding the vesicle. Therefore the bud should be external and containing sucrose solution. It is expelled from the "mother" vesicle, but is still attached to it. If the bud was internal – when a vesicle bends inwards from outside to inside, the bud would contain glucose solution and its grayscale would be lighter than the vesicle one. When DNA is introduced in the microchamber, the prolate vesicle (image A in fig 4.8d) moves up in the ADE-model phase diagram (fig. 4.5) towards higher spontaneous curvatures, until it crosses the budding transition phase boundary, where it buds. This vesicle had the smallest reduced volume (v=0.954) of all vesicles where budding was observed. The diameter of the main bud (about 4.1 μm) was the biggest one observed in all conducted experiments. As explained before, the reduced volume is a direct measure for the free area of a vesicle thus one may speculate that the bud size is related to the vesicle free area (the larger free area, the bigger bud).

4.4.2.2. Surface concentration 0.3Γ^{ov}

This is the second surface concentration of anchors classified in *Group 2*, corresponding to 1 anchor per 5.5 μm^2 of vesicle surface. As in the previous case (0.12Γ^{ov}) in some experiments the investigated vesicles budded when DNA was flushed through the experimental chamber. In other experiments, the DNA induced increase in the spontaneous curvature was smooth, without budding shape transformations. Experimental data for the latter case is shown in fig. 4.10(a, b). The vesicle fluctuation spectrum did not change after

applying shear stress (by flushing buffer through the microchamber). As was observed in the experiments with the previous surface concentrations, when DNA was introduced inside the microchamber the fluctuations decreased. That is clearly visible from the decrease in the mean square amplitude of the fluctuation spectrum (fig. 4.10b). In contrast, a very well pronounced increase in the spontaneous curvature was observed when DNA was flushed through the experimental cell. Notice the extent of the increase – larger than any other one, measured in the experiments with lower surface concentration (of course, it can be compared only with experiments where budding transitions were not observed). Similar effect (large increase) was observed in experiments, conducted with the other ($0.06\Gamma^{\infty v}$ and $0.12\Gamma^{\infty v}$) surface concentrations of anchors. No further measurements were conducted after the last, presented in the figure, because the fluctuations vanished and fluctuation spectroscopy measurements were not applicable. The vanishing fluctuations indicate a loose a free area. The reduced volume, however, remains constant (v=0.998) during the whole experiment. Presumably the vesicle follows trajectory 2 (fig. 4.5), the spontaneous curvature increases, but the vesicle remains in the prolate region and does not cross the prolate/pear phase boundary (does not bud). For this experiment it was found that $M'_{sp,ini}$=0.0109 μm^{-1}, $M'_{sp,fin}$=0.0345 μm^{-1} and $\Delta M'_{sp}$=0.0236 μm^{-1}.

Experimental data for the DNA induced vesicle budding is shown in fig. 4.10(c, d). The fluctuation spectra of all three different measurements, presented in fig. 4.10a are very well reproducible. In this experiment shear stress test measurements (by flushing buffer) were not performed. When spectra identity was observed, DNA was pumped in the experimental microchamber. In fig 4.10d the time evolution of the ratio $\langle a_3^2\rangle/\langle a_2^2\rangle$ is presented. It is constant (within the experimental error) for 45 minutes. Immediately after DNA was introduced, the vesicle budded. The bud (marked with a red circle on image (B), fig. 4.10d) remained connected to the "mother" vesicle via a tiny tether, which can be seen as well on the same image. The bud diameter is about 4.1 μm, while the diameter of the "mother" vesicle is 12.7 μm. This experiment is actually quite interesting. One can notice that the bud is connected to the "mother" vesicle by a pearl of small vesicles of approximately equal size (about 1.4 μm). A possible interpretation of this event would be that each of the vesicles-pearls has one or several anchored polymers (each pearl should have about four anchors).

4.4.3. High surface concentration of anchors, $0.6\Gamma^{\infty v}$. Vesicle budding.

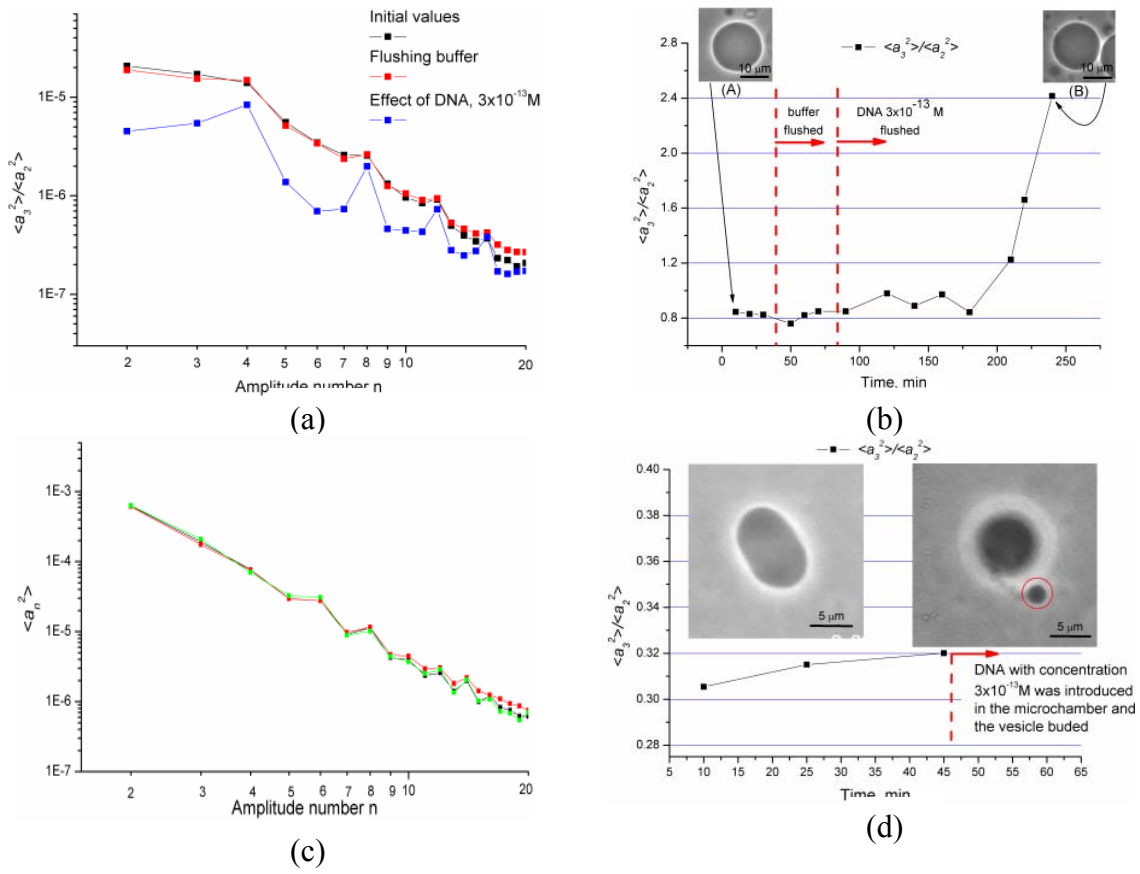

Fig 4.10: Two different effects on the membrane material properties, induced by DNA with the same surface concentration 0.3Γ^{ov} – increase in the spontaneous curvature without (a, b) and with (c, d) morphological transformations (budding); (a) the mean square amplitudes for three different measurements – before flushing buffer through the chamber, after that and at the end of the experiment, (b) Time evolution of the membrane spontaneous curvature. The effect of anchored DNA is expressed in a big increase in $\langle a_3^2\rangle/\langle a_2^2\rangle$. Plateau region was not observed (see the text for details); (c) Tree different measurements aiming to probe the fluctuation spectrum reproducibility, which seems to be excellent. In this experiment DNA was introduced after these three test measurements, (d) the spontaneous curvature changes slightly during the test measurements, but such a change is within the experimental error, determined in the other experiments where shear stress test was performed. When DNA was introduced the vesicle budded. The bud (encircled in red in picture (B)) remained connected to the "mother" vesicle via a tiny necklace of vesicles, visible in picture (B). The diameter of the main bud is about 4.1 μm. The reduced volumes of vesicle A is 0.975. See *Appendix D* for an enlarged and more detailed image.

This is the highest surface concentration of anchors investigated in this thesis and corresponds to 1 anchor per 2.5 μm^2 of vesicle surface. It is classified in a different group, *Group 3*, because the introduced DNA induced budding in every experiment. The fluctuation spectroscopy was inapplicable to determine the DNA induced increase in the membrane spontaneous curvature. The latter was estimated from the sizes of the buds and the "mother" vesicles.

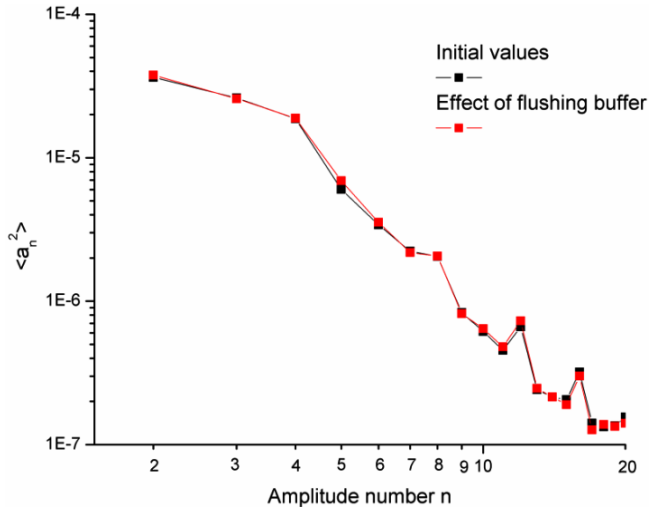

Fig 4.12: The mean square amplitudes for two experiments at $0.6\Gamma^{ov}$ – before and after flushing buffer through the chamber. Notice the excellent reproducibility.

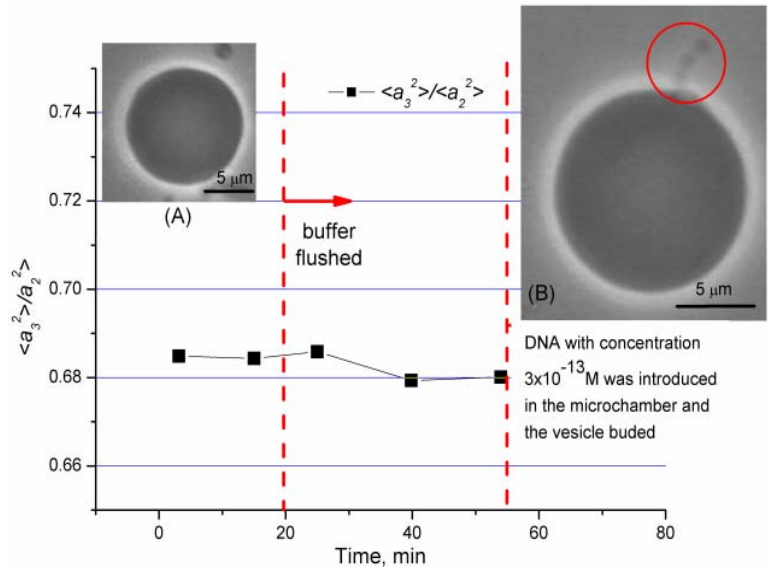

Fig 4.13: The spontaneous curvature changes slightly with time during the test measurements at $0.6\Gamma^{ov}$. This change however is within the experimental error. When DNA was flushed through the microchamber the vesicle budded. The bud remained attached to the "mother" vesicle and can be seen on the upper part of picture (B). It consists of three connected smaller spherical buds with identical sizes – diameter about 1.4 μm. The reduced volumes of vesicle A is 0.997. See *Appendix D* for enlarged and more detailed images.

The experimentally determined mean square amplitudes $\langle a_n^2 \rangle$ for two independent experiments with a single vesicle (before and after flushing buffer) are shown in fig. 4.12 plotted versus *1/n*. Both measurements are very well reproducible reflecting the spectrum constancy with time, which is a hidden parameter (there is a time spacing of about 30 min between the measurements) and stability against shear stress. The time evolution of the

spontaneous curvature is shown in fig. 4.13. When DNA was introduced in the microchamber the vesicle budded. The bud remained attached to the "mother" vesicle with a lace of vesicle pearls, just like in fig. 4.10d. Each of the connected vesicles is with diameter of about 1.4 μm. The buds color appears much darker than the glucose solution, surrounding the vesicle, because they contain the sucrose solution of the "mother" vesicle. When DNA is introduced in the microchamber, the vesicle (image A in fig 4.12) moves up in the ADE-model phase diagram (fig. 4.5) towards higher spontaneous curvatures until it crosses the budding transition phase boundary, it buds.

4.5. Conclusions and discussion

This chapter presented the effects on the material properties of GUVs, induced by long anchored DNA with different surface concentrations were investigated. The latter were calculated in terms of overlapping surface concentration Γ^{ov}. The number of anchors on the vesicle surface was set by controlling the molar ratio DOPC/biotinyl-CAP-PE (the vesicles were made of these two lipids, see section 2.1.1). In the investigated mushroom regime, it is expected that the increase in the membrane spontaneous curvature scales linearly with the polymer surface coverage (see equation 1.23). In order to characterize this dependency experimentally, we worked with five different surface concentrations of anchors. They were lower than the polymer overlapping coverage Γ^{ov}, defined in section 1.2.2, and their values were $0.03\Gamma^{ov}$, $0.06\Gamma^{ov}$, $0.12\Gamma^{ov}$, $0.3\Gamma^{ov}$ and $0.6\Gamma^{ov}$. The experiments were prepared and conducted as described in section 4.3.

When DNA was flushed through the microchamber an instant increase in the membrane spontaneous curvature in some experiments was observed, while in others, a similar increase was observed but after a delay ranging from about 20 min (fig 4.9b) to 80 min (fig. 4.10). Presumably this effect is due to an inhomogeneous distribution of DNA in the bulk. When the DNA solution is flushed through the microchamber (fig. 4.1a), the flux is not homogeneous throughout the chamber and the local concentration of polymer in not uniform. When pumping is completed, the bulk concentration is homogenized due to DNA diffusion. This process however is very slow, because of the low diffusion coefficient of the DNA (0.47 ± 0.03 $\mu m^2/s$, [61]). Therefore one may expect that if the vesicle is close to (or in) a DNA molecules rich region, the anchors on the membrane surface will be occupied faster than if the same vesicle is away from such region and the DNA needs time to diffuse to its surface.

When anchored to the membrane, the DNA induced changes in the spontaneous curvature can be estimated in two different ways: *(i)* by analyzing the thermal fluctuations of the vesicle; *(ii)* by analyzing the dimensions of the bud and the "mother" vesicle (in the case of budding only).

If the investigated vesicle is prolate, unilamellar and without defects then the membrane fluctuation spectrum can be studied and analyzed. The changes in the spontaneous curvature can be estimated from the ratio $\langle a_3^2 \rangle / \langle a_2^2 \rangle$ (see equation 4.1 and 4.2). Such a measure, however, is only qualitative. The absolute value can be obtained when the experimentally determined amplitudes are matched with the corresponding fluctuation spectrum amplitudes, generated with MC-simulations (see section 2.3.3). In this work such comparison (data quantification) was not made. The DNA induced changes in the spontaneous curvature ($\Delta M_{sp}^{'}$) were obtained in this way from the experiments falling in *Group 1* and *Group 2* (the cases without budding).

In case of budding one can estimate M_{sp} from the size of the "mother" vesicle and the expelled bud. If the cross sections of both vesicles are circular one may assume that they exhibit rotational symmetry and have spherical topology. It is a trivial task to obtain the curvature of a spherical surface: from equation (1.4) $M = (1/R+1/R)/2=1/R$, where R is the surface radius. If a bud (B) is connected to a mother vesicle (M) (it is assumed that the compositions of B and M are homogeneous and identical, see [103]) via an infinitely thin neck, the spontaneous curvature of the system is given by [94]

$$M_{sp} = \frac{1}{2}\left(M^M + M^B\right) \tag{4.3}$$

where M^M and M^B are the mean curvatures of the vesicle and the bud respectively. Thus the spontaneous curvature of a vesicle with an attached bud can be estimated if the mean curvatures of the "mother" vesicle and the bud are known (the curvature of a spherical vesicle can be determined if its radius is known). In our experiments, where buds occur (*Group 2* and *Group 3*) the vesicles and the buds had spherical topologies. Their radii (see Table 2) were estimated from the images, shown in figures 4.9d, 4.10d and 4.13. The spontaneous curvature was estimated from (4.3), but it is a combination of the effect of anchored DNA and other factors (outlined above). As in the cases without budding one the DNA induced increase in the spontaneous curvature has to be considered separately. In this case however $\Delta M_{sp}^{'}$ cannot be determined: $M_{sp,ini}^{'}$ was measured from the fluctuation

Surface concentration of anchors	*Mother vesicle radius*	*Bud(s) radius*
$0.12\Gamma^{ov}$ (fig. 4.9d)	6.3 μm	bud 1: 0.6 μm
$0.3\Gamma^{ov}$ (fig. 4.10d)	7 μm	bud 1: 0.7 μm, bud 2: 0.9 μm bud 3: 0.7 μm, bud 4: 0.7 μm
$0.3\Gamma^{ov}$ (fig. 5.3e) Chapter 5	7 μm	bud 1: 1.6 μm, bud 2: 1.6.μm bud 3: 0.6 μm
$0.6\Gamma^{ov}$(fig. 4.13d)	8 μm	bud 1: 0.7 μm, bud 2: 0.7 μm bud 3: 0.7 μm
$0.6\Gamma^{ov}$ (not shown in the text)	5 μm	bud 1: 0.9 μm

Table 2: Size of the bud(s) and the mother vesicle

spectroscopy experiments, but due to budding the measurements of $M'_{sp,fin}$ were impossible. The spontaneous curvatures, obtained from both different methods (fluctuation spectroscopy and bud analysis) are not comparable ($M'_{sp,fin}$ is proportional to the absolute value M_{sp} of the membrane spontaneous curvature, see equation 4.2). Thus $\Delta M'_{sp}$ cannot be estimated from $M'_{sp,ini}$ and M_{sp}. In order to estimate the DNA induced curvature it was assumed that the contribution of the mother vesicles to the total spontaneous curvature is small and can be neglected. Indeed, from Table 2 it is obvious that the diameters of the mother vesicles are about 10 times larger than the diameters of the buds. This assumption introduces about a 10 percent error in equation 4.3. Presumably budding is induced from the anchored DNA, because it was observed only after polymer solution was flushed through the flow chamber. Further in the text we consider only the bud contribution to the total spontaneous curvature M_{sp} (see equation 4.3)

The change of the membrane spontaneous curvature, induced by anchored DNA as a function of the surface concentrations of anchors is shown in fig. 4.14. The data from the fluctuation spectroscopy (black line) and the bud analysis data (red line) for every surface concentration of anchors was averaged over all conducted experiments with this surface concentration (two fluctuation spectroscopy experiments with $0.03\Gamma^{ov}$, three fluctuation spectroscopy experiments with $0.06\Gamma^{ov}$, one fluctuation spectroscopy and one bud analysis experiments with $0.12\Gamma^{ov}$ and $0.3\Gamma^{ov}$, two bud analyses experiments with $0.6\Gamma^{ov}$). The point at $0\Gamma^{ov}$

Group 2	$0.12\Gamma^{ov}$	$0.3\Gamma^{ov}$
No budding	v=0.932	v=0.998
Budding	v=0.959	v=0.975

Table 3: The reduced volumes of the vesicles classified in *Group 2*

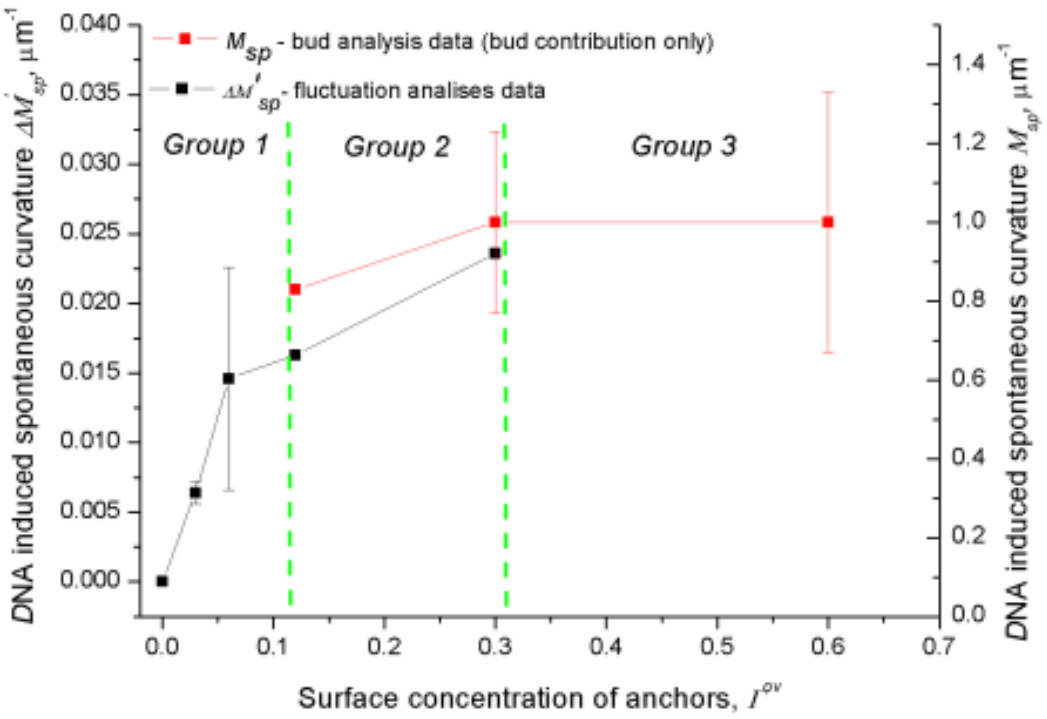

Fig. 4.14: The effect on the membrane spontaneous curvature, induced by anchored DNA with different surface concentrations. The left vertical axis represents the dimensionless spontaneous curvature (black curve), calculated from (4.1). The right vertical axis is for the spontaneous curvature, estimated from bud analysis (red curve). The horizontal axis represents the expected surface concentration of anchors, calculated in terms of overlapping surface concentration. I^{ov}

corresponds to the case of membrane without anchored polymers.

As already noted, the spontaneous curvatures, obtained with the two different methods - fluctuation spectroscopy and bud analysis - cannot be compared and are shown separately in the figure. Nevertheless one can employ an empirical rule and to argue that in every case where budding was observed, the increase in the spontaneous curvature is larger than in the cases without budding (if the difference in the reduced volumes of the vesicles from different experiments is not very big). Let us consider the prolate region of the ADE phase diagram (fig. 4.5). When the spontaneous curvature increases (e.g. due to anchored polymers) the vesicle moves up in the phase diagram (possible trajectories were sketched in fig. 4.5). If the reduced volumes of two vesicles (from different experiments) are not very different and if M_{sp} increases one may assume that both vesicles follow the same trajectory. Thus if the first of these two vesicle buds and the second does not, the increase of the spontaneous curvature of the first vesicle should be larger than the corresponding increase of the second one. Such comparison can be made for the experiments from *Group 2 (intermediate surface*

concentrations). The reduced volumes of the vesicles (from the measurements before DNA was introduced) are summarized in Table 3. The differences between the reduced volumes of the vesicles which bud and which do not bud (for both surface concentrations) is relatively big, but we assume that in both cases the vesicle follows similar (not very distant trajectories) and the spontaneous curvature in the cases of budding is bigger than in the cases where budding was not observed. Similar comparison cannot be made for the experiments from *Group 3*, because all vesicles bud.

Because the vesicle spontaneous curvature in the cases of budding is larger (than the cases without budding), the curve obtained from the bud analysis data should be "above" the corresponding curve obtained from the fluctuation analyses data. (fig. 4.14). The spacing between the two cures is arbitrary, because the mentioned empiric rule cannot be used for data quantification. The bud analysis yields the absolute value of the spontaneous curvature, while the spontaneous curvature obtained from the fluctuation spectroscopy is proportional to the actual change (see equation (4.2)).

As demonstrated in fig. 4.14, up to $0.3\Gamma^{ov}$ the DNA induced spontaneous curvature increases with the increase of the surface concentration of anchors. This behavior can be explained with the relatively low bulk concentration of DNA inside the experimental flow chamber. In *Appendix F* we present an estimation that if a uniform distribution of the polymer inside the experimental cell is assumed then within one hour (the averaged time for all experiments to observe effect on the membrane spontaneous curvature when polymer solution was introduced in the experimental microchamber) about 30 DNA molecules can diffuse and presumably bind to the investigated vesicle. Thus regardless of the increased surface concentration of anchors the number of anchored DNA is approximately constant. Note however that in the discussion so far regarded to the surface concentration of *anchors* and the DNA induced spontaneous curvature, but it was not specified how many DNA were attached to the avidin anchors. Experimentally we control the number of avidin anchors on the membrane surface. One may expect that when an experiment is conducted, some anchors will remain unoccupied. Thus the effective surface concentration of anchored DNA can be smaller than the one of the anchors. In the next chapter we present attempts to quantify (by using fluorescence) the number of DNA molecules, anchored to vesicles with different surface concentrations of anchors. When this number is estimated, in order to compare the theoretical expectation and experimental data (see section 1.3) we will come back to the changes in the membrane spontaneous curvature, presented in fig. 4.14.

Chapter 5

Detecting anchored DNA by fluorescence measurements

5.1. Overview and motivation

This work has for objective to perform a systematic investigation and to quantify the changes in membrane material properties, induced by anchored long DNA with different surface concentrations. As explained in the previous chapter, the surface concentration of DNA anchors was varied by controlling the number of avidin anchors residing on the membrane surface. The working surface concentrations of the latter were calculated in terms of the overlapping concentration Γ^{ov} (see section 1.2.2) and they were $0.03\Gamma^{ov}$, $0.06\Gamma^{ov}$, $0.12\Gamma^{ov}$, $0.3\Gamma^{ov}$ and $0.6\Gamma^{ov}$. When an experiment is performed (as described in the previous chapter), the number of DNA molecules, anchored to a particular vesicle depends on the location of the latter in the experimental microchamber. Inside the chamber DNA molecules can be transported to the vicinity of a vesicle by two mechanisms – convection and diffusion. Convection occurs due to the flux (created by the micropump) of sample through the flow chamber. This flux however does not create a uniform distribution of DNA within the chamber volume. If the investigated vesicle is away from the flux, the relevant mechanism for DNA transportation to the membrane is diffusion. Because of the very small diffusion coefficient of λ-DNA molecules, it might happen that only few of them can approach the vesicle and bind to the anchors within the experiment duration. In this case the number of available for binding polymers in the vicinity of the vesicle might happen to be much smaller than in the case with convection. Thus one can distinguish two different surface concentrations of DNA – virtual (the corresponding to the number of anchors) and actual (the number of anchored polymers). They will coincide only if each anchor on the surface is occupied by a DNA molecule. Notice that in every other case the actual polymer coverage on a particular vesicle will be lower than the surface concentration of anchors (the virtual surface concentration).

The actual surface concentration of the anchored to a given vesicle DNA may vary within the range from zero (no anchored ones) to the virtual surface concentration (all anchors are occupied). Theoretical calculations predict that in mushroom regime (which is investigated in this thesis) the effect of the anchored DNA on the membrane spontaneous curvature scales linearly (see equation 1.23) with the polymer surface coverage. Therefore the knowledge of the exact number of anchored DNA per vesicle (the actual surface coverage) is of central importance.

The previous chapter presented a detailed study on the effect of anchored DNA with different virtual concentrations on the spontaneous curvature of prolate vesicles. In this chapter we attempted to estimate the actual surface concentration (for a given virtual one) of the polymer. The approach to obtain this information was to employ three different types of fluorescence detection techniques: fluorometry, fluorescent microscopy and laser scanning confocal microscopy (LSCM). These techniques can indirectly (fluorometry) or directly (fluorescence microscopy and LSCM) obtain information about the number of DNA, anchored to vesicles with a given working (virtual) surface concentration of anchors. Such measurements are presumably possible, because the DNA molecules used in this work were fluorescently labeled with TOTO-1 (see section 2.2.3).

5.2. Sample preparation

The samples for the fluorometric and confocal microscopy measurements were prepared by following a procedure very similar to the one outlined in section 4.2. The bottle with swelled GUV was opened prior to each experiment. A small amount of sucrose solution (about 150 µl) was taken out and its osmolarity was measured. The typical osmolarities for the experiment with fluorometry were ranging in the interval 400-500 mOsm/g (the necessity for such high osmolarity will be explained later). The one for the measurements with fluorescent microscopy and LSCM was 150-200 mOsm/g (as in the experiment with fluctuation spectroscopy). A glucose solution (in the same buffer as the sucrose one) with slightly higher osmolarity of (about 5-7 mOsm/g was prepared). The characteristic cloud of vesicle suspension was gently taken out of the bottle with a pipette and was dissolves in the glucose solution. Biotinylated and fluorescently labeled DNA were added in the vessel with the vesicle solution. The vessel volume (about 500µl) and the total concentration of DNA (about 10^{-13} M) were chosen on purpose. The goal was to simulate as close as possible the

experimental conditions in the microchamber, where the experiments with fluctuation spectroscopy were conducted. The incubation time of the sample was about 2 hours.

5.3. Fluorescence microscopy

Fluorescence microscopy equipment (Till-Photonics) was installed in the experimental setup, used to visualize vesicles and to perform the fluctuation spectroscopy experiments for this work. The equipment comprised of a computer controlled CDD camera (Till-Imago), a frame grabber, a monochromator, software for data acquisition and image processing and a PC. To keep the picture clear, this equipment was not shown in the figure sketching the experimental setup (fig. 4.1). Both measurements (fluctuation spectroscopy and fluorescence detection) could be performed with the same sample by changing the light source and the detection camera. This is demonstrated in *Appendix D*, where a sketch of the optical paths inside the used microscope (Zeiss Axiovert 135 TV) is shown. At the end of every fluctuation spectroscopy experiment we attempted to conduct a measurement of the signal from the fluorescently labeled DNA, anchored to the investigated vesicle. The measurements were performed by using two different objectives – 40x Phase contrast and 40x DIC. As light source for fluorescence excitation the monochromator (equipped with a 150 W Xenon lamp) was used. The light was guided from the monochromator to the condenser (which focuses the excitation light on the sample) via an optical fiber.

The fluorescence detection measurements were conducted as follows. The fluorescent dye was excited by illuminating the sample with a beam with wavelength 513 nm (the excitation wavelength TOTO-1, see 2.2.3). No fluorescence was observed in the microscope oculars. It was assumed that the intensity of the emitted light was too low to be detected with a naked eye and the signal was directed to the Till-Imago CCD camera. The camera exposure time was varied in the interval 200-1000 ms. The signal from the camera was directed the frame grabber and afterwards stored in the computer memory. A typical image is shown in fig 5.1. The vesicles were visualized and located in the microchamber by using transmitted light microscopy (fig. 5.1a). Afterwards the illuminating light was blocked, and the fluorescent dye was excited at 513 nm. The recorded picture is shown in fig. 5.1b. The exact location of both vesicles is indicated with red circles. The intensity from the area, where the vesicles are seems to be higher. Because the fluorescence quantification (the number of anchored DNA per vesicle) was needed, the grayscale image shown in fig. 5.1b was binarized (converted to a black and white one). This operation was performed with the image processing software (Till Vision). The binary image is presented in fig 5.1c. The white spots correspond to the areas

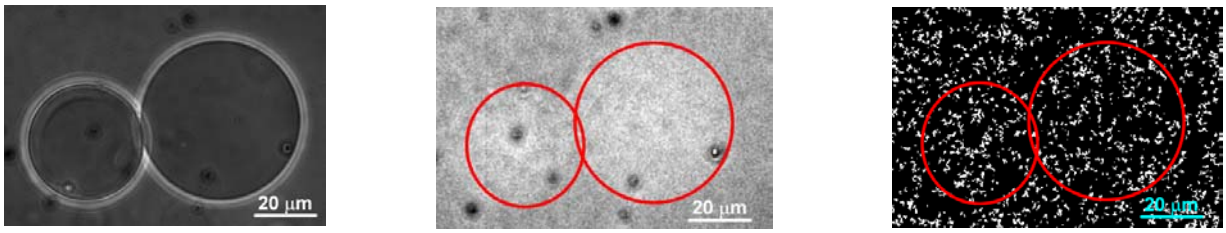

(a) **(b)** **(c)**

Fig. 5.1: Two vesicles with anchored DNA with surface concentration $0.6\Gamma^{ov}$, observed with a 40x Phase contrast objective; (a) a transmitted light observation; (b) signal detected when the fluorescent dye on the DNA molecules was excited with 513 nm wavelength beam; (c) The grayscale picture (b) is converted in a binary (black and white) one. The white spots were expected to be the signal from the anchored DNA

with the highest intensity (actually with intensity higher than a certain threshold set by the software) from fig. 5.1b (presumably DNA). The areas with intensity lower than the threshold are colored in black.

Because of the very low intensity of fluorescence emission (not visible with a naked eye) the exposure time of the camera in most experiments was set to very high values, around 1s. One may expect that when the fluorescence signal is collected for 1s, the level of the background signal (noise) will increase too (the camera cannot separate the signal (fluorescence emission) and noise and amplifies both signals). In order to probe the signal to noise ratio of the electronics (CCD camera and frame grabber) a test experiment was conducted as follows. The experimental microchamber was filled with sucrose solution only and was illuminated with 513 nm wavelength. Sequence of images was recorded and processed by following the already described procedure. In the images recorded from the sucrose solution areas with very high intensity were detected. Their number and size (area) distribution were identical to those presented in fig. 5.1 (b, c). Presumably such pseudo fluorescence was due to the amplification of the noise (as longer the exposure time, as the higher level of noise). The test demonstrated that the signal to noise level of the fluorescence microscopy equipment is very low and cannot yield reliable data about the number of anchored DNA. Thus this experimental technique was abandoned.

5.4. Fluorometry

The emission (excitation) spectrum of a fluorescently labeled sample can be measured with a fluorometer (sometimes called spectrofluorometer). It records the spectrum, which in fact represent the relative photon intensity per wavelength interval. A schematic drawing of such machine is presented in *Appendix B*. We attempted to use this technique in order to

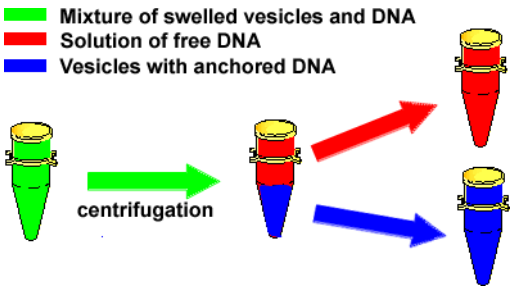

Fig. 5.2: The vesicles-DNA mixture (green vessel) is centrifuged in order to separate the vesicles with anchored polymer and the free in the bulk DNA molecules. Then the intensity from the separated solutions is measured and is compared to the one measured from the mixtures.

estimate the amount of DNA molecules anchored to GUVs. The experiments were conducted as follows. The sample was prepared as described above; the osmolarity of the sucrose solution inside the vesicle was 500 mOsm/g. A measuring cuvette was filled with 300 μl mixture of GUV (surface concentration of anchors $0.60\Gamma^{\infty v}$) and DNA. The total concentration of DNA inside the cuvette was $3\text{x}10^{-13}$ M. The intensity of the fluorescence emission I_m at 533 nm was measured. Then the vesicles-DNA mixture was centrifuged for 2 hours with a speed of 2000 rpm. Due to the relative density difference of the solutions inside/outside the vesicles (with anchored DNA), the latter should sink at the bottom of the vessel, while the free (not anchored) DNA molecules are expected to be uniformly distributed in the bulk. The vessel with the mixture was carefully (without any agitation) taken out of the centrifuge. The liquid from the upper part of the vessel (250 μl) was taken out with a pipette and added in a second vessel containing 50 μl glucose solution. In the first vessel were added 250 μl glucose. Thus both vessels were set to contain 300 μl solution, only vesicles with anchored DNA in the fist one and free DNA in the second (fig5.2). The intensity of fluorescence emission at 533 nm from both vessels was measured. Let us denote with I_v the intensity from vesicles with anchored DNA solution, with I_{DNA} the intensity from free bulk DNA and with I_m the intensity from the vesicles DNA mixture. Notice that the DNA molecules are the only fluorescently labeled component and thus the number of anchored polymers can be estimated from the intensity I_v. One can relate the intensities I_m, I_v and I_{DNA} with the equation

$$I_m = I_v + I_{DNA} \tag{5.1}$$

The experimental data showed $I_m \approx I_{DNA}$. The intensity of fluorescence emission from the DNA-decorated vesicles solution was very low, comparable with the experimental error. The latter was determined by measuring the "fluorescence" emission spectrum of the solvent. Presumably this effect (very low I_v) appears either due to the low bulk concentration of anchored DNA in the vessel or due to inappropriate centrifuging speed and diffusion do not allow the sample separation (the DNA-vesicles mixture solution has to be separated in DNA-

decorated vesicles and free in bulk DNA molecules solutions). We tried to optimize the sample separation procedures, but the result $I_m \approx I_{DNA}$ remained. It was assumed that this was due to the low bulk concentration of anchored DNA. The concentration of DNA, used in these experiments, was $3x10^{-13}$ M, which is comparable with the machine resolution. Presumably if the bulk concentration of anchored DNA is lower than 10^{-13} M, the fluorescence signal could not be detected.

This method was not used further for quantification of anchored DNA, because the machine sensitivity at very low sample concentrations was not sufficient.

5.5. Laser Scanning Confocal Microscopy

Confocal images were taken with a confocal laser-scanning system TCLS coupled to an inverted microscope Leica (Wetzlar, Germany), equipped with a 100x oil immersion objective (numerical aperture of 1.4). The fluorescent intensities (λ=488 nm) of the scanned DNA decorated vesicles were measured by using the TCLS software. A 2D image of a small partial volume of the vesicle centered at the focal plane was obtained by performing a raster sweep of the specimen in the focal plane. As the raster scans across the specimen, the analog signal from the photomultiplier is converted to digital, thus contributing a pixel-based image on a monitor, connected to the CLSM control computer. The relative intensity of the fluorescent light, emitted from the laser-hit point, corresponds to the intensity of the resulting pixel in the image. The plane of focus (z-plane) is selected by a computer controlled step motor. The latter controls the movement of the microscope stage (up and down).

To avoid the misinterpretation of the electronics noise as fluorescence emission (as in the fluorescence microscopy experiments) series of test experiments were conducted and the obtained results are summarized in Table 4. Fluorescence was observed only from samples containing fluorescently labeled DNA molecules (free in the bulk or anchored to avidin coated GUVs). The samples were prepared as described before. About 50 μl of the vesicles-DNA

Table 4

Investigated system	*Observable fluorescence*
Sucrose solution	NO
Glucose solution	NO
Non fluorescently labeled DNA	NO
Fluorescently labeled DNA	YES
Vesicles in glucose	NO
Vesicles, decorated with non-fluorescently labeled DNA	NO
Vesicles, decorated with fluorescently labeled DNA	YES

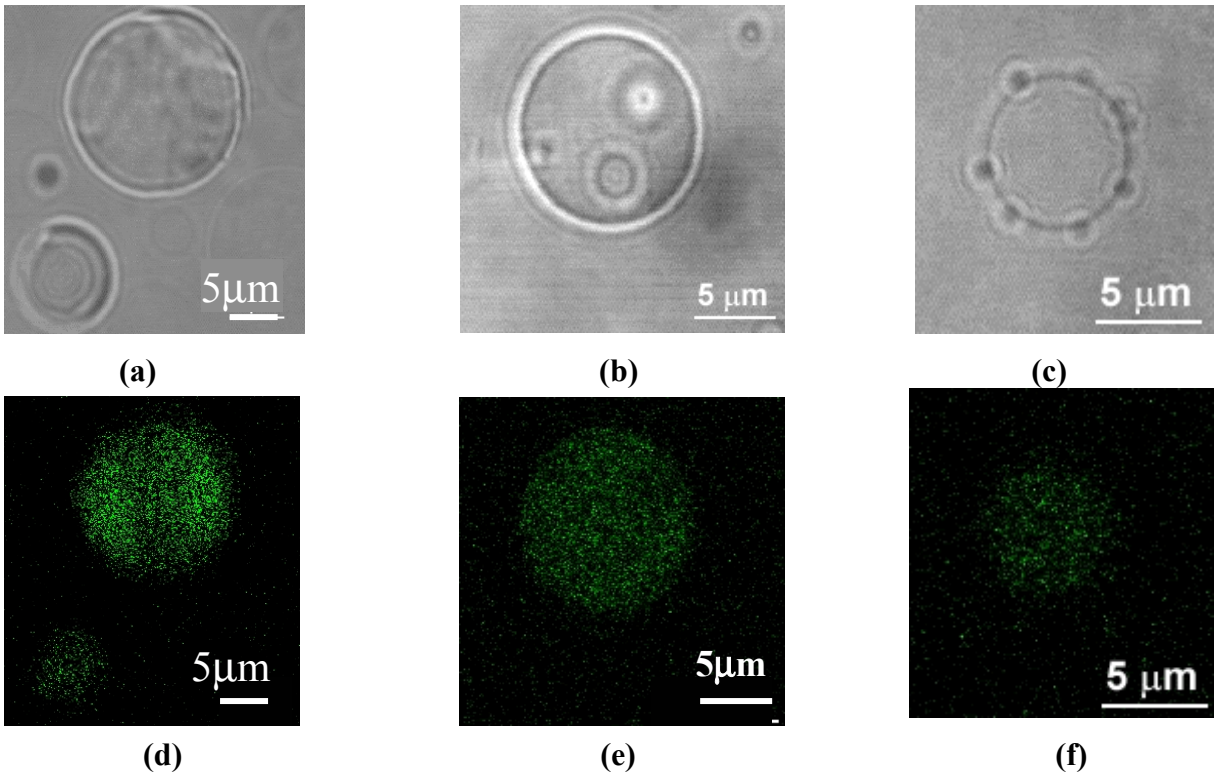

Fig. 5.3: Vesicles, decorated with anchored DNA with three virtual concentrations: $0.6\Gamma^{ov}$(a,d), $0.3\Gamma^{ov}$(b,e) and $0.12\Gamma^{ov}$(c,f). The upper images (a, b, c) represent vesicles with the corresponding surface concentration of polymer, observed in transmitted light with a 100x oil immersion objective. The bottom images (d, e, f) show the fluorescence signal from anchored DNA molecules.

mixture was enclosed between two microscope cover slides and directly observed. Experiments were conducted with all virtual surface concentrations of DNA (surface concentration of avidin anchors), investigated with fluctuation spectroscopy (see Chapter 4), namely $0.03\Gamma^{ov}$, $0.06\Gamma^{ov}$, $0.12\Gamma^{ov}$,$0.3\Gamma^{ov}$ and $0.6\Gamma^{ov}$. Detectable signal was registered only with the experiments with $0.12\Gamma^{ov}$, $0.3\Gamma^{ov}$ and $0.6\Gamma^{ov}$ (fluorescence from the anchored DNA at $0.03\Gamma^{ov}$, $0.06\Gamma^{ov}$ was not observed, presumably due to very low emission intensity) and representative images are shown in fig. 5.3. Notice the internal structures in 5.3a, the three buds in 5.3b. Presumably these morphological changes are induced by the anchored polymers. Vesicle budding for $0.3\Gamma^{ov}$ was observed in the experiments with fluctuation spectroscopy. The DNA induced spontaneous curvature was estimated from the bud size, as described in the previous chapter, M_{sp}=0.7 μm^{-1} (fig. 53b, $0.3\Gamma^{ov}$). The ring of dark spots surrounding the vesicle in fig 5.3c does not consist of buds, but of defects on the microscope cover slide below. The fluorescence images presented in the figure show higher fluorescence intensity is at the higher surface concentrations. This however does not contradict the data presented in

the previous chapter (regardless of the increased surface concentration of anchors the number for anchored DNA could be constant, corresponding to $0.12I^{\phi\nu}$), because the intensity of fluorescence emission depends strongly on the photo-bleaching (see section 3.2.4. and *Appendix B*). The observed effect may originate from different exposure times of the different vesicles during the fluorescence detection measurements.

We attempted to estimate the number of anchored DNA per vesicle by using the digital image processing algorithms described in [4]. The first step was to maximize the contrast of the image. A common technique for contrast enhancement is the combined use of the top-hat [98] and bottom-hat [99] transforms. Because both transforms are based on searching the image for patterns with particular geometry [4] and because the gyration radius of the used DNA is 0.5 μm [41], the image was scanned for circles with diameter 0.5 μm (area of about 50 pixels). The contrast was enhanced when the bottom-hat image was digitally subtracted (pixel by pixel) from the sum of the original and top-hat images. The enhanced image was processed with algorithms for edge detection. The size and the area of the detected objects were compared to the corresponding size and dimensions of a single DNA molecule.

Our attempts to determine the number of anchored DNA by the means of digital image processing did not yield reliable results. We found that the obtained data were contradictory. No correlations were found between the surface concentration of anchors and the determined number of anchored polymers. A possible reason for that is the searching pattern, required from the contrast enhancing algorithms, which scans the image for a particular structural element but the anchored DNA might have large variety of different configurations and appear in the image as objects with different and uncorrelated topologies[3].

5.6. Conclusions

In order to estimate the number of anchored DNA to a membrane with a given surface concentration of avidin anchors we used three different experimental techniques: fluorescence microscopy, fluorometry and confocal microscopy. The confocal microscopy experiments yielded qualitative information about the anchored DNA. We attempted to quantify the data and to determine the number of anchored DNA by analyzing the confocal microscopy images by the tools of digital image processing, but no quantitative data was obtained.

[3] We tried to scan the image by using different structural elements, but that did not improve the total performance of the algorithms.

Chapter 6

Summary and conclusions

6.1. Summary

The ultimate goal of this work was to conduct a systematic experimental study on the changes in the elastic properties of lipid membranes induced by anchored long polymers and to compare the experimental data with the theoretical expectations. As long polymers we used biotinylated λ-DNA molecules (see section 2.2.2), which were anchored to avidin coated DOPC/biotinyl-CAP-PE membranes via the very strong (-88 kJ/mol [44]) avidin-biotin bond. The study was conducted in the polymer mushroom regime and the working surface concentrations of anchors (virtual concentrations of anchored DNA, defined in Chapter 5) were $0.03\Gamma^{ov}$, $0.06\Gamma^{ov}$, $0.12\Gamma^{ov}$, $0.3\Gamma^{ov}$ and $0.6\Gamma^{ov}$. By employing two different experimental techniques - fluctuation spectroscopy (section 2.3.3) and fluorescence detection (section 2.3.2.4 and 2.3.2.5) - we attempted to measure the change in the membrane spontaneous curvature and to detect the effective surface concentration of anchored DNA, respectively. In Chapter 4 we presented the results of a detailed fluctuation spectroscopy study on the effect of anchored DNA on the membrane spontaneous curvature (experiments with each working surface concentration of anchors were performed). The main results were summarized in fig. 4.14. Up to $0.3\Gamma^{ov}$ the DNA induced increase in the spontaneous curvature correlates with the increase of the surface concentration of anchors. For $0.3\Gamma^{ov}$ and the higher surface concentration ($0.6\Gamma^{ov}$) of anchors the DNA induced effect is identical for both surface concentrations of anchors. Presumably this effect is due to the relatively small number of polymers, which can diffuse to the investigated vesicle (see *Appendix F* for details). The obtained results from the fluorescence measurements were presented in Chapter 5; the confocal microscopy experiments demonstrated that the DNA molecules were anchored to membranes with different surface concentration of avidin anchors, but no quantitative information about their number was obtained.

6.2. Conclusions

As described in section 1.2.2 theoretical calculations [10, 22, 26, 27] predict two limiting regimes for the membrane spontaneous curvature as a function of the polymer surface concentration: *i)* At low coverage (mushroom regime) the spontaneous curvature scales linearly with the surface density of anchored polymers (1.23) (as already mentioned, the presented data in this study concern this regime only); *ii)* At high surface concentration (brush regime) the dependence is quadratic (1.29). Experimentally we control the number of avidin anchors on the vesicle surface, which we refer as virtual concentration of anchored polymer (discussed in section 5.1). In section (1.2.2.2) we defined two different mushroom regimes, separated by the crossover surface concentration Γ^*. The latter was calculated according to equation (1.28) and it was found to be 0.136 μm^{-2}, which corresponds to $0.18\Gamma^{ov}$. Thus the DNA induced spontaneous curvature for the surface concentrations of anchors $0.03\Gamma^{ov}$, $0.06\Gamma^{ov}$ and $0.12\Gamma^{ov}$ is predicted by equation (1.23) and (1.26) (mushroom regime 1). For $0.3\Gamma^{ov}$ and $0.6\Gamma^{ov}$ the different contributions to the DNA induced spontaneous curvature are calculated from equation (1.23), (1.26) and (1.27) (mushroom regime 2).

As one may expect it is possible that in the experiments not every avidin anchor on the vesicle surface is occupied. This situation was discussed in section 5.1, where the actual surface concentration was defined as the effective surface coverage of anchored DNA at a given surface density of avidin anchors. As discussed in Chapter 5, our attempts to determine the actual surface concentration of anchored polymers by fluorescence were not successful due to low fluorescence intensity. The spontaneous curvature data (obtained from fluctuation analysis and bud analysis data, Chapter 4) indicate that for the surface concentration of anchors, higher than $0.3\Gamma^{ov}$ the change in the spontaneous curvature is identical. Presumably this is due to identical actual surface concentrations of DNA, although the surface concentrations of anchors (virtual polymer coverage) are different.

In section 4.5 we demonstrated that in the cases of budding (an effect arising from the anchored polymers), the DNA induced spontaneous curvature can be determined from the size of the buds. This curvature is absolute (unlike the one obtained from the fluctuations spectroscopy, which is proportional to the absolute one, see section 4.4.1). The averaged value for DNA induced spontaneous curvature was obtained from the bud analysis of all experiments conducted with surface concentration of anchors $0.3\Gamma^{ov}$ and $0.6\Gamma^{ov}$ (the DNA induced spontaneous curvatures in the experiment with these surface concentrations of anchors are identical, see fig. 4.14) it was found to be M_{sp} =1.05 ±0.02 μm^{-1}.

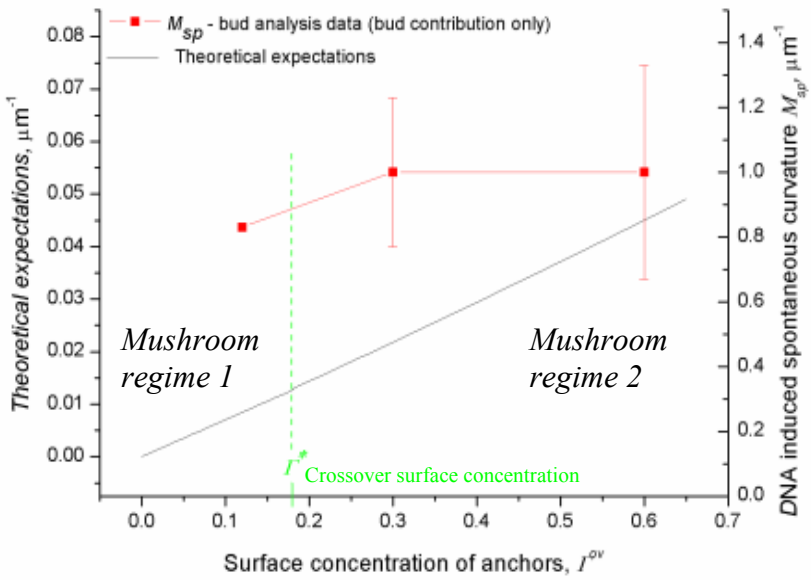

Fig. 6.1: Spontaneous curvature induced in lipid membranes by anchored DNA in mushroom regime – comparison of the experimentally obtained data and the theoretical expectations. Both mushroom regimes (1 and 2) are separated by the crossover concentration Γ^*. The fluctuation spectroscopy data (in mushroom regime 1) is not shown

Fig. 6.1 presents a comparison of the experimentally obtained spontaneous curvature with the theoretical expectations. The latter were calculated by using equation (1.23), (1.26) and (1.27) (the end to end distance of the polymer was calculated from equation (1.16) with number of statistically independent segments N=170 and persistence length a_p=50 nm [63], because the bending rigidity of the membranes we used was not known, a typical phospholipid membranes κ=20 K_BT was taken, but the membrane could be stiffer due to the presence of avidin). As explained in chapter 4, the data obtained from the fluctuation spectroscopy is proportional to the real spontaneous curvature and cannot be directly compared with the theoretically obtained spontaneous curvature. But qualitative comparison is possible. Notice the linear increase in the spontaneous curvature with the increase in the surface concentration for mushroom regime 1 ($0.03\Gamma^{ov}$, $0.06\Gamma^{ov}$ and $0.12\Gamma^{ov}$) presented in fig. 4.14 (experimental data) and fig. 6.1 (theoretical expectations). The slopes are different, but the theoretical curve was obtained by using a typical value of 20 K_BT for the membrane bending stiffness. The actual bending stiffness is to be obtained by performing a numerical MC quantification of the experimental data (see section 2.3.3 for details).

For the experiments conducted with surface concentrations of anchors $0.03\Gamma^{ov}$, $0.06\Gamma^{ov}$ and $0.12\Gamma^{ov}$, the DNA in the bulk is in excess and one can assume that every avidin on the vesicle surface binds a DNA. If the surface concentration of anchors is higher than $0.12\Gamma^{ov}$ the anchors are in excess and regardless of the increased number of anchors (virtual concentration

of DNA, see Chapter 5), the actual surface concentration of DNA does not change significantly. Thus the DNA induced spontaneous curvature obtained from the bud analysis (within the experimental error) is identical for $0.3\Gamma^{\infty v}$ and $0.6\Gamma^{\infty v}$. As discussed before, this spontaneous curvature is absolute and can be compared with the theoretically calculated one. As seen from fig. 6.1, there is a big discrepancy between the experimental data and theoretical expectations. It can appear due to

1. Incorrect value of the bending stiffness (see the above discussion)
2. When the DNA induced spontaneous curvature was estimated from the size of the bud (equation 4.3) it was assumed that the membrane composition was homogeneous. But if the number of anchors on the bud surface is relatively large this assumption may not be correct and the estimated value of the spontaneous curvature might be wrong.

The exact reason for this discrepancy in not known. It is a subject of a further study.

6.3. Perspectives

The case with excess of DNA relative to the surface concentration of avidin (at $0.03\Gamma^{\infty v}$ and $0.06\Gamma^{\infty v}$) was studied with fluctuation spectroscopy. An increase in the membrane spontaneous curvature with the increase the number of surface anchors was detected. These data are to be quantified with Monte Carlo simulations (see section 2.3.3 for details) and the absolute values of the DNA induced spontaneous curvature and the membrane bending stiffness are to be obtained. When the membrane bending stiffness is known, the only undetermined parameter remains the exact surface concentration of anchored polymers. The unknown polymer surface coverage can be used as a fitting parameter in equation (1.23), (1.26) and (1.27) and the theoretical increase in the spontaneous curvature could be compared with the experimentally measured changes.

The discrepancy between the bud analysis data and the theoretical expectations is also a subject of further investigations.

Appendix A

Avidin binding site (ABS)

Avidin is a tetrameric protein. It is built of four subunits, each containing 128 amino acid residues [46]. The subunits however have different amino acid compositions. In fig. A.1 is shown the residues and the hydrogen bonds involved in an ABS-biotin for the subunit labeled as B in [46, 96, 97]. The picture was taken from [96]. The 3D structure of this subunit is available in [97]

Hydrophobic residues in ABS

These include Trp-70, Phe-72, Phe-79 (not shown in fig. A.1) and Trp-97 from one monomer and Trp-110 (not shown in fig. A.1), which is provided by the adjacent symmetry –related monomer [48].

Hydrophilic interactions in the ABS

Ureido oxygen on of the biotin molecule forms three hydrogen bonds with the side chains of Asn-12, Ser-16, and Tyr-33 of avidin, forming a tetrahedral oxyanion. In addition, each of the two ureido nitrogens participates in single hydrogen bonds. One interacts with the main chain N¨H of Ala-39 and Thr-40 as well as the side chain of Thr-38 (these residues are part of the loop that is stabilized when biotin is bound), and the other forms hydrogen bonds with the side chains of Ser-73 and Ser-75 [48].

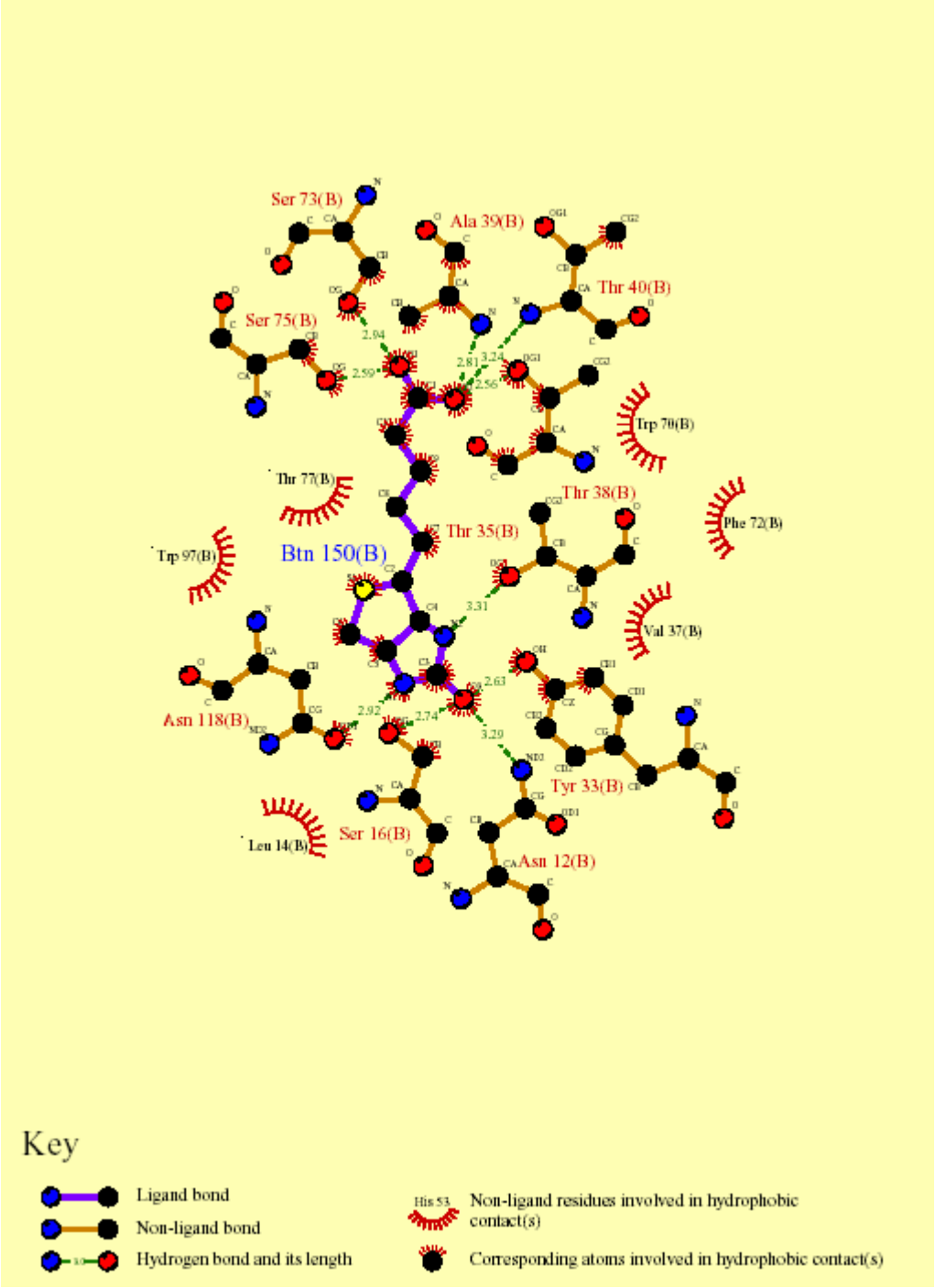

Fig A.1: Binding site of avidin (ABS) (chain B, [46, 96, 97]).

`

Appendix B

Fluorescence – physical principles and detection

Fluorescence belongs to a group of phenomena, unified with the common name luminescence. They occur when susceptible molecules emit light from electronically excited states created by a physical (for example, absorption of light), mechanical (friction), or chemical mechanism. Generation of luminescence through excitation of a molecule by ultraviolet or visible light photons is a phenomenon called photoluminescence, which is formally divided into two categories, fluorescence and phosphorescence, depending upon the electronic configuration of the excited state and the emission pathways.

The electronic state with lowest energy is referred as ground state. Every state with higher energy is known as an excited state. At room temperature the number of atoms in excited state is negligibly small and therefore the majority of molecules are in the ground state. A further characteristic of the electronic state is its multiplicity. The spin quantum number (S) of the molecule is the absolute value of the sum of the electronic within the molecule. The multiplicity of a molecule is defined as (2S+1) and it can be either singlet state (S=0) or triplet state (S=2). For the same electro configuration the triplet states always have higher energy than the singlet ones, e.g. T_1 has lower energy that S_1. Therefore, usually, the excited state with lowest energy is a triplet state (fig B.1).

When a molecule, residing in the ground state (with energy E_0) adsorbs a photon with energy $E_A=h\nu_A$, it jumps to an excited state. The molecule has several ways to return to the state with lowest energy (fig B.1) and there is a certain probability for each of them. In the case of fluorescence the emitted photon (F) has less energy ($E_F=h\nu_F$) than the excitation photon (A). Therefore the wavelength of the emission is longer than the excitation - Stokes' law. In the particular case in which the excited electron is initially in not in its ground state, the energy of emission can be higher than that of excitation.

The characteristic spectra of fluorescence are adsorption (excitation) spectrum and emission spectrum. The excitation spectrum is a plot of the excitation wavelength versus the total intensity of the emitted fluorescence. The emission spectrum is a plot of the relative intensity of the emitted radiation at each wavelength. (see section 2.2.3)

The excited molecules can return to the state with lowest energy by following different mechanisms:

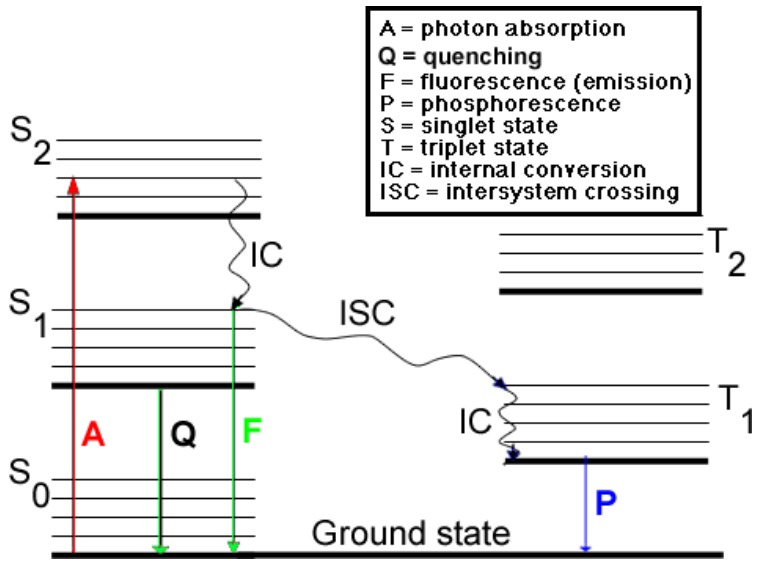

Fig. B.1: Molecular energy levels: singlet and triplet electronic states and the different mechanisms for relaxation from an excited state to the state with lowest energy (Jablonski diagram). The rotational energy levels and vibrational relaxation transition are not shown.

- *Fluorescence* is a transition from an exited singlet to ground state. Due to the very short excited state lifetime, the decay time of fluorescence is approximately 10^{-9} to 10^{-8}s

- *Internal conversion* (IC) is a transition from low vibrational level of an excited state to a high vibrational level of lower excited state without emitting radiation. Since the energies of S_2 and S_1 are very close, the transition probability is high and usually the transitions last less than 10^{-11} s.

- *Intersystem crossing* (ISC) is a non radiative process and occurs when a molecule in an excited singlet state converts to an excited triplet. This process is usually followed, by vibrational relaxation, where the molecule falls to the lowest energy level of the excited triplet state.

- *Phosphorescence* is the returning to ground state from triplet state by emission of a photon. The lifetime of excited triplet state is in the range 10^{-4}-1 s, and therefore phosphorescence decay is much longer than that of fluorescence. The energy of a triplet state is generally lower than the one of the corresponding singlet state, e.g. T_1 is at lower level than S_1. It follows that the wavelength of phosphorescence is generally longer that that of fluorescence.

- *Vibrational relaxation* is the most common of the three non radiative transitions, occurs very quickly (10^{-12} seconds) and is enhanced by physical contact of an excited molecule with other particles to which energy, in the form of vibrations and rotations, can be transferred through collisions (not shown in fig. B.1)

The excitation and emission spectra can be measured with a fluorometer (sometimes called spectrofluorometer) (fig. B.2). It records the excitation and emission spectra of the

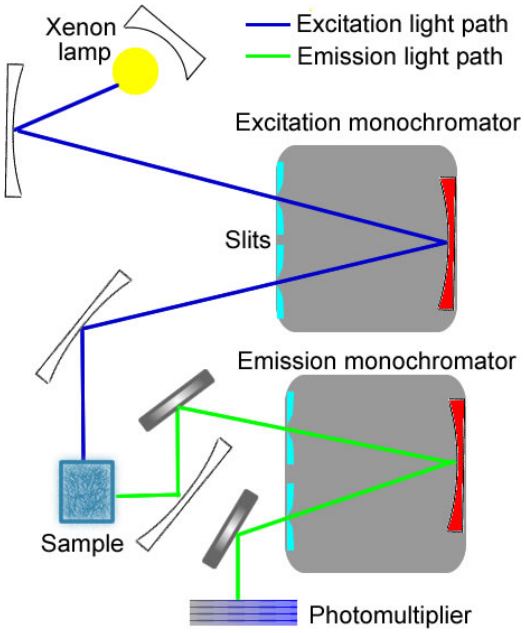

Fig. B.2: The optical paths in a typical fluorometer

fluorescing sample, which represent the relative photon intensity per wavelength interval. The light, emitted from a xenon lamp, is directed onto a monochromator grating. The grating splits the light up into its rainbow colors. The slits allow only a narrow band of light to pass through. This band of approximately monochromatic light is then focused onto the sample. Light emitted from the sample is collimated and directed into the emission monochromator. Built similar to the excitation monochromator, it lets only a narrow band of wavelengths to pass. A photomultiplier collects the light and measures its intensity.

Appendix C

Available for binding biotin on the vesicle surface

In this Appendix we show that, due to the very high surface concentration of biotin in the ITC experiments with 10 mM extruded vesicles (DOPC/biotinyl-(CAP)-PE 10:1) not every biotin can be bound to an avidin binding site (ABS). This is true for all investigated systems: excess of avidin, intermediate case and large excess of biotin, see section 3.1).
Let us consider a spherical vesicle and introduce the following notation:
N_b^t -the total number of biotin on the outer vesicle surface (the bulk concentration of these lipids in the ITC measuring cell was defined in equation 3.3)
N_b^B -the number of bound biotins on the vesicle surface if the latter is densely covered with avidin
R_{ves} -vesicle radius
S_{lip} -area per lipid headgroup (S_{lip} =0.7 nm, [31])
S_{av} -area of the vesicle surface covered by an avidin molecule
Let us calculate N_b^t and N_b^B :

$$N_b^t = 0.1\frac{4\pi R_{ves}^2}{S_{lip}} \qquad \text{C.1a}$$

$$N_b^B = 2\frac{4\pi R_{ves}^2}{S_{av}} \qquad \text{C.1b}$$

The factor 0.1 in (C.1a) reflects the fact that the molar fraction of the biotinylated lipid is 10 percent of the total amount of lipid in the vesicle. The factor 2 in (C.1b) sets the maximal number of biotin from the membrane, which can be bound to one avidin molecule (see section 2.1.2 for details). By taking the ratio of (C.1a) and (C.1b) one finds:

$$\frac{N_b^B}{N_b^t} = \frac{2S_{lip}}{0.1S_{av}} \approx 0.6 \qquad \text{(C.2)}$$

(C.2) shows that even if the entire vesicle is densely covered with avidin, only the maximal molar fraction of bound membrane biotin is only 0.6. The remaining biotin groups on the surface remain unbound. This result is universal for every vesicle, because it does not depend on the vesicle radius.

Appendix D

Enlarged bud images

Due to the limited space all vesicle images, shown in Chapter 4 were drastically shrunk (down to about 20% of the original size). The latter however makes it very difficult (even impossible) to visualize the vesicle buds. The same images (80% of the original size) are shown in this appendix.

1. Surface concentration 0.12$\Gamma^{\infty v}$

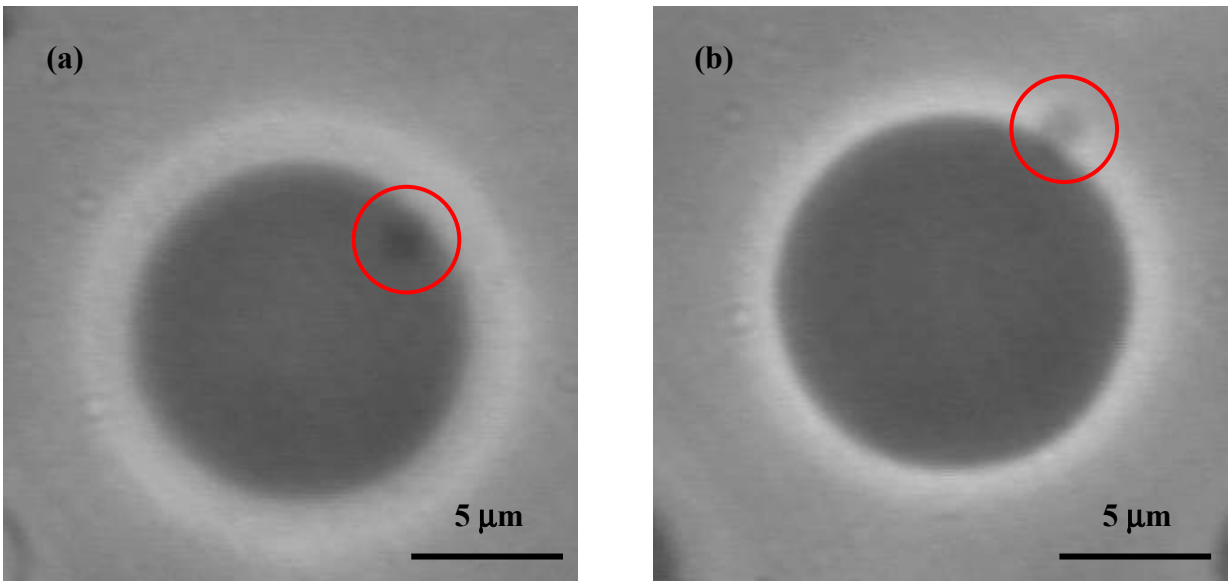

Fig D.1: (a) image shown in fig 4.9d; (b) this image was taken 2 min after image (a) and is not shown in Chapter 4. The bud location is indicated with red circles.

2. Surface concentration 0.3$\Gamma^{\infty v}$

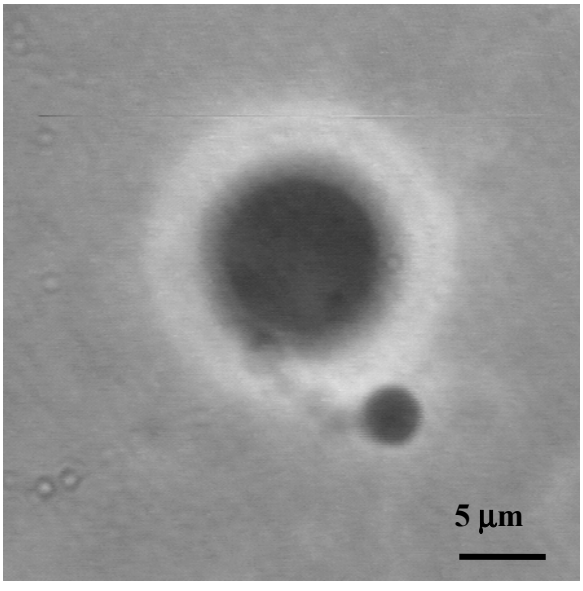

Fig D.2: This image is shown in fig.4.10d. The bud is clearly visible. It is connected to the "mother" vesicle by a pearl of small vesicles of approximately equal size. (about 1.4 µm). A possible interpretation of this event would be that each of the vesicles-pearls has one or several anchored polymers (each pearl should have about four anchors).

3. Surface concentration $0.6\Gamma^{\infty v}$

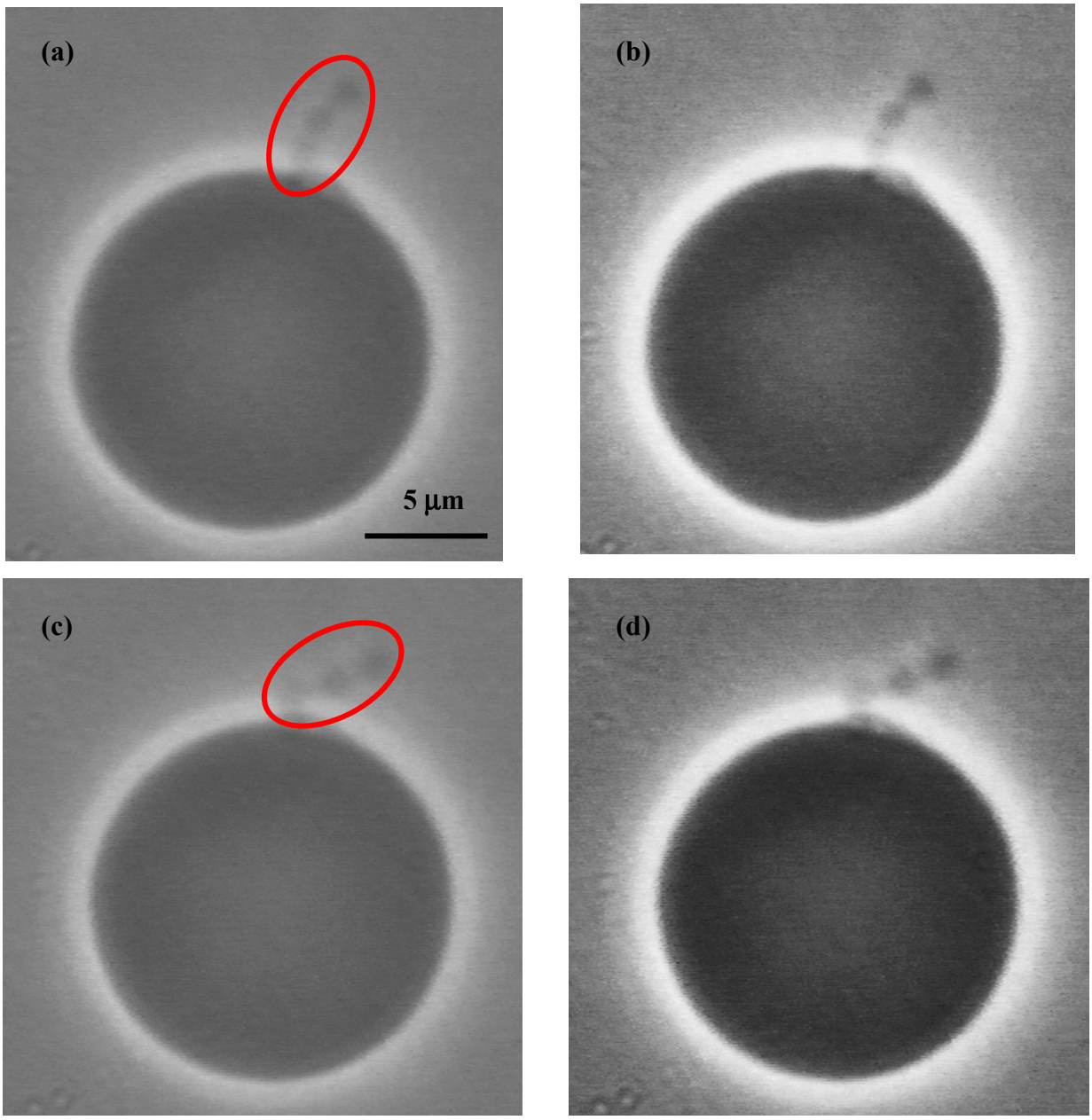

Fig D.4: Image (a) is shown in fig 4.13 (image B). The bud consists of three interconnected spherical vesicles with identical sizes (about 1.4 µm). The bud location is encircled in a red ellipse; (b) the contrast of image (a) is enhanced in order to visualize the bud; (c) this image is not shown in Chapter 4. It was made 15 min after image (a). The red ellipse again indicates the bud location; (d) the contrast of (c) is enhanced in order to visualize the bud.

Appendix E

Fluorescence microscopy equipment

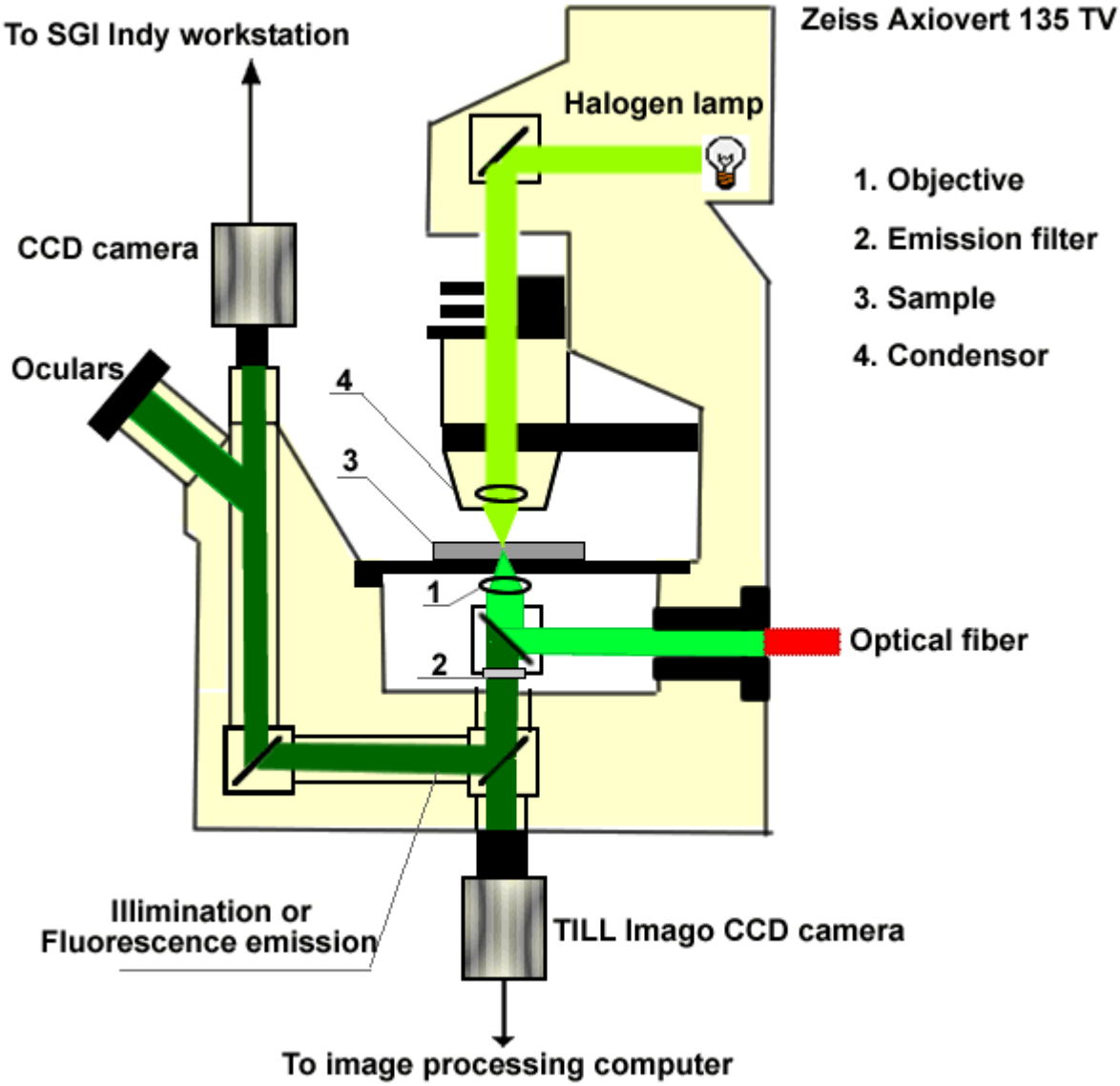

The main parts and the light paths in an inverted optical microscope (Zeiss Axiovert 135 TV), equipped with fluorescence microscopy camera (Till Imago CCD camera), optical fiber connected to a monochromator (nor shown), frame grabber (not shown) and image processing computer (not shown). When the objective is focuses on the sample, the observed in the oculars images can be directed either to the CCD camera or to the TILL Imago Camera. By changing the illumination from the halogen lamp with the beam from the optical fiber one may observe fluorescence from the sample. The images are grabbed and stored in the memory of the image processing computer (as described in section 5.3).

Appendix F

DNA diffusion in the flow chamber

When flushed inside the flow chamber, the DNA molecules need certain time to diffuse to the vicinity of the investigated vesicle. This process however is relatively slow, because the low diffusion coefficient of the DNA molecules (0.47±0.03 $\mu m^2/s$, [61]). In this appendix we estimate the number of polymers which can approach the vesicle by diffusion within one hour (the averaged time to observe effect on the spontaneous curvature after flushing DNA). Within this period a DNA molecule can sweep (in either vertical or horizontal direction) area of approximately A_0=1700 μm^2. If the investigated vesicle lies on the bottom of the flow chamber in the middle of a square with such area ($A_0=a^2$, where a is the side length of the square), it can be approached by DNA molecules from the neighboring squares. Thus the total area around the vesicle the DNA molecules can sweep, before getting anchored is $A=4a^2$. Let consider a virtual parallelepiped, surrounding the vesicle and the latter lies in the middle of its bottom. The horizontal side lengths are $2a$ (reflecting lateral polymer diffusion from the neighboring virtual parallelepipeds), while the vertical ones are with length a (because the vesicle lies on the bottom of the chamber, there are no neighboring parallelepipeds from below) (see fig. F.1); the volume of such parallelepiped is $1.4.10^{-4}$ µl. Because the total volume of the experimental cell is about 500 µl, the number of such virtual parallelepiped inside is 4.10^6. The typical concentration of DNA inside the flow chamber is 3.10^{-13} M, which corresponds to about 10^8 molecules in the chamber. Thus the number if a DNA molecule, residing in the imaginary parallelepiped, is approximately 30. Thus within one hour, after DNA is flushed in the flowing chamber, the estimated number of DNA molecules which can diffuse (and presumably anchor) to the vesicle is 30. This estimation is correct only if the DNA molecules are uniformly distributed inside the bulk.

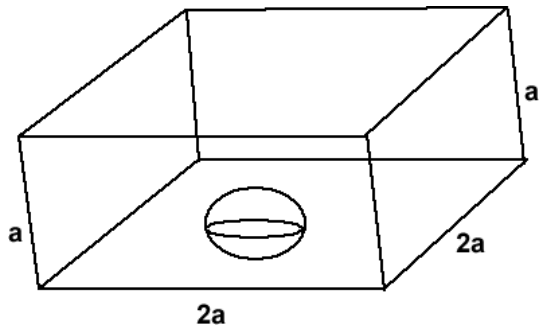

Fig. F.1: A vesicle, lying on the bottom of the experimental cell. Presumably within one hour after DNA is introduced in the cell, only DNA molecules, from the sketched virtual parallelepiped can diffuse and bind to the vesicle (see the text for details)

Glossary

ABS = Avidin Binding Site

ADE = Area Difference Elasticity model

biotinyl-DOPE = 1, 2-Dioleoyl-*sn*-Glycero-3-Phosphoethanolamine-N-Biotinyl, 18:1

biotinyl-CAP-PE =1, 2-Dioleoyl-*sn*-Glycero-3-Phosphoethanolamine-N-Cap Biotinyl

CLT = Central limit theorem

DLS = Dynamic Light Scattering

DSC = Differential Scanning Calorimetry

DOPC = 1, 2-Dioleoyl-*sn*-Glycero-3-Phosphocholine, 18:1

FJC = Freely jointed chain

GFP = Green Fluorescent Protein

GUVs = Giant Unilamellar Vesicles

ITC = Isothermal Titrational Calorimetry

LSCM = Laser Scanning Confocal Microscope

LUVs = Large Unilamellar Vesicles

MC = Monte Carlo Simulations

TOTO-1 = fluorescent dye

References

1. Donald D. Voet, Judith G. Voet, *Biochemistry*, Wiley, second edition, 1995
2. James Darnell, Harvey Lodish, David Baltimore, *Molecular Cell Biology*, Scientific American Books, second edition, 1990
3. Pier Luigi Luisi and Peter Walde, *Giant Vesicles. Perspectives in Supramolecular Chemistry*, John Wiley & sons Ltd, 1999
4. Rafael C. Gonzales, Richard E. Woods, Digital image processing, Prentis Hall, 2002
5. C. Ladavière, M. Toustou, T.Gulik-Krzywicki and C. Tribet, *Journal of Colloind and Interface Science*, **241**, 2001, 178-187
6. Robert G. Gennis, *Biomembranes. Molecular structure and function*, Springer-Verlag, 1989
7. Structure and Dynamics of Membranes, Editors R. Lipowsky and E. Sackmann, Elsevier, 1995
8. Theodore Frankel, *The Geometry of Physics. An introduction*, Cambridge University Press, 1997
9. W. Helfrich, *Z. Naturforsch., **28**, 693-703,* 1973
10. R. Lipowsky, *Europhys. Lett. **30 (4)** , 197–202,* 1995
11. H.-G. Döbereiner, PhD thesis, Simon Fraiser University, Canada, 1995 (unpublished)
12. Ling Miao, Udo Seifert, Michael Wortis, H.-G. Döbereiner, *Physical Review E, **49(6)**, 5389-5407,* 1994
13. H.-G. Döbereiner, *Habilitation Thesis,* Universität Potsdam, 1999
14. J. Dhont, G. Gompper, D. Richter, *Lecture manuscripts of the 33th IFF winter school*, 04-15 March 2002, Forschungszentrum Jülich GmbH
15. Gert Strobl, The physics of polymers, 2nd edition, Springer, 1996/1997
16. C. Rutkowski, L. Williams, T. Haines, H. Cummins, *Biochemistry*, **30**, 5688-5696, 1991
17. Reinhard Lipowsky, Colloids and Interfaces A, 1997, **128,** 255-264
18. J. Simon, M. Kühner, H. Ringsdorf, E. Sackmann, *Chem. Phys. Lipids, **76**, 241-258-132,* 1995
19. G. Decher, E. Kuchinka, H. Ringsdorf, J. Venzmer, D. Bitter-Suermann, C. Weisgerber, *Die Angewandte Chemie, **166/167**, 71-80 (2768),* 1989
20. H.-G Döbereiner, A. Lehmann, O. Selchow, R. Lipowsky*, Materials Science of the Cell*, MRS Vol. 489 (Material Research Society, Warrendale 1998).
21. R. Lipowsky, H.-G Döbereiner, C. Hiergeist, V. Indrani, *Physica A, **249,** 536-543, 1998*
22. C. Hiergeist, R. Lipowsky, *J. Phys. II France, **6,** 1465-1481, 1996*
23. Y. W. Kim and W. Sung, *Europhys. Lett., **47*** **(3)***, 293-297, 1999*
24. A. Nicolas and B. Foucarde, *Eur. Phys. J. E, **10**, 355-367, 2003*
25. Landau L. D., Lifschitz E. M., Elastiztätsheorie, Akademie Verlag, 1991
26. M. Breidenich, R. R. Netz and R. Lipowsky, Europhys. Lett., **49(4)**, 2000, 431-437
27. M. Breidenich, PhD Thesis, Potsdam university, 2000
28. T. Bickel, C. M. Marques, *Eur. Phys. J. E., 2002, DOI 10.1140/epje/i2001-10113-8*
29. Kalina Hristova and David Needham, *Journal of Colloid and Interface Science, **168**, 302-314 (1994)*
30. The polymer mushroom should influence membrane properties on area of size the cross section of polymer coil. The resulting effective elastic constants are therefore valid on lengthscale comparable to the linear size opo polymer mushroom [22]
31. Jacob Israelachvil, *Intermolecular & surface forces*, Academic Press, 1992
32. J. Pencer, G. White and R. Hallett, *Biophys. J.* **81**, 2716-2728, 2001
33. M. Webb, S. W. Hui, P. Steponkus, *Biochimica et Biophysica Acta, **1145**, 93-104, 1993*

34. J. Pencer, R. Dimova, R. Lipowski, Effects of Cholesterol on Thermo mechanical Properties of Large Unilamellar Vesicles. Biophysical Society Meeting, San Antonio, Februrary 2003
35. J. Lee, P. G. Petrov, and H.-G. Döbereiner, *Curvature of Zwitterionic Membranes in Transversal pH Gradients*, Langmuir **15**:8543, 1999. J. Lee, P. G. Petrov, and H.-G. Döbereiner, *Curvature of Zwitterionic Membranes in Transversal pH Gradients*, Langmuir **15**:8543, 1999.
36. R. Lipowsky and H.-G. Döbereiner, *Europhysics Letters*, **43**, 1998, 219-225
37. H.P Duwe, J. Kas and E. Sackmann, *J. Phys. France*, **51**, 945-962, 1990
38. P Meleard, C Gerbeaud, T Pott, L Fernandez-Puente, I Bivas, MD Mitov, J Dufourcq and P Bothorel, *Biophysical Journal*, **72**, 2616-2629, 1997
39. R. Dimova, C. Dietrich, A. Hadjiisky, K. Danov and B. Pouligny, *Eur. Phys. J. B*, **12**, 589-598, 1999
40. F. Sanger, A. R. Coulson, G. F. Hong, D. F. Hill and G. B. Petersen, *J. Mol. Biol*., **162**, 729-773, 1982
41. R.Verma,J. Crocker, T. Lubensky and A. Yodh, *Phys. Rev. Lett*., **81(18),** 4004-4007, 1998
42. Lewis, R.; Sykes, B.; McElhaney, R, *Biochemistry*, **27**, 1988, 880-887
43. Author(s): Webb, M.; Hui, S.; Steponkus, P., *Biochimica et Biophysica Acta*, **1145**, 1993, 93-104
44. Green, M., *Adv. Protein Chemistry*, **29**, 1975, 85-133
45. Woolley, D. E., and Longsworth, L. G., *J. Biol. Chem*., 142, 285, 1942
46. Pugliese, L., Coda, A., Malcovati, M., Bolognesi, M, *J Mol Biol*, **231**, pp. 698 (1993)
47. Eakin, R. E., Snell E. E., and Williams R. J., *J. Biol. Chem*, **140**, 535, 1941
48. Livnah O., Bayer E., Wilchek M., and Sussman J., *Proc. Natl. Acad. Sci. USA*, **90**, 5076-5080, 1993
49. Donovan, J. W. and Ross K. D.,*Biochemistry*, **12**, 512-517, 1973
50. Green, N. M., *Biochem J*., **89**, 609-620, 1963
51. Pasut Ratanabanangkoon, Michael Gropper, Rudolf Merkel, Erich Sackmann and Alice P. Gast, *Langmuir*, **18**, 2002, 4270-4276
52. Weber, R. E., *J. Appl. Physical*., **72 (4)**, 1611 (1992)
53. Kragh-Hansen, U. and Vorum, H., *Clin. Chem*., **39 (2)**, 202 (1993).
54. Uria - Nickelsen, M.R., Leadbetter, E.R. and Godchaux, W.D., *J-Gen. Microbiol*., **139(2)**, 203 (1993)
55. R. Lipowsky, *J. Phys. II France*, 2, 1825-1840, 1992
56. Anne Ertel, Alejandro Marangoni, Jackie Marsh, F. Ross Hallet, Janet Wood, *Biophys. J*, **64**, 426-434, 1993
57. D. Needham, T. McIntosh, E. Evans, **27**, 4668-4673, 1988
58. Bürk Schäfer, PhD-thesis, Friedrich-Schiller-Universität Jena, 2001
59. X. Yan, W. Kevin Grace, Thomas M. Yoshida, R. Habbersett, N. Velppapan, James H. Jett, R. E. Keller and B. Morrone, *Anal. Chem*., **71**, 5470-5480, 1999
60. Jason Bordelon, Karl Feierabend, Shabana Siddiqui, Laura Wright, and Jeffrey Petty, *J. Phys. Chem. B*, **106**, 4838-4843, 202
61. D. Smith, T. Perkins and Steven Chu, *Macromolecules*, **29**, 1372-1373, 1996
62. Steven Smith, Laura Finzi, Carlos Bustamante, *Science*, **258(5085)**, 1122-1126, 1992
63. Claudio Rivetti, Martin Guthold and Carlos Bustamante, *J. Mol. Biol*., **264**, 919-932, 1996
64. Molecular probes online handbook, http://www.probes.com
65. H. Heerklotz, J. Seelig, *Biochimica and Biophysica Acta, **1508**, 2000, 69-85*
66. VP-ITC Microcalorimeter manual, version , MicroCal, MA, USA
67. Maskymilian Pluta, Advanced light microscopy, vol 2, Elsevier 1989
68. Online course of optical microscopy, http://microscopy.fsu.edu

69. Trask, B.J., *Trends in Genetics*, **7(5)**, 149-154, 1991
70. Prasher, D. C., Eckenrode, V., Ward W., Prendergast F., Cormier M., *Gene*, **111 (2)**,1992, 229-233
71. Mats GL Gustafsson, *Curr Opin Struct Biol*. 1999 Oct; **9(5)**: 627-34.
72. Bo, L., Waugh, R. E., *Biophys. J*., 1989, **55**, 509-517
73. Kummrow, M., Helfrich, W., *Phys. Rev. A*, **44**, 8356-8360, 1991
74. Servuss, R. M., Harbich, W., Helfrich, W., *Biochim. Biophys. Acta*, 1976, **436**, 900-903
75. E. Evans and W. Ravitz, *Phys Rev. Lett*, **64**, 2094, 1990
76. G. Gommper, H. Endo, M. Mihailescu, J. Allgaier, M. Monkenbuch, D. Richter, B. Jakobs, T. Sottmann, R. Strey, *Europhysics Letters, **58(5)**, 683-689, 2001*
77. B. M. Discher, Y.-Y. Won, D. S. Ege, J. C-M. Lee, F. S. Bates, D. E. Discher, and D. A. Hammer, Science **284**, 1143 (1999).
78. A. Petrelli, G. F. Gilestro, S. Lanzardo, P. M. Comoglio, N. Migone, and S. Giordano, Nature (London) **416**, 187 (2002).
79. H.-G Döbereiner, E. Evans, M. Kraus, U. Seifert and M. Wortis, Physical Review E 1997, **55(4),** 4458-4474
80. Hans-Gunther Dobereiner,Gerhard Gompper, Christopher K. Haluska,Daniel M. Kroll, Peter G. Petrov and Karin A. Riske, *Phys. Rev. Lett*., **91 (4)**, 2003
81. The picture was kindly provided by Dr. Rumiana Dimova
82. SA Darst, M Ahlers, PH Meller, EW Kubalek, R Blankenburg, HO Ribi, H Ringsdorf, and RD Kornberg, Biophys. J. 1991 **59**: 409-418
83. Martin Gonzales, Luis A. Bagatolli**,** Izaskun Echabe, Jose L. Arrondo, Carlos E. Argaraña, Charles R. Cantor and Gerardo D. Fidelio, *The Journal of Biological Chemistry, **272(17)**, 11288-11294, 1997*
84. Gil U Lee. David A. Kidwell and Richard J. Colton, *Langmuir,* 1994, **10**, 354-357
85. Doris A. Noppl-Simson and David Needham, Biophys. J. 1996, **70,** 1391-1401
86. Hong Qin, Zheng Liu, Sen-fang Sui, Biophys. J. 1995 **68,** 2493-2496
87. J. Lee, P. G. Petrov, and H.-G. Dobereiner, *Langmuir*, **15**, 8543, 1999
88. H. Launer, H. Fraenkel-Conrat, *J. Biol. Chem.,**193**, 125-132, 1951*
89. A private conversation with Andreas Erbe and Dr. Jeremy Pencer
90. Bang Laboratories Inc., 9525 Technology Drive, Fishers, IN 4638-2886, USA, Inventory number L001003H
91. The overlapping concentration for λ- DNA can be calculated from the definition in reference [22, 26, 108]. The polymer persistence length and number of statistically independent segments are a_p=50 *nm* [63] and N=170 [110] respectively. Thus

$$\Gamma^{ov} = \frac{1}{\pi R_p^2} = \frac{1}{\pi\left(2*0.05\sqrt{170}\right)^2} \approx 0.75\mu m^{-2}$$

92. Let us assume that the coefficient of proportionality in (2.5) is the same for every measurement within the same experiment. Then if with *i* we denote the initial state (e.g. before flushing DNA) and with *f* – the final state (e.g. the equilibrium after flushing DNA), the change in the slope can be estimated from

$$\kappa_f = \frac{\left\langle a_n^2 \right\rangle_i}{\left\langle a_n^2 \right\rangle_f} \kappa_i$$

93. J. Simon, M. Kühner, H. Ringsdorf, E. Sackmann, *Chem. Phys. Lipids, **76**, 241-258-132, 1995*
94. Seifert U., Berndl K., Lipowsky R., *Phys. Rev. A,* **44**, 1182–1202 (1991)
95. Several combinations of vesicle solutions with different concentrations (1 *mM,* 5 *mM*, 7 *mM*, 10 *mM* and 40 *mM*) and different DOPC/biotinylated lipid molar ratio (10^7:1, 10^4:1, 100:1, 10:1, 1:1) were considered and tested experimentally. The system 10 *mM* solutions and molar ratio 10:1 was found to be the best compromise between measurable signal (set by ITC machine resolution) and lipid composition. The smaller the amount of biotinylated lipid, the closer to the vesicle composition, used in the fluctuation spectroscopy experiments (10^6-10^7:1) the system will be. The upper limit of the amount of biotinylated lipid in the membranes was set by considerations of possible phase separation.
96. PDBSum database (a database of the known 3D structures of proteins and nucleic acids), code 1AVD, URL: http://www.biochem.ucl.ac.uk/bsm/pdbsum/1avd/main.html
97. CATH protein structure classification database, code 1avdB0, URL: http://www.biochem.ucl.ac.uk/bsm/cath/
98. The top-hat transform is defined as the difference between the original image and its opening. The opening of an image is the collection of foreground parts of an image that fit a particular structuring element [4]
99. The bottom-hat transform is defined as the difference between the closing of the original image and the original image. The closing of an image is the collection of background parts of an image that fit a particular structuring element [4].
100. E. Evans, D. Needham, *J. Phys. Chem.*, 91, 4219-4228, 1987
101. In references [1, 2 and 6] the authors have collected data for the lipid composition of various animal and bacterial cells, including cell membranes and organelles.
102. According to reference [90] each nanosphere is coated with approximately 1000 streptavidin molecules. Because the streptavidin molecule has four identical Avidin Binding Sites (ABS) (see section 2.1.2), the total number of ABS per nanosphere is about 4000. Presumably only a half of these ABS are on the surface of the coated nanosphere, thus available for binding (the other half is located between the surface of the polysterene nanosphere and the adsorbed protein molecules and is not accessible for the biotin molecules from the bulk)
103. This relation is correct if the mother vesicle and the bud have the same compositions. If they are composed of a mixture of lipids (or other amphiphilic molecules), which aggregate in clusters or domains, one has to take into account the line tension of the domain edge [55, 94]. The composition of the giant vesicles, use in this study can be considered as homogeneous, because the molar fraction of the used lipids was DOPC/biotinyl-CAP-PE:10^6-10^7. Moreover in order to check whether both lipids phase separate (form domains) we conducted Differential Scanning Calorimetry (DSC) experiments (data not shown). The obtained data did not indicate phase separation. Thus we assume that the composition of the mother vesicle and the expelled bud is the same.
104. The bending energy for a cylindrical deformation of a flat laterally isotropic bilayer can be written as [7] $E_B = \frac{1}{2}\kappa c^2$, c=1/R are the curvature and the radius of the deformed membrane cylinder. The flat membrane is set to its equilibrium configuration by setting the spontaneous curvature to zero. Let us consider the relative stretching and compression of the two monolayers with respect to the neutral surface of the membrane [3, 7]. For symmetric stretching moduli, $K_m = K/2$ of the monolayers, the neutral surface of the membrane corresponds to the bilayer midplane. We measure the area of a

monolayer at its corresponding midplane, located at a distance $l_{me}/4$ from the bilayer center. The relative area change of a monolayer is then given by $\Delta A^m / A = \pm l_{me}/4R$. The total bending energy of the bilayer E_B is obtained by summing up the stretching/compression contributions as follows:

$$E_B = 2E^m = \frac{1}{2}(2K_m)\left(\frac{\Delta A^m}{A}\right)^2 = \frac{1}{32R^2} K l_{me}^2 \propto K l_{me}^2$$

105. G. Gommper, H. Endo, M. Mihailescu, J. Allgaier, M. Monkenbuch, D. Richter, B. Jakobs, T. Sottmann, R. Strey, ***:*** *Europhysics Letters, **56(5**), 683-689, 2001*
106. R. Lipowsky, *Journal of Biological Physics*, **28**, 195-210, 2002
107. The reported in reference [44] and [88] equilibrium constant *K*, covers a wide range from 10^1 mM to 10^{12} mM (see Table V, page 105-107 in reference [44]) . The wide range reflects the large number of biotin derivatives and the various experimental conditions at which these constants have been measured, e.g. pH ranging between 2 and 11.8, various buffers and salt concentrations etc. In reference [44] there is no data about the equilibrium constant of d-biotin (used in this study); in reference [88] there is no information about the investigated biotin derivative.
108. M.-N. Designess, B. Maier, Y. Zhang, M. Peliti, D. Bensimon and V. Croquette, *Phys. Rev. Lett*., **89(24)**, 2002, 249102